

**A Final Report for the American Metalcasting Consortium (AMC)
Research Program: Casting Solutions for Readiness (CSR)**

**Modeling of Steel Casting Performance:
Dimensions and Distortion**

Authors: Daniel J. Galles, Richard A. Hardin and Christoph Beckermann

Contacts: Christoph Beckermann (Principal Investigator)
e-mail: christoph-beckermann@uiowa.edu

Richard A. Hardin (Research Engineer)
e-mail: richard-hardin@uiowa.edu

The University of Iowa
Department of Mechanical and Industrial Engineering
3131 Seamans Center
The University of Iowa
Iowa City, Iowa 52242-1527
tel.: (319) 335-6075
fax: (319) 335-5669

Project Partners: Steel Founders' Society of America (SFSA)
SFSA Member Foundries
MAGMA Foundry Technologies
Sivyer Steel
Bradken-London
Bradken-Atlas

Project Period: April 30, 2012 through September 30, 2017

Submitted to:
Advanced Technology International (ATI)
Attn: Mr. Thornton White
315 Sigma Drive
Summerville, SC 29486

September 30, 2017

ABSTRACT

Casting distortions are unacceptable dimensional changes resulting from stresses during solidification and cooling which can result in repair work or scrapped castings. Both the mechanical behaviors and properties of the steel and the sand mold affect the final casting dimensions through mold expansion, and by constraining the casting from free contraction, which introduces stresses and additional distortions. Distortions can lead to a lengthy trial-and-error process of modifying pattern allowances to meet dimensional requirements. In the past, foundries relied on rules-of-thumb, lengthy trial-and-error processes, and excessive machining allowances to meet dimensional tolerances. New dimensional predictive capabilities are especially needed for optimizing the dimensional performance of the thin-walled and light-weight steel castings needed in advanced weapon systems. The research and developments described here were undertaken to address deficiencies of computer models to predict final dimensions and distortions of steel castings. These deficiencies arise from mechanical properties for the mold and the steel not being known with sufficient accuracy, and the software not fully accounting for the mechanical and thermal interactions at the mold-metal interface. Resulting from this project, software tools and material properties necessary to perform such modeling were developed. The steel is modeled as an elasto-visco-plastic material, and the Drucker Prager Cap model is employed for the bonded sand. Properties and models are developed and calibrated with measurements from casting experiments. Steel properties and models are calibrated using steel bar castings that are strained by applying a force to bolts embedded in the bar ends. Restraint forces and the bars' length changes are measured *in situ*. The experiments are simulated by inputting calculated transient temperature fields into a finite element stress analysis that employs the measured forces as boundary conditions. Thermal strain predictions are validated using data from bar experiments without a restraint. The resulting calibrated mechanical property dataset is valid for the high-temperature austenite phase of steel. Bonded sand mold properties and material models are developed using two experimental setups by matching measurements and finite element stress analyses. The two casting experimental geometries used for this are a hollow cylinder and U-shaped bracket. The temporal evolutions of 1) the cylinder's inner diameter and 2) the gap opening between the bracket legs are measured *in situ* utilizing LVDTs (Linear Variable Differential Transformers) connected to quartz rods. By matching the predicted displacements with the measurements, a temperature dependent constitutive dataset is developed. The predictive capabilities of the properties and models are then demonstrated through case studies where dimensional changes and associated distortions for production steel castings are predicted. Pattern allowances for ten casting features are measured and later used to validate the simulations in a case study reported here. Pattern allowances are predicted with good accuracy, as the root mean square (RMS) error between measured and predicted pattern allowances for the new simulation capability is 0.29%, while pattern allowances based on current production practices, known as pattern maker's shrink rule, have a much larger RMS error of 1.31%. Implementation and transitioning of this research for predicting casting dimensions and distortions to industry has been accomplished by undertaking demonstration case studies with industrial partners, implementation of its results in the *MAGMAstress* software available from MAGMA Foundry Technologies, through eleven publications and dozens of presentations to the steel foundry industry.

Table of Contents

<u>Section</u>	<u>Page</u>
1. Introduction and Background	1
2. Experimental and Simulation Procedures	5
2.1 Experimental Procedures for Bar Casting Experiments	5
2.2 Experimental Procedures for Cylinder Casting Experiments	7
2.3 Experimental Procedures for Bracket Casting Experiments	9
2.4 Procedures for Thermal Simulations and Thermophysical Properties	10
2.5 Procedures for Stress Modeling and Properties for Steel and Bar Castings	12
2.6 Stress Modeling Methods, Properties and Procedures for Bonded Sands	20
2.7 Description and Procedures for the Case Study of Dimensional Predictions	28
3. Results and Discussion	33
3.1 Experimental and Simulation Results for Bar Castings	33
3.2 Experimental and Simulation Results for Cylinder Castings	47
3.3 Experimental and Simulation Results for Bracket Castings	65
3.4 Predictions and Measurement Results for Case Study Casting	82
3.5 Implementation and Transitioning of Research to Industry	86
4. Summary of Work and Conclusions	89
Acknowledgements	94
References	94
Appendix A: Student Involvement in Research and Model Development	98

1. Introduction and Background

During sand casting, mechanical interactions between the casting and mold generate distortions, which in turn influence pattern allowances (PA):

$$PA [\%] = \frac{feature\ length_{initial} - feature\ length_{final}}{feature\ length_{initial}} \times 100 \quad [1.1]$$

In Eq. [1.1], *feature length* is the dimension for a particular feature. The *initial* and *final* subscripts refer to the pattern and casting, respectively. In the absence of distortions, pattern allowances are determined solely by thermal strains and commonly referred to as the patternmaker's shrink (e.g., the patternmaker's shrink is approximately 2.1 % for steel), which is commonly used during pattern design as a first estimate to predict casting dimensions. From this viewpoint, distortions can be defined as deviations from the patternmaker's shrink. Examples of these deviations are illustrated in Figure 1.1^[1], where measured pattern allowances from numerous castings are plotted over a range of feature lengths (taken from Voigt^[1]). The considerable scatter of pattern allowances seen in the figure demonstrates that, due to the influence of distortions, the patternmaker's shrink cannot reliably predict pattern allowances.

Distortions can lead to a lengthy trial-and-error process of modifying pattern allowances to meet dimensional requirements. Foundries rely on rules-of-thumb, lengthy trial-and-error processes, and excessive machining allowances to meet dimensional

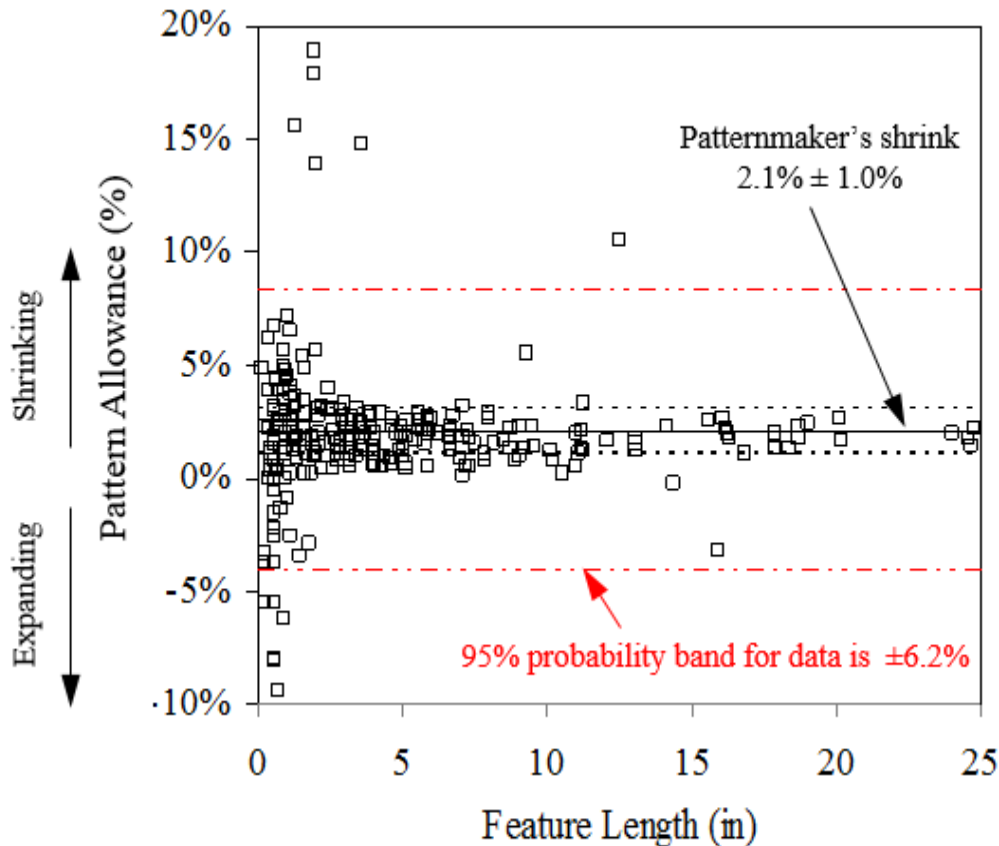


Figure 1.1. Measured pattern allowances plotted as a function of feature length (taken from Voigt [1]). The scatter in the data demonstrates the effect of distortions.

tolerances. New predictive capabilities are especially needed for optimizing the dimensional performance of the thin-walled and light-weight steel castings needed in advanced weapon systems. Hence, the ability to accurately predict stresses and distortions in steel casting processes can lead to more efficient processes and higher quality cast products.

Clearly, casting distortions are unwanted dimensional changes. They result from mechanically and thermally induced stresses during solidification and cooling. Mechanically induced stresses are created when the steel contacts another part of the casting system, while thermally induced stresses are created by uneven cooling. After pouring liquid steel into the casting cavity, the mold temperature increases, and in particular mold cores are subject to rapid and very high temperature increases. Because of these high temperatures, mold cores expand and create mechanical interactions with the steel. The resulting stresses from this and other mold-metal interactions create distortions or plastic strains, particularly where the steel lacks coherency and strength at high temperatures. Both the mechanical behaviors and properties of the steel and the sand mold affect the final casting dimensions through mold expansion. By constraining the casting from free contraction, stresses and additional distortions are induced, which in turn lead to dimensional inaccuracies and defects in the as-cast product. If distortions occur near the end of solidification, hot tears may form, and the casting may be scrapped. The complexities associated with a casting process (i.e., multi-physics constitutive laws, thermo-mechanical coupling, three-dimensional geometries) provide considerable challenges to efficient and accurate stress modeling. In short though, distortions are created by several physical phenomena, including uneven cooling, mold (or core) restraint, and mold (or core) expansion.

Uneven cooling occurs in castings with different section thicknesses. The thinner sections of the casting cool (and thus contract) faster than the thicker sections, generating stresses and associated distortions. A thorough understanding of the casting material behavior throughout the casting process is essential to understand and predict the effects of uneven cooling. In recent years, thermal simulation software has been combined with advanced stress models to predict stresses and deformations during solidification and cooling; to date, the models have been calibrated with stress-strain data from previous mechanical tests (using reheated samples in a controlled environment) [2-6]. Unfortunately, because the microstructure created during solidification differs from that of a reheated specimen, the ability of these models to accurately predict deformations in an industrial casting process has not been verified. In order to emulate the conditions encountered in a casting environment, measurements should be acquired during *in situ* experiments [7-13], from which the measurement of displacements at high temperatures provides a challenge. This *in situ* experimental approach is used in this project to determine the temperature dependent thermo-mechanical properties of steel during solidification and cooling.

Mold restraint constrains thermal contractions in the casting and generates distortions at times ranging from the end of solidification until shakeout. The influence of mold restraint is a well-known problem that has been the focus for previous *in situ* experimental studies [7-11, 13]. The studies usually involved casting a slender bar with a flanges on both ends to induce mold restraint. The experiments were carried out with different metals (steel [7], grey iron [8], ductile iron [9], and aluminum [10,13]) and

bonded sands (sodium silicate [8-10], furan [13], and green sand [8-10]). In addition, Monroe and Beckermann [11] studied the effect of mold restraint on hot tears by casting a T-shaped bar in a no-bake sand mold. Again, in this project an *in situ* experimental approach is used to determine the temperature dependent thermo-mechanical properties for the mold during solidification and cooling.

In contrast to mold restraint, mold expansion occurs at early casting times, shortly after filling. Because the casting is mostly liquid, the sand mold can easily expand into the mold cavity and reduce the casting volume. This expansion is not only due to thermal expansion of the sand, but also dilation, which is the volumetric expansion of a granular material due to a shear force. Dilative behavior is illustrated in Figure 1.2; the initial state of dense sand contains small air voids between the grains (Figure 1.2(a)). After a shear force is applied, however, the irregularly-shaped sand grains translate and/or rotate and cause the voids to grow, resulting in volumetric expansion of the sand aggregate (Figure 1.2(b)). Peters et al. [14] studied mold expansion through *in situ* casting experiments in which a hollow cylinder was produced using silica and zircon sand cores. Distortions were attributed to thermal expansion of the bonded sands as well as core restraint. However, dilation was not considered.

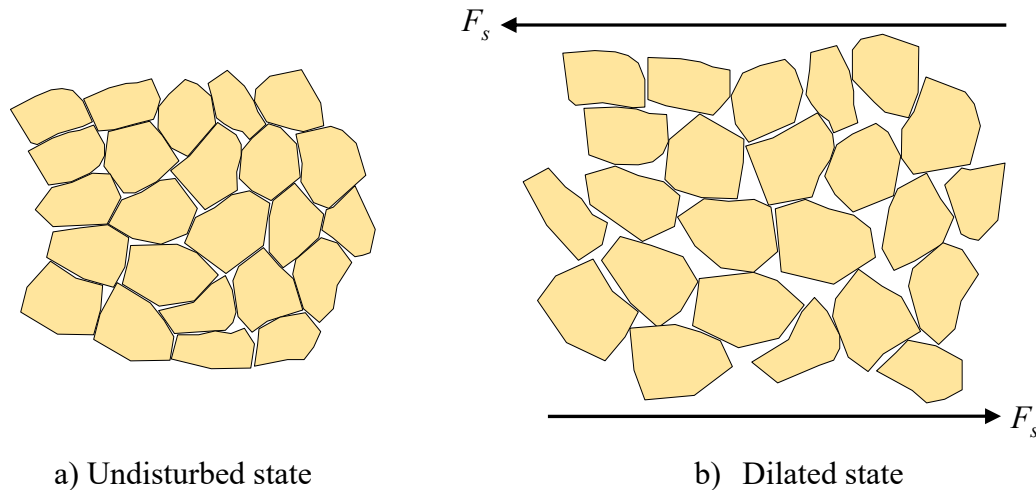


Figure 1.2. Sand dilation. After a shear force, F_s , is applied to the undisturbed state (a), the voids between sand grains increase, resulting in dilation (i.e., volumetric expansion of the sand aggregate), as shown by the dilated state (b).

Computational advances in recent years have stimulated the development of complex constitutive models capable of predicting distortions and pattern allowances for castings of arbitrary size and shape. The accuracy of such models, however, remains uncertain, due in part by the limited availability of realistic mechanical properties and model parameters. This is particularly true at high temperatures where the majority of distortions can be expected to occur. These deficiencies have spurred researchers to study high-temperature properties of bonded sands, including compressive strength [15], tensile strength [16], and elastic modulus [17]. Compressible materials such as sand should be modeled using a constitutive law that considers pressure-dependent yield behavior. This added complexity introduces extra parameters that must be determined through additional

testing. The only high-temperature parameters for such models were determined by Saada et al. [18], who performed triaxial, uniaxial compression, isotropic compression, and die pressing tests on green sand at elevated temperatures to determine parameters for Cam Clay and Hujex constitutive models.

In spite of the contributions from previous studies, the capability of stress analyses to accurately predict distortions and pattern allowances for production castings remains uncertain due in part to the extreme conditions encountered during casting. In particular, the high heating rates near the mold-metal interface cannot be recreated by mechanical tests. Thus, data from these tests may not be appropriate for stress modeling of casting processes. Thole and Beckermann [17] reported significant variations in the elastic modulus for heating rates ranging from 0.8°C/min to 8°C/min. In reality, however, heating rates in the bonded sand within a few millimeters of the mold-metal interface can reach several hundred °C/min. For this reason, the calibration of computational models with data from *in situ* experiments is preferable to calibration from mechanical testing.

Except for relatively simple cases of free shrinkage and trivial mold-metal interactions, current casting simulation models are not capable of predicting the final dimensions and distortion of steel castings accurately. The presence of possible residual stresses and crack formation in castings is also difficult to predict. The primary reason for this is that existing casting simulation software does not fully account for the mechanical and thermal interactions at the mold-metal interface. Also, the mechanical properties of the mold and the steel itself are not known with sufficient accuracy. In order to predict final dimensions and distortions of steel castings accurately using computer modeling, the research undertaken here has resulted in the development and validation of software tools and material properties necessary to perform such modeling.

In this study, *in situ* data on the high temperature deformation behavior for steel is acquired from experimental casting trials using a long, slender low-carbon steel bar. With the aid of a restraint and turnbuckle, an axial force is applied to the bar at high temperatures (before solidification is complete), generating stresses and mechanical strains in the casting. The applied force, dimensional changes, and temperatures of the bar are measured dynamically throughout the casting process. An additional bar casting trial serves as the experimental control to determine the thermal strain in the steel bar, which is subsequently subtracted from the total strain to calculate the mechanical strain. Experiments investigating the mold material properties are performed using a hollow cylinder and U-shaped bracket. All experimental data are used to calibrate finite element stress model parameters by matching the *in situ* and the simulated distortions and pattern allowance predictions. During all experiments, the temporal evolution of selected casting features are measured *in situ* by utilizing LVDTs (Linear Variable Differential Transformers) connected to fused quartz rods. In addition, temperatures are measured in the castings, molds, and cores. For the cylinder experiments, distortions are generated by core expansion during solidification. For the bracket experiments, distortions are generated mainly at later times, as the mold restrains thermal contractions in the bracket. For the simulations, distortions are predicted using a one-way temperature-displacement coupling. Temperatures are calculated first using casting simulation software and then input to a finite element stress analysis. The steel is modeled using an elasto-visco-plastic constitutive law, whose parameters were calibrated using the bar casting data [19]. The bonded sands are modeled using the Drucker-Prager Cap (DPC) constitutive law. Mechanical properties

are taken from the literature or estimated through room temperature mechanical testing. By matching the measured and predicted feature lengths for the bar, cylinder and bracket experiments, a constitutive dataset is developed that can be used to predict pattern allowances for production steel sand castings. This capability is then demonstrated through case studies of dimensional measurements and predictions for production steel castings.

2. Experimental and Simulation Procedures

2.1 Experimental Procedures for Bar Casting Experiments

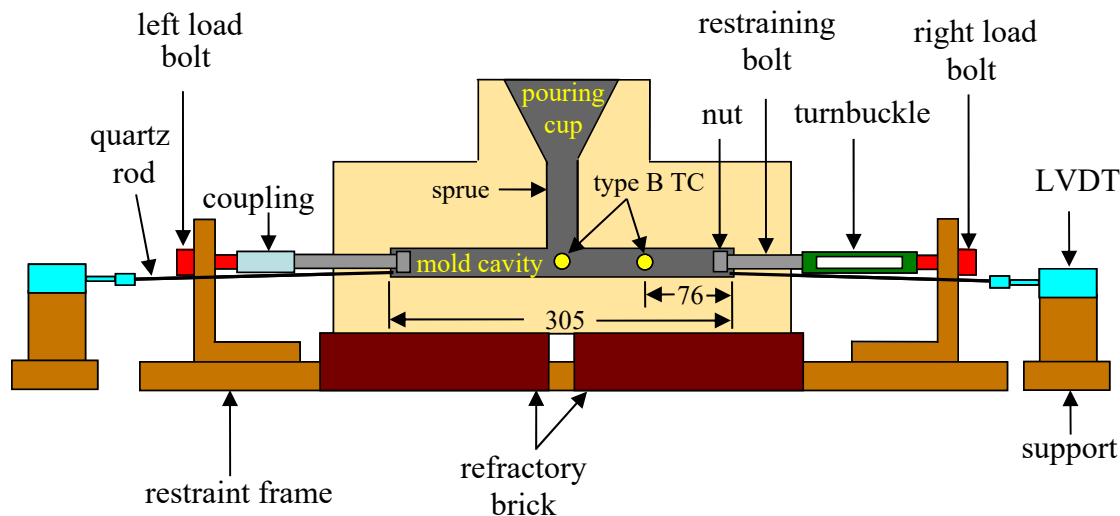
The bar castings experiments were designed to collect data for model development and calibration for the cast steel properties needed to predict dimensions and distortions. The experimental design was motivated from the presumption that the total strain, ϵ_{total} , can be decomposed into the sum of its mechanical, ϵ_{mech} , and thermal, ϵ_{th} , parts, as

$$\epsilon_{total} = \epsilon_{mech} + \epsilon_{th} \quad [2.1]$$

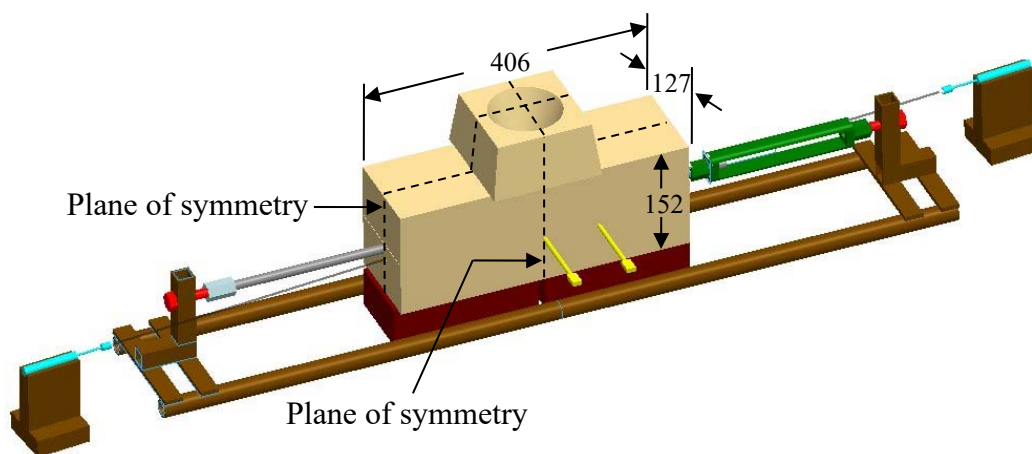
Consequently, two sets of casting trials, referred to as “strained” and “unrestrained”, were designed to measure ϵ_{total} and ϵ_{th} independently. Schematics of the setup for the strained bar experiments are shown in Figure 2.1. A slender steel bar (305 mm long with a 25 mm square cross section) was cast in a sand mold. The mold cavity was filled through the pouring cup and sprue (which also serves to feed the casting) located at the center of the bar. With the aid of a restraint frame and steel bolts inserted at the two ends of the bar, the thermal shrinkage along the axis of the bar was constrained during solidification and cooling to induce stresses. Preliminary experiments showed that this effect alone did not generate sufficient viscoplastic strains. Therefore, a turnbuckle was added in line with one of the restraining bolts to produce additional distortions. In order to prevent slippage between the casting and the bolts, nuts were inserted over the ends of the bolts in the mold cavity. Removal of the restraint, restraining bolts, load bolts, coupling, turnbuckle, and nuts reduces the schematic in Figure 2.1 to the setup for the unrestrained bar experiments.

Contact interactions at the mold-metal interface were minimized due to the simple geometry and the symmetry of the setup about the two vertical planes shown in Figure 2.1(b). Friction forces between the casting and mold generated negligible mechanical strains due to the small casting weight. For these reasons, dimensional changes in the unrestrained bars were due to thermal strains only, whereas all measured distortions in the strained bars were a consequence of the restraint.

In order to collect data, several devices were used; a load bolt was connected in-line with each restraining bolt (via a coupling on the left side and turnbuckle on the right side of Figure 2.1(a)) to continuously measure the axial restraint force at both ends of the bar. The axial displacements at each end of the bar were transmitted via quartz rods to LVDTs, from which the axial length change was calculated by adding the LVDT measurements together. Finally, type B thermocouples were encased in quartz tubes and inserted into the mold cavity to measure steel temperatures directly under the sprue and 76 mm from the end of the casting.



(a) Mid-section cut



(b) CAD Drawing









Figure 2.1. Schematics of the setup for the strained bar experiments. All dimensions are in mm. Forces, displacements, and temperatures were measured in-situ with load bolts, LVDTs, and type B thermocouples, respectively.

To build the molds, silica lake sand was bonded using a phenolic urethane no-bake (PUNB) binder system (which accounted for 1.25% of the total mold weight) and mixed with a 55:45 ratio of Part 1 (PEP SET[®] 1000) to Part 2 (PEP SET[®] 2000). The chemical reaction was accelerated with a catalyst (PEP SET[®] 3501) based on 6% of the binder weight.

Bar casting experiments were performed at the University of Northern Iowa's Metal Casting Center. The target chemistry was ASTM A216 grade WCB carbon steel, which was prepared in an induction furnace and poured from a 250 lb heat at approximately 1873 K (1600 °C). The measured compositions of the cast steel for each experiment are provided in Table 2.1. Following pouring, the strained bars were allowed to partially solidify, after

which the turnbuckle was engaged (i.e., turned) to lengthen the bar and induce distortions. Due to differences in casting chemistry, the solidification times varied among the casting heats. A value of 1673 K (1400 °C) (the approximate temperature at the end of solidification) was typically assumed as the temperature at which the casting could transmit stresses. Once the thermocouple reading (under the sprue) had fallen below this temperature, the turnbuckle was slowly engaged for a period of 30-60 s.

Table 2.1 Summary of the color codes (used in the plots) and casting chemistries for all unrestrained (unr.) and strained (str.) bars.

Set	Color Code	Casting Chemistry								
		%C	%Si	%Mn	%P	%S	%Cr	%Al	%Cu	%Fe
unr. 1		0.21	0.50	0.52	0.072	0.002	0.08	0.070	0.08	bal.
unr. 2		0.32	0.69	0.64	0.025	0.014	0.23	0.054	0.10	bal.
unr. 3		0.25	0.59	0.55	0.012	0.014	0.04	0.069	0.04	bal.
str. 1		0.25	0.58	0.62	0.022	0.016	0.03	0.087	0.05	bal.
str. 2		0.42	0.78	0.65	0.068	0.010	0.09	0.057	0.08	bal.
str. 3		0.25	0.61	0.56	0.021	0.017	0.10	0.071	0.08	bal.
str. 4		0.25	0.45	0.46	0.019	0.017	0.04	0.045	0.03	bal.
str. 5		0.30	0.57	0.41	0.031	0.026	0.02	0.056	0.01	bal.

2.2 Experimental Procedures for Cylinder Casting Experiments

In the cylinder experiments, the casting geometry consisted of a thick-walled cylinder with dimensions (in mm) shown in Figure 2.2(a). A schematic of the experimental design is depicted at the casting mid-plane in Figure 2.2(b). The hollow section of the cylinder was created with a core, which was held in place with a core print. The temporal evolution of the inner diameter at the mid-height of the cylinder was measured by utilizing two identical assemblies consisting of a quartz rod, quartz tube, and LVDT. One end of the quartz rod was flattened into a disc (approximately 7 mm in diameter) using an oxy-acetylene torch and inserted through pre-drilled holes in the drag and core. The disc was butted to the outer diameter of the core, as shown in Figure 2.2(b). In order to transmit displacement, the quartz rod passed through a quartz tube, which traversed the mold cavity. The other end of the quartz rod was attached to an LVDT, which continuously measured the displacement from one side of the inner diameter. The other assembly measured displacement on the opposite side of the cylinder. The LVDT measurements were added together to calculate the temporal evolution of the inner diameter. It should be noted from Figure 2.2(b) that both LVDT measurements could not be taken at the same height. Therefore, one measurement was taken approximately 5 mm above the cylinder mid-height, while the other was taken 5 mm below the mid-height.

Temperatures were measured at several locations. Type K thermocouples were inserted through the bottom of the drag and into the core at radial distances of 6, 9, 15, and 25 mm from the vertical core-casting interface. The thermocouples were staggered circumferentially to minimize the influence from other thermocouples. A type B

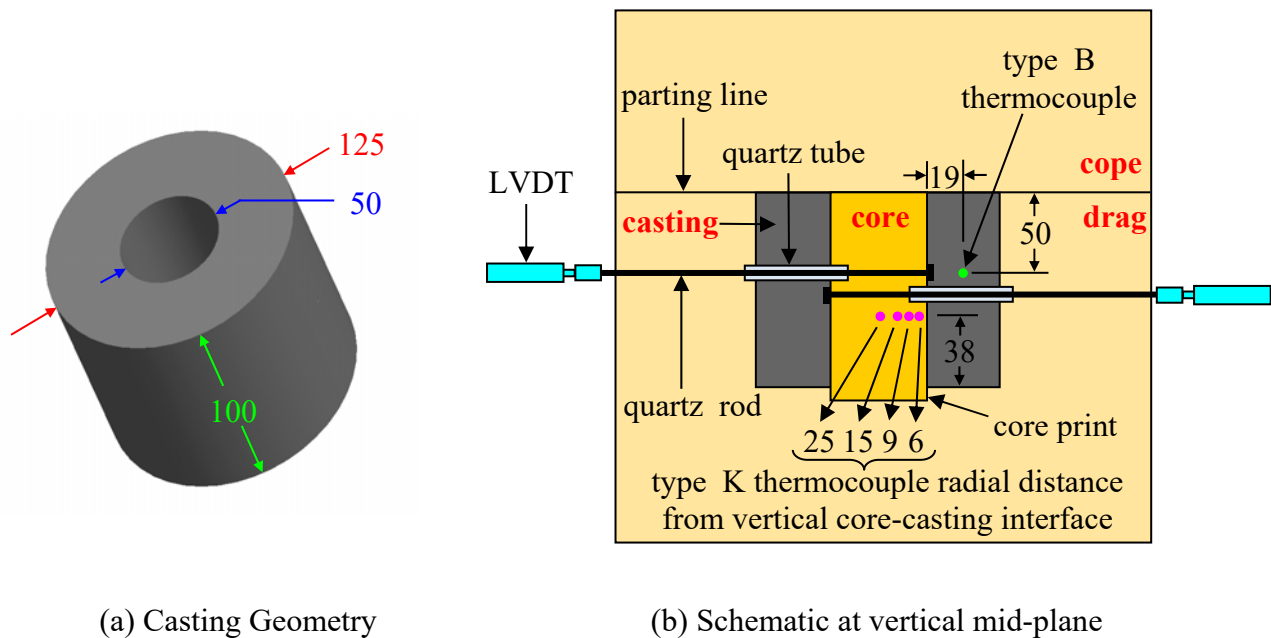


Figure 2.2 Casting geometry (a) and experimental schematic (b) for the cylinder experiments. All dimensions in mm.

thermocouple was encased in a quartz tube and inserted into the mold cavity to measure the temperature of the steel.

To build the cope and drag, Unimin® IC55 silica lake sand was bonded with a phenolic urethane no-bake (PUNB) binder system. The binder (1.25% of mold weight) was mixed using a 55:45 ratio of part 1 (PEPSET® 1000) to part 2 (Techniset® 6435). The cores were produced from either Unimin® IC55 silica lake or zircon sand and bonded using the same binder system as the cope and drag. The cope and drag were hand packed, whereas the cores were manually rammed. The core weights varied less than 1% for each type of core sand.

In total, 5 cylinders of each core type were produced (10 cylinders in total). For the first 4 cylinders, the inner diameter evolution was measured, as well as temperatures in the steel and at the 25 mm location in the core. For the final cylinder of each core type, no displacement or temperatures in the steel were recorded; only temperatures at the 4 core locations (shown in Figure 2.2(b)) were measured.

Experimental casting trials were performed at the University of Northern Iowa's Metal Casting Center. The target chemistry was ASTM A216 grade WCB carbon steel. The castings were poured from a 250 lb heat and prepared in an induction furnace. Because of the heat loss encountered during the transfer from the furnace to pouring ladle, the molten steel was heated to approximately 1700°C in the furnace. The castings were poured within four hours after building the molds. Immediately before pouring, any slag was removed from the ladle. The liquid steel was poured directly into the mold cavity, after which the cope was placed on top of the drag. This method was utilized to avoid additional mold-metal interactions from the sprue. For this reason, the mold cavity was never completely filled and an air gap (approximately 5 mm) existed between the casting and cope.

2.3 Experimental Procedures for Bracket Casting Experiments

The geometry and experimental setup for the U-shaped bracket is shown in 2.3(a) and 2.3(b), respectively. The outer mold dimensions are 254 mm (length) \times 254 mm (width) \times 75 mm (height) for the cope and 254 \times 254 \times 230 for the drag. In total, 4 brackets were cast. A simple gating system consisting of a sprue (25 mm radius \times 50 mm height) and pouring cup (which also served as a feeder) was utilized.

Displacement was measured by utilizing same LVDT-quartz rod assemblies used in the cylinder experiments. The ends of the quartz rods were bulged into spherical shapes (to firmly anchor the rods into the steel and eliminate any slippage) using an oxy-acetylene torch and inserted through pre-drilled holes in the drag (at the casting mid-plane) and extended approximately 3 mm into and 5 mm above the bottom of the mold cavity. As in the cylinder experiments, the LVDT measurements were then added to calculate the temporal evolution of the distance between the bulged ends of the quartz rods, henceforth known as the “outer length” (see 2.3(b)).

Temperatures were measured at the vertical casting mid-plane. Type K thermocouples were inserted midway between the bracket legs at 25, 50, 75, and 100 mm from the bottom horizontal casting surface, as shown in 2.3(b). Additionally, a type B thermocouple was encased in a quartz tube and inserted underneath the sprue, albeit slightly offset to prevent inertial forces from molten stream to potentially break the quartz tube during filling.

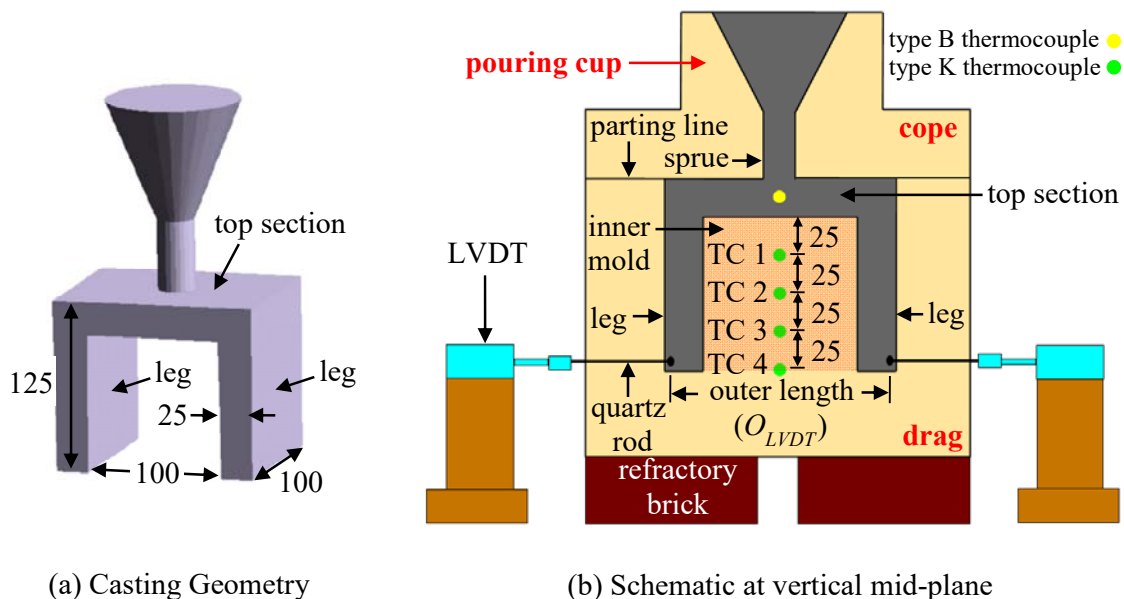


Figure 2.3 Casting geometry (a) and experimental schematic (b) for the bracket experiments. The bracket consisted of a top section and two legs. The region between the bracket legs (light red) is termed the “inner mold”. The temporal evolution of the outer

The molds were built using the same materials that were used for the cylinder experiments (Unimin® IC55 silica lake sand bonded with a PUNB binder system). The drag was constructed as a single piece and hand packed; hence, no core was used. The molds were poured under the same conditions as those described in the previous section for

the cylinders, except that a pouring cup was used. Therefore, for the bracket experiments, the castings were poured directly from the pouring ladle into the pouring cup.

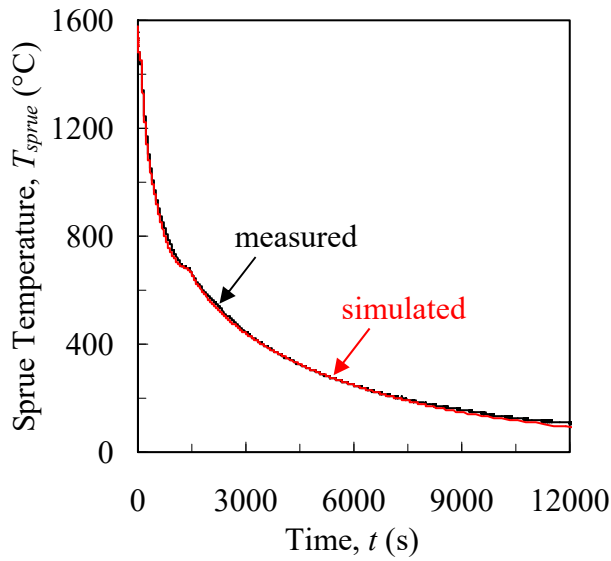
2.4 Procedures for Thermal Simulations and Thermophysical Properties

Temperatures throughout the project work were predicted using the commercial casting simulation software MAGMASOFT^[20], which required several inputs. Mold properties were taken directly from the MAGMASOFT[®] database. Temperature-dependent thermophysical properties (i.e., density, specific heat, thermal conductivity) of the steel, as well as the solid volume fraction as a function of temperature and the latent heat of solidification, were calculated with IDS^[21] software using the measured steel chemistries for each experiment (Table 2.1). The interfacial heat transfer coefficient (at the mold-metal interface) was initially specified as a constant value.

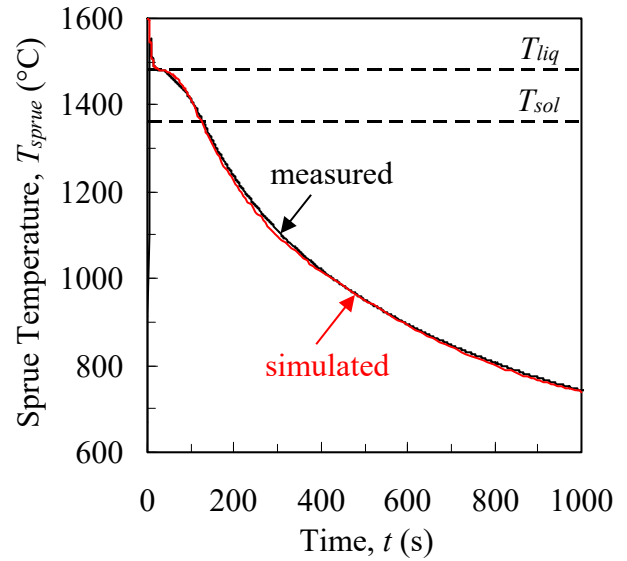
In general, using the initial property datasets and boundary conditions did not result in good agreement between measured and predicted temperatures. Therefore, through a trial-and-error process, several adjustments to the simulation inputs were made. The process is described in detail elsewhere^[22,23]. The main modifications involved the temperature dependent interfacial heat transfer coefficient and solid fraction. In particular, the solid fraction curve was adjusted to exactly match the measured liquidus and solidus temperatures and measured cooling rates during the solidification interval. An example of an adjusted solid fraction curve is provided in Figure 2.4(d). The slight kink in the solid fraction curve at about $g_s = 0.3$ is due to the transformation of δ -ferrite to austenite. As is typical for cast steels, the total solidification interval exceeds 120 K, but more than 90% of the liquid solidifies within the first 50 K. It is important to note that a different solid fraction curve resulted from the thermal simulation for each of the eight experiments. These variations can be attributed to the different steel compositions (see Table 2.1). After the adjustments, excellent agreement was achieved between measured and predicted temperatures for each experiment. An example of this agreement (from the strained bar 5 simulation) is shown in Figures 2.4(a) (overall time scale) and 2.4(b) (intermediate time scale).

An example of predicted temperature fields (from the strained bar 1 simulation) at the beginning and end of the straining period is shown in Figures 2.5(a) and 2.5(b). At any location in the bar, large temperature drops ($\Delta T > 175$ K) can be observed between the beginning and end of the straining period. In addition, significant temperature variations can be seen both over the length of the bar and over each of the cross sections, labeled A-D. Section A is located directly under the sprue and contains the highest temperatures in the bar at any particular time, whereas section D is near the end of the bar and contains lower temperatures.

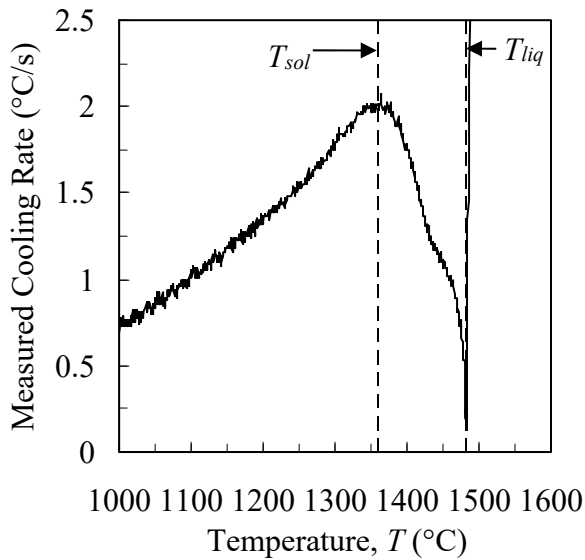
For the stress model used in this project, the strains are dependent on the solid fraction, g_s (see the following section). Due to the hot spot created by the sprue at the bar's mid-length, cross section A (see Figure 2.5) is the last to solidify. The predicted solid fractions for cross section A at the onset of straining are shown for all strained bars in Figure 2.5(c). The values vary from $g_s \approx 0.6$ at the middle of strained bar 1 to $g_s = 1$ at all locations in strained bar 4. In most of the experiments, however, the bar was close to or fully solidified when straining commenced. Hence, the effect of the solid fraction in the



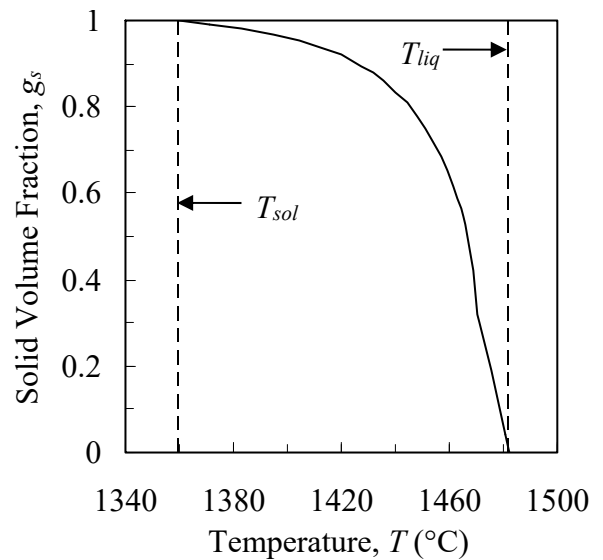
(a) Complete Time Scale



(b) Intermediate Time Scale



(c) Measured Cooling Rate



(d) Solid Volume Fraction

Figure 2.4 Comparison (from strained bar 5) between measured and predicted sprue temperatures on complete (a) and intermediate (b) time scales. The solidus and liquidus temperatures are determined from the measured cooling curve in (c). The adjusted solid volume fraction curve used for the simulations is shown in (d).

stress model can be expected to be small. Nonetheless, the variations from bar to bar emphasize again that the five strained bar experiments provide mechanical data for different temperature ranges and are not intended to duplicate each other. The predicted temperature fields in the steel for each experiment were saved at a large number of time

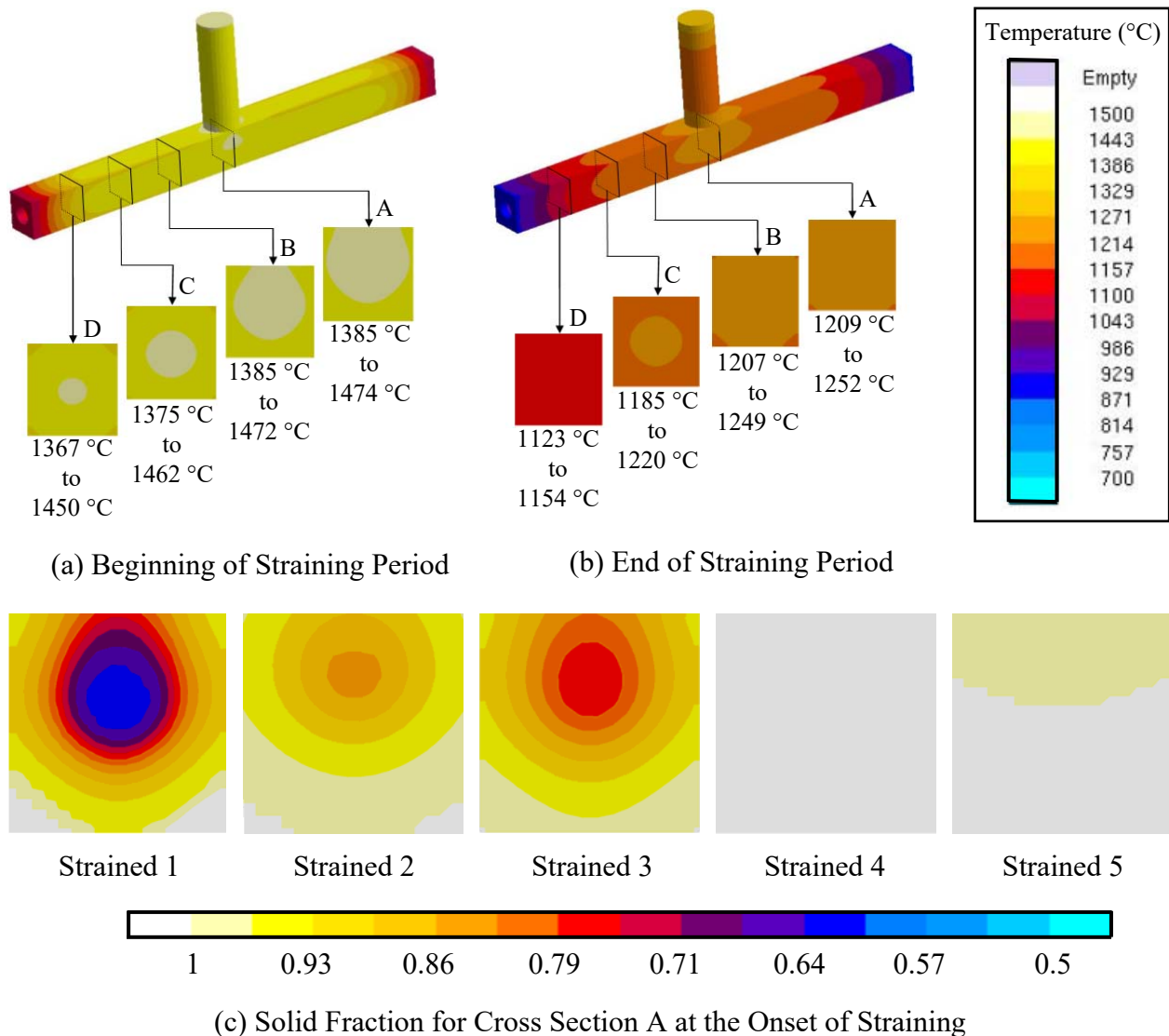


Figure 2.5 Predicted temperature fields for strained bar 1 at the beginning (a) and end (b) of the straining period. The predicted solid fraction contours for cross section A (location shown in (a) and (b)) at the onset of straining.

steps (approximately 100) and subsequently mapped onto the finite element mesh used in the stress analysis (see below).

2.5 Procedures for Stress Modeling and Properties for Steel and Bar Castings

During the project, an elasto-visco-plastic constitutive model that considers damage was implemented in an ABAQUS user-defined UMAT subroutine to predict stresses and distortions during solidification and cooling in a steel casting. To validate the model, experimental data was acquired from *in situ* casting trials in which a long, slender low-carbon steel bar is produced. With the aid of a restraint and turnbuckle, an axial force was applied to the bar at high temperatures (before solidification is complete), generating stresses and mechanical strains in the casting. The applied force, dimensional changes, and

temperatures of the bar were measured dynamically throughout the casting process. An additional casting trial served as the experimental control to determine the thermal strain in the steel bar, which was subsequently subtracted from the total strain to calculate the mechanical strain.

Through a decoupling of the volume-averaged conservation equations, stresses and deformations are predicted in a two-step process using commercial software. In the first step, *MAGMASoft* calculates the temperature fields during solidification and cooling, which are then used to determine the preliminary temperature-dependent mechanical properties (estimated with experimental stress-strain data from the literature) at all times and locations throughout the bar. In the second step, stresses and deformations are calculated with ABAQUS; the experimental control is simulated first to determine the thermal expansion coefficient of the steel. Then, using the measured force as a boundary condition, the axial length change of the steel bar is predicted. Finally, through an adjustment to the elasto-visco-plastic parameters, the measured and simulated distortions are matched at all times throughout the casting process.

The stress simulations were performed using the general-purpose finite element software ABAQUS®. The present constitutive model was implemented in a user-defined UMAT subroutine^[24]. To save computational costs, the simulation model was somewhat simplified. Frictional forces at the mold-metal interface were estimated to be negligibly small, and the mold was not included in the simulations. Additionally, the metal in the pouring cup did not contribute to distortions in the bars and was also excluded. Finally, the parts of the restraining bolts protruding from the casting (which only served to transmit forces) were omitted. The resulting ABAQUS® model for the strained bar is shown in Figure 2.6. Approximately 60,000 second-order tetrahedral elements (90,000 nodes) were used to generate the mesh.

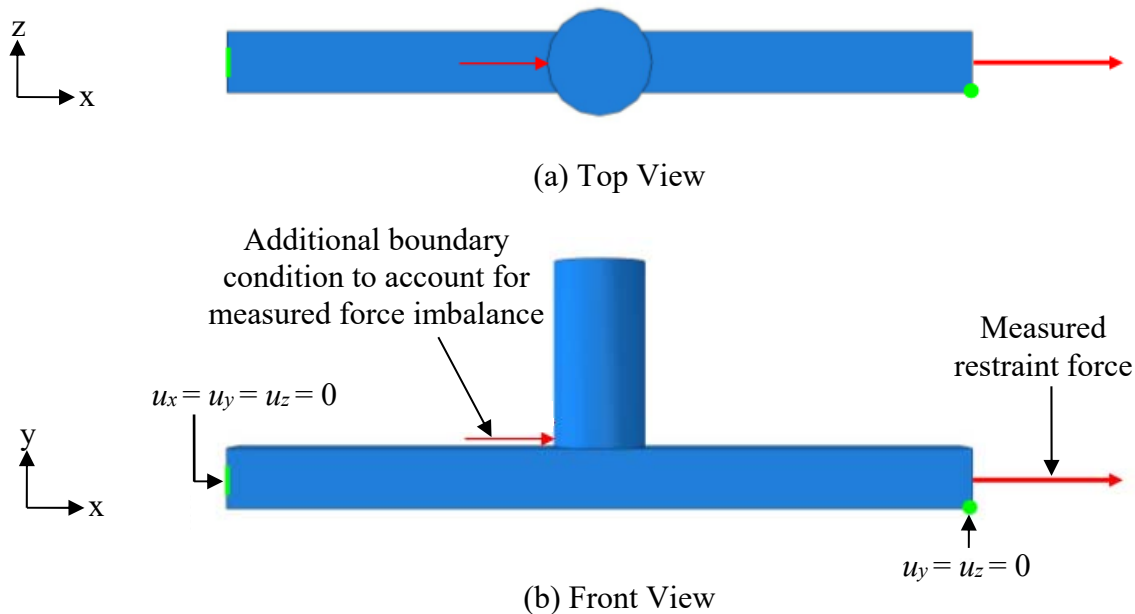


Figure 2.6 Top (a) and front (b) views of the ABAQUS® model for the strained bar. An additional force boundary condition was applied at the base of the sprue to account for the measured force imbalance (shown in results section).

For the strained bars, a zero displacement ($u_x = u_y = u_z = 0$) boundary condition was specified at one end of the bar. Although both ends translated during cooling, the axial length change is a relative displacement (between the bar ends); therefore, constraining one end was sufficient for the simulations. At the other end, the measured restraint force was assigned. In order to account for the force imbalance (shown in the results section), the difference between the forces measured at the two ends was applied at the base of the sprue. Because the mold was excluded, an additional displacement boundary condition was required (shown on the right end of the model in Figure 2.6) to constrain the length change for the bar to the axial direction (i.e., $u_y = u_z = 0$). Omission of the force boundary conditions in Figure 2.6 reduces the model for the strained bars to the unrestrained case.

Stress Model for the Steel

The stress model developed is based on the work of Monroe and co-workers^[26]. In this model, the effective stress depends on the solid fraction. This dependency eliminates the need to model each region in a casting (i.e., fully liquid, semi-solid, fully solid) as a separate material and therefore leads to a robust model capable of predicting the strains and stresses over the entire temperature range using a single constitutive relation. For $g_s = 1$ (fully solid), the model reduces to a standard elasto-visco-plastic model.

Assuming negligible inertial effects, body forces, and momentum transport between the solid and liquid during solidification, the solid momentum equation is given by

$$\nabla \cdot \boldsymbol{\sigma} = 0 \quad [2.2]$$

where $\boldsymbol{\sigma}$ is the effective stress tensor. The semi-solid mush created during solidification is treated as a compressible porous medium where the stress depends on the pressure. In such media, the stress tensor is given by^[27]

$$\boldsymbol{\sigma} = g_s \boldsymbol{\sigma}_s + g_l p_l \mathbf{I} \quad [2.3]$$

where g_s is the solid volume fraction, $\boldsymbol{\sigma}_s$ is the Cauchy stress tensor of the solid material, and \mathbf{I} is the second-order identity tensor. Near the end of solidification, the liquid pressure minimally contributes to casting stresses and is set to $p_l = 0$.

Using small strain theory, the strain tensor, $\boldsymbol{\varepsilon}$, is decomposed into the elastic ($\boldsymbol{\varepsilon}_e$), thermal ($\boldsymbol{\varepsilon}_{th}$), and viscoplastic ($\boldsymbol{\varepsilon}_{vp}$) components as

$$\boldsymbol{\varepsilon} = \boldsymbol{\varepsilon}_e + \boldsymbol{\varepsilon}_{th} + \boldsymbol{\varepsilon}_{vp} \quad [2.4]$$

The elastic strain is determined from Hooke's law as

$$\boldsymbol{\sigma} = \mathbf{C}_e : \boldsymbol{\varepsilon}_e \quad [2.5]$$

where \mathbf{C}_e is the elastic stiffness tensor. Assuming a homogeneous and isotropic material, it is given by

$$\mathbf{C}_e = \frac{E}{3(1-2\nu)} \mathbf{I} \otimes \frac{E}{3(1+\nu)} \mathbf{I}_{dev} \quad [2.6]$$

where E is the effective Young's modulus, ν is the effective Poisson's ratio, \mathbf{I} is the fourth-order identity tensor, and \mathbf{I}_{dev} is the fourth-order deviatoric identity tensor. The effective elastic properties are determined using the following solid fraction dependent relations^[29]

$$E = E_s \left(\frac{g_s - g_s^{coh}}{1 - g_s^{coh}} \right)^{n^E} \quad [2.7]$$

and

$$\nu = \nu_0 + \left(\frac{g_s - g_s^{coh}}{1 - g_s^{coh}} \right) (\nu_s - \nu_0) \quad [2.8]$$

In Eq. [2.7], the effective Young's modulus is scaled between Young's modulus of the solid material, E_s , at $g_s=1$ and a negligibly small value at the coherency solid fraction, g_s^{coh} . The coherency solid fraction refers to the moment during solidification when the solid dendrites become sufficiently entangled to form a continuous network that allows stresses to be transmitted. The coherency solid fraction was taken as $g_s^{coh}=0.5$ and the power coefficient, n^E , as 2.5^[29]. Eq. [2.8] shows that the effective Poisson's ratio is linearly scaled from the fully solid value at $g_s=1$ to a minimum Poisson's ratio, $\nu_0=0.14$ ^[28] at g_s^{coh} .

The thermal strain is given by

$$\boldsymbol{\varepsilon}_{th} = \alpha_{tot} (T - T_{th}) \mathbf{I} \quad [2.9]$$

where T_{th} is the temperature at the onset of thermal contraction. Additionally, α_{tot} is the total linear thermal expansion coefficient and defined as

$$\alpha_{tot} = \frac{1}{(T - T_{th})} \int_{T_{th}}^T -\frac{1}{3\rho_s} \frac{d\rho_s}{dT} dT \quad [2.10]$$

where ρ_s is the solid density. Eq. [2.10] is the form of the linear thermal expansion coefficient required by ABAQUS[®]^[30].

The viscoplastic strain rate is given by an associated flow law [31],

$$\dot{\boldsymbol{\varepsilon}}_{vp} = \dot{\gamma} \frac{\partial \sigma_{eq}}{\partial \boldsymbol{\sigma}_0} \quad [2.11]$$

where \mathcal{P} is the scalar flow parameter and σ_{eq} is the equivalent stress. The latter is taken as^[32]

$$\sigma_{eq}^2 = A_1 q_s^2 + A_2 p_s^2 \quad [2.12]$$

In Eq. [2.12], the pressure of the solid, $p_s = -1/3(\mathcal{P} \mathbf{I})$, is the mean of the normal stresses from the effective stress tensor. The von Mises stress of the solid, $q_s = \sqrt{3/2(\boldsymbol{\tau}_s : \boldsymbol{\tau}_s)}$, is determined from the deviatoric stress tensor, $\boldsymbol{\tau}_s = \mathcal{P} \mathbf{I} + p_s \mathbf{I}$. The equivalent stress can be thought of as the scalar form of the effective stress tensor. The functions A_1 and A_2 are from Cocks model^[33] and defined as

$$A_1 = \left(1 + \frac{2}{3}(1 - g_s^*)\right) (g_s^*)^{-2/(1+m)} \quad [2.13]$$

and

$$A_2 = \frac{9}{4} \left(\frac{1 - g_s^*}{2 - g_s^*} \right) \left(\frac{2}{1 + m} \right) (g_s^*)^{-2/(1+m)} \quad [2.14]$$

where m is the strain rate sensitivity exponent and g_s^* is the scaled solid fraction. In the limit where the solid fraction is unity, the equivalent stress reduces to the von Mises stress, where A_1 is equal to unity and A_2 is equal to zero. The scaled solid fraction is defined as

$$g_s^* = \left(\frac{g_s - g_s^{coh}}{g_s^{coal} - g_s^{coh}} \right) \quad [2.15]$$

where g_s^{coal} is the coalescence solid fraction, which occurs near the end of solidification and represents the upper limit of the scaled solid fraction, above which scaling is not employed. The coalescence solid fraction was set to 0.85, the value from a previous study^[4] below which ductile fracture occurred in a round tensile bar due to coalescence of voids. For the present study, the bar was near complete solidification when straining began (see Figure 2.5(c)), with only the interior region under the sprue containing semi-solid material in some experiments. Therefore, the coherency and coalescence solid fractions had a negligibly small effect on the present results.

The dynamic yield stress, σ_{dy} , defines the stress-strain relationship after yielding occurs. The relation used here is taken from Marin and McDowell^[35] and given by

$$\sigma_{dy} = \sigma_0 \left(1 + \frac{\varepsilon_{eq}}{\varepsilon_0} \right)^n \left(1 + \frac{\mathcal{P}_{eq}}{\mathcal{P}_0} \right)^m \quad [2.16]$$

where σ_0 is the initial yield stress, n is the strain hardening exponent, and m is the strain rate sensitivity exponent. The equivalent plastic strain rate, $\dot{\epsilon}_{eq}$, is determined from the scalar dissipation of energy according to

$$\dot{\epsilon}_{eq} = \frac{\sigma_0 \dot{\epsilon}_{yp}}{g_s \sigma_{dy}} \quad [2.17]$$

The equivalent plastic strain, ϵ_{eq} , is obtained by integrating the equivalent plastic strain rate over time for temperatures below the annealing temperature. The annealing temperature is taken as T_{sol} . Additionally, ϵ_0 is the reference strain, defined as $\epsilon_0 = \sigma_0 n / E$, and $\dot{\epsilon}_0$ is the reference strain rate. The latter is given by the Arrhenius equation $\dot{\epsilon}_0 = A \exp(-Q/RT)$, where A is the Arrhenius prefactor, Q is the activation energy, R is the universal gas constant, and T is the absolute temperature. When the equivalent stress exceeds the dynamic yield stress, the equivalent plastic strain is increased to satisfy $\sigma_{eq} = \sigma_{dy}$. Combining this relation with Eq. [2.12] defines the yield surface as

$$f = \sigma_{dy}^2 - A_1 q^2 - A_2 p_s^2 = 0 \quad [2.18]$$

Mechanical Properties for Steel

The elastic properties were obtained from the literature. The temperature-dependent Young's modulus was taken from Koric and Thomas^[36]. Also, because experimental observations of increased Poisson's ratio with temperature may be due to increasing amounts of creep during the test^[37], a constant value of 0.3 was used.

Substituting the reference strain and reference strain rate definitions into the dynamic yield stress equation (Eq. [2.16]) gives

$$\sigma_{dy} = \sigma_0 \left(1 + \frac{E \epsilon_{eq}}{\sigma_0 n} \right)^n \left(1 + \frac{\dot{\epsilon}_{eq}}{A \exp(-Q/RT)} \right)^m \quad [2.19]$$

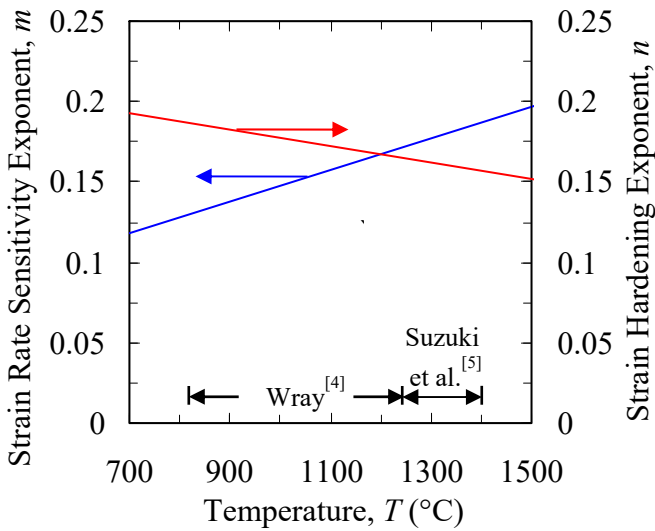
Now it can be seen that 5 material parameters must be known: σ_0 , n , m , A , and Q . These parameters were estimated for austenite using data from the uniaxial tensile tests of Wray^[4] ($1123 \text{ K (} 850 \text{ }^\circ\text{C)} \leq T \leq 1523 \text{ K (} 1250 \text{ }^\circ\text{C)}$) and Suzuki et al.^[5] ($1523 \text{ K (} 1250 \text{ }^\circ\text{C)} \leq T \leq 1673 \text{ K (} 1400 \text{ }^\circ\text{C)}$) involving reheated steel specimens. The Levenberg-Marquardt algorithm, which minimizes the difference between measured and predicted values of a nonlinear function with a least squares method, was employed to perform the fit. Following the method of Kozlowski et al.^[38], the initial yield stress (σ_0), strain hardening exponent (n), and strain rate sensitivity exponent (m) were initially estimated as quadratic functions of temperature but later reduced to linear, as differences between the fits were found to be small. The activation energy (Q) was estimated as a constant value. To account for carbon-content dependency, the Arrhenius prefactor (A) was estimated as a

quadratic function of the carbon content^[38]. The estimated parameters are provided in Table 2.2.

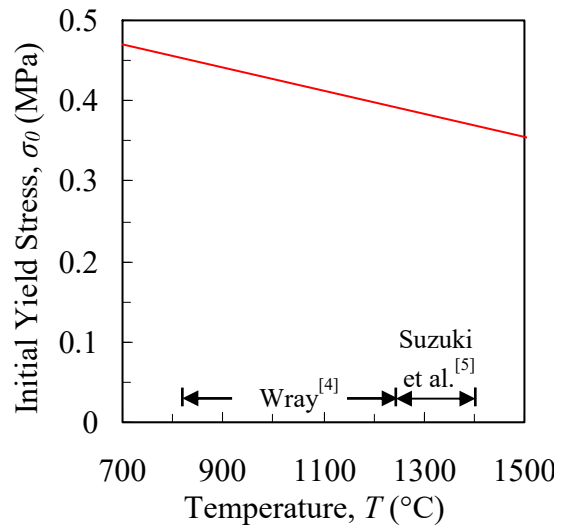
Table 2.2 Estimated parameters from the mechanical tests of Wray^[4] and Suzuki et al.^[5]

Parameter	Expression	Units
Initial Yield Stress, σ_0	$5.729 \times 10^{-1} - 1.461 \times 10^{-4} T$	MPa
Strain Hardening Exponent, n	$2.457 \times 10^{-1} - 6.192 \times 10^{-5} T$	-
Strain Rate Sensitivity Exponent, m	$4.924 \times 10^{-2} + 9.930 \times 10^{-5} T$	-
Arrhenius Prefactor, A	$2.501 \times 10^4 + 1.246 \times 10^5 (\%C)^+ + 1.240 \times 10^4 (\%C)^2$	1/s
Activation Energy, Q	354	kJ/mol

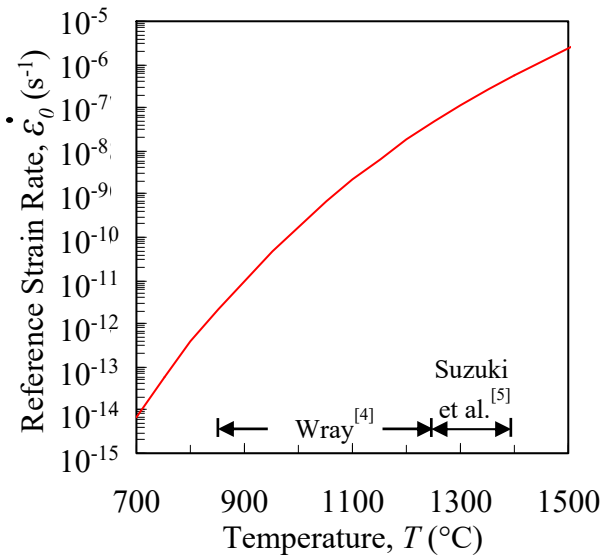
The estimated viscoplastic material parameters are plotted over the approximate temperature range of austenite ($973 \text{ K (} 700 \text{ }^\circ\text{C)} \leq T \leq 1773 \text{ K (} 1500 \text{ }^\circ\text{C)}$) in Figure 2.7. Note, however, that the tensile test data are limited to a temperature range of $1123 \text{ K (} 850 \text{ }^\circ\text{C)}$ to $1523 \text{ K (} 1250 \text{ }^\circ\text{C)}$ for Wray^[4] and $1523 \text{ K (} 1250 \text{ }^\circ\text{C)}$ to $1673 \text{ K (} 1400 \text{ }^\circ\text{C)}$ from Suzuki et al.^[5], which are denoted on all plots in Figure 2.7. Outside this range, the parameters were extrapolated. The δ -ferrite phase is present in the mushy zone at very high temperatures. However, for the carbon contents in this study ($\%C > 0.2$), δ -ferrite exists only at solid fractions below 0.5 at which the steel does not transmit stresses; therefore, the mechanical properties of δ -ferrite did not require consideration. The reference strain rate and reference strain (shown in Figures 2.7(c) and 2.7(d), respectively), were calculated from the expressions given below Eq. [2.17] and the values in Table 2.2. The reference strain rate is shown for a representative carbon content of 0.25% (which is needed to calculate A); for the finite element simulations, the measured carbon content (shown in Table 2.1) was used.



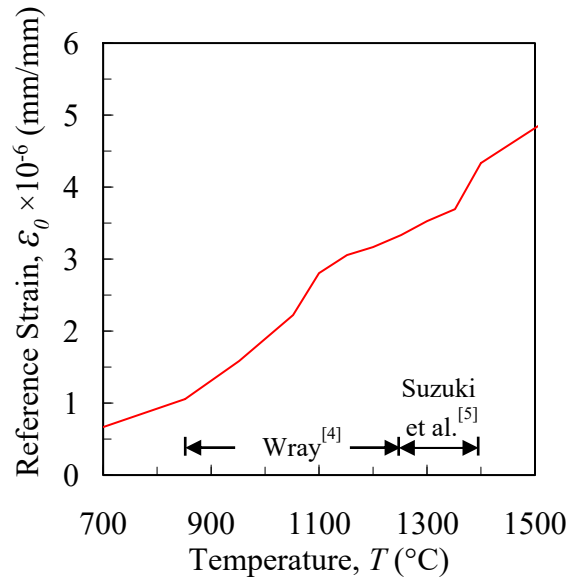
(a) Strain Rate Sensitivity and Strain Hardening Exponents



(b) Initial Yield Stress



(c) Reference Strain Rate



(d) Reference Strain

Figure 2.7 The strain rate and strain hardening exponents (a), initial yield stress (b), reference strain rate (c), and reference strain (d) as functions of temperature. Parameters were estimated from the experimental data of Wray^[4] (1123 K (850 °C) $\leq T \leq$ 1523 K (1250 °C)) and Suzuki et al.^[5] (1523 K (1250 °C) $\leq T \leq$ 1673 K (1400 °C)).

2.6 Stress Modeling Methods, Properties and Procedures for Bonded Sands and Cylinder and Bracket Castings

Constitutive Model for Bonded Sand

The bonded sands used in the mold and core are modeled using the Drucker-Prager Cap model, which is commonly used to model granular media that exhibit pressure-dependent yielding. The model is taken from the ABAQUS[®][30] material library and reviewed here for completeness.

The Drucker-Prager Cap model is defined by a multi-surface yield function, shown in the meridional (i.e., deviatoric stress vs. pressure) plane in Figure 2.8(a). The shear failure (F_s) surface is defined as

$$F_s = t - p \tan \beta - d = 0 \quad [2.20]$$

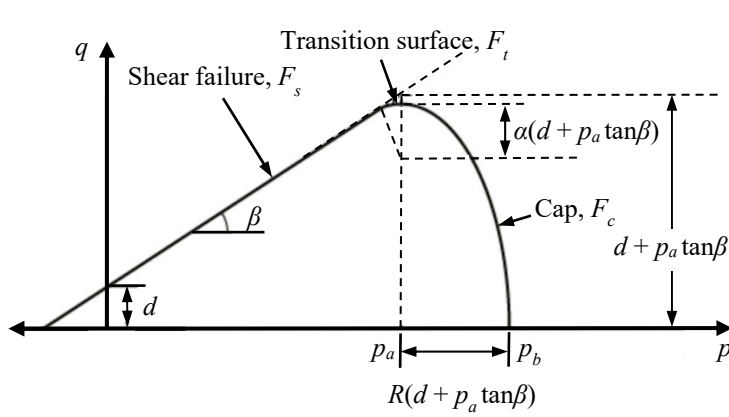
where, $p = -1/3 \text{trace}(\boldsymbol{\sigma})$ is the pressure and $\tan \beta$ is the slope of the failure surface. The cohesion parameter (d), defines the intersection of the shear failure surface with the deviatoric stress axis. The deviatoric shear stress (t) is given as

$$t = \frac{1}{2}q \left[1 + \frac{1}{K} - \left(1 - \frac{1}{K} \right) \left(\frac{r}{q} \right)^3 \right] \quad [2.21]$$

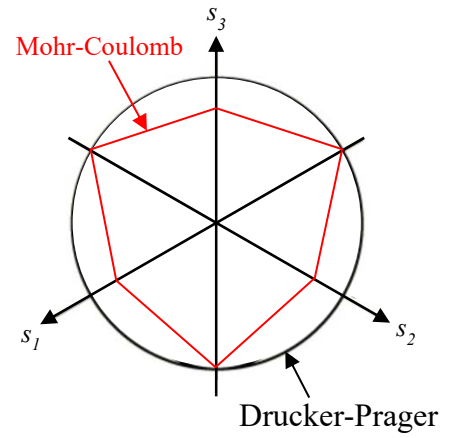
In Eq. [2.21], $q = \sqrt{3/2(\boldsymbol{\tau} : \boldsymbol{\tau})}$ is the von Mises stress and determined from the deviatoric stress tensor, $\boldsymbol{\tau} = \boldsymbol{\sigma} + p\mathbf{I}$, where \mathbf{I} is the second order identity tensor. Also, $r = (9/2\boldsymbol{\tau} : \boldsymbol{\tau} \cdot \boldsymbol{\tau})^{1/3}$ is the third stress invariant, and K governs the shape of the yield surface in the deviatoric stress plane (see Figure 2.8(b)). For the present study, $K=1$ (i.e., a circle in the deviatoric plane) is required for ABAQUS[®]/explicit, which reduces Eq. [2.21] to $t = q$. The Drucker-Prager yield surface is taken to circumscribe the Mohr-Coulomb failure envelope in the deviatoric stress space.

The cap (F_c) and transition (F_t) surfaces in Figure 2.8(a) are defined, respectively, as

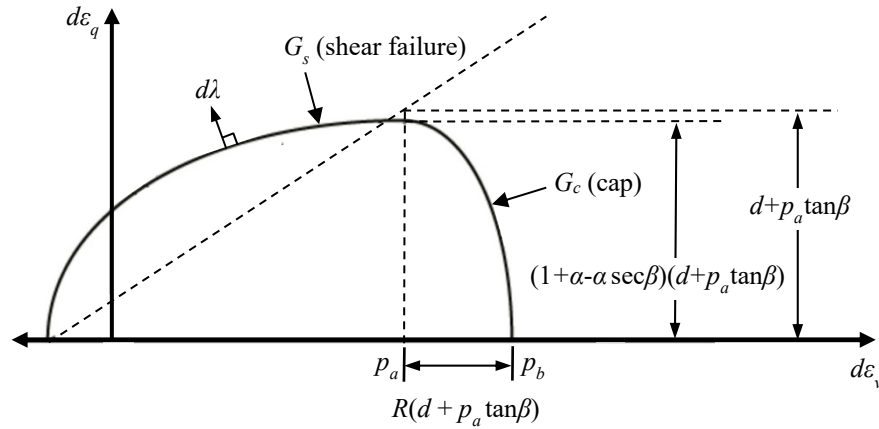
$$F_c = \sqrt{[p - p_a]^2 + \left[\frac{Rt}{(1 + \alpha - \alpha/\cos \beta)} \right]^2} - R(d + p_a \tan \beta) = 0 \quad [2.22]$$



(a) Yield Surface in Meridional Plane



(b) Yield Surface in Deviatoric Plane



(c) Plastic Potential

Figure 2.8 The Drucker Prager Cap yield surface shown in the meridional (a) and deviatoric (b) planes. The plastic potential (c) uses associated and non-associated flow rules for the cap and failure surfaces, respectively.

and

$$F_t = \sqrt{[p - p_a]^2 + \left[t - \left(1 - \frac{\alpha}{\cos \beta} \right) (d + p_a \tan \beta) \right]^2} - \alpha(d + p_a \tan \beta) = 0 \quad [2.23]$$

where R is the eccentricity of the elliptical cap, α is a small number (typically 0.01 to 0.05) that defines the shape of the transition surface, and the evolution parameter (p_a) is defined as

$$p_a = \frac{p_b - Rd}{(1 + R \tan \beta)} \quad [2.24]$$

where p_b is the hydrostatic compressive strength and defines the intersection of the cap with the pressure axis in Figure 2.8(a). The hardening/softening behavior is governed by the evolution of p_b with plastic volumetric strain increments and was determined for this study with a 1-D compression test (see *Properties for Bonded Sands* section below).

The plastic strain increment ($d\epsilon_{pl}$) is determined from the flow rule, given as

$$d\epsilon_{pl} = d\lambda \frac{\partial G}{\partial \sigma} \quad [2.25]$$

In Eq. [2.25], $d\lambda$ is the magnitude of the plastic strain increment, G is the plastic potential, and $\partial G/\partial \sigma$ is the direction of the plastic flow. The plastic potentials for the failure surface (G_s) and cap surface (G_c) are shown in Figure 2.8(c) and given as

$$G_s = \sqrt{[(p_a - p)\tan \beta]^2 + \left[\frac{t}{(1 + \alpha - \alpha/\cos \beta)} \right]^2} \quad [2.26]$$

and

$$G_c = \sqrt{[p_a - p]^2 + \left[\frac{Rt}{(1 + \alpha - \alpha/\cos \beta)} \right]^2} \quad [2.27]$$

Note that in Eqs. [2.26] and [2.27] no new parameters have been defined. The parameters used to characterize the yield surface also define the plastic potential. Comparing Figures 2.8(a) and (c), it is obvious that $F_c = G_c$, which implies associated flow in the cap region. For the shear failure region, a non-associated flow rule is used, as the yield surface is different from the plastic potential. This is typical for materials that exhibit dilative behavior.

Properties for Bonded Sands

In this study, core expansion was induced by high heating rates near the mold-metal interface, which suggests the high-temperature mechanical properties play an important role for predicting distortions. Unfortunately, no commercially available mechanical testing machines possess the necessary high-temperature measurement capabilities. Consequently, no high-temperature mechanical testing was performed in this study. Instead, as a first estimate, the high-temperature mechanical properties of the bonded sands were determined from room temperature tests on un-bonded, densely-packed sands. Using un-bonded sand to estimate properties is reasonable because pyrolysis of the binder essentially reduced the molds and cores to un-bonded sands at high temperatures.

Several properties (β , α , R , ν) were set to constant values for all temperatures. Based on the findings of Saada et al.^[18], the friction angle (β) was held constant. The shape parameter for the transition surface ($\alpha = 0.01$) only governs a small portion of the yield surface and will have little impact on the simulation results. The eccentricity ($R = 0.45$ ^[39])

defines the ratio of the major to minor axis for the elliptical cap surface. Due to the limited data available in the literature, this value was taken as a constant. Poisson's ratio ($\nu=0.3$) was also taken as a constant.

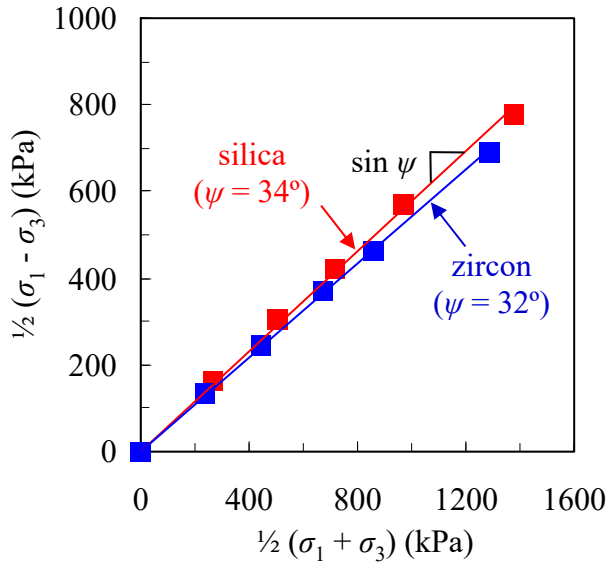
The remaining properties (E and d) were estimated over the entire casting temperature range using the following procedure. The room temperature bonded sand properties were linearly decreased to their high-temperature values at some critical temperature, T_{crit} , and then held constant for all $T > T_{crit}$. The critical temperature represents the onset of pyrolysis of the binder, after which the mold and core are transformed to un-bonded sands. Although the properties can be expected to exhibit some degree of temperature dependency above T_{crit} , such variations are likely minimal over the temperature range for which distortions occurred. Therefore, using constant values above T_{crit} is a reasonable first estimate.

A single temperature dependent Young's modulus (E) was used for the silica and zircon bonded sands. The room temperature ($E_{R.T.} = 3403$ MPa) and high temperature ($E_{H.T.} = 60$ MPa) values were taken from Thole and Beckermann^[17] and Hettler and Vardoulakis^[40], respectively.

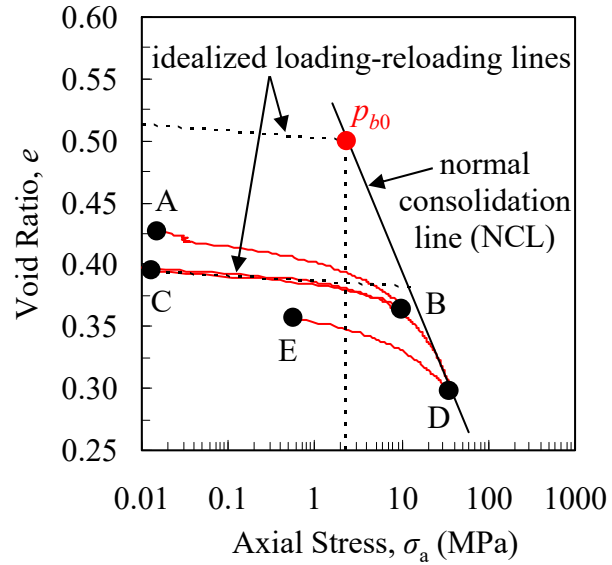
The shear failure surface parameters (β and $d_{H.T.}$) for the Drucker-Prager Cap model were estimated from drained triaxial compression tests. An un-bonded cylindrical test specimen (70 mm long and 38 mm diameter) was contained in a 1-mm thick elastomer membrane during the test and housed in a triaxial cell. The test was carried out in 2 steps. First, a confining pressure was applied by filling the triaxial cell with water and then pressurizing it. This created a hydrostatic stress state, i.e., $\sigma_1 = \sigma_2 = \sigma_3$ (where the subscripts denote the principal directions. As is customary for geological materials, compressive stresses are defined here as positive values). Next, a displacement-controlled piston compressed the test specimen in the axial direction at a constant rate of 0.01 mm/min until a peak axial force (F) was measured. The peak axial stress, σ_1 , was calculated by dividing the peak axial force by the cross-sectional area of the specimen and adding the result to the confining pressure, i.e., $\sigma_1 = F/A + \sigma_3$. In total, 5 tests were performed for both sands, each at a different confining pressure (100, 200, 300, 400, and 600 kPa). For each test, a Mohr's circle can be constructed from the confining pressure, σ_3 , and peak axial stress, σ_1 . The friction angle can then be determined using the Mohr-Coulomb failure criterion. However, obtaining a best-fit failure envelope is difficult using this method. A convenient alternative is to plot the triaxial data on a modified Mohr-Coulomb diagram in which $1/2(\sigma_1 - \sigma_3)$ is plotted versus $1/2(\sigma_1 + \sigma_3)$. This diagram is advantageous because a single point represents each test, which enables a best-fit line to be easily constructed. Since dry sand has no cohesion, the cohesion parameter was set to zero by forcing the best-fit line through the origin. The results of the silica and zircon triaxial tests are shown on the modified Mohr-Coulomb diagram in Figure 2.9(a). The angles of the best-fit lines for the silica and zircon sand tests were found to be $\psi = 35^\circ$ and 33° , respectively. Then, using the relation

$$\phi = \sin^{-1}(\tan \psi) \quad [2.28]$$

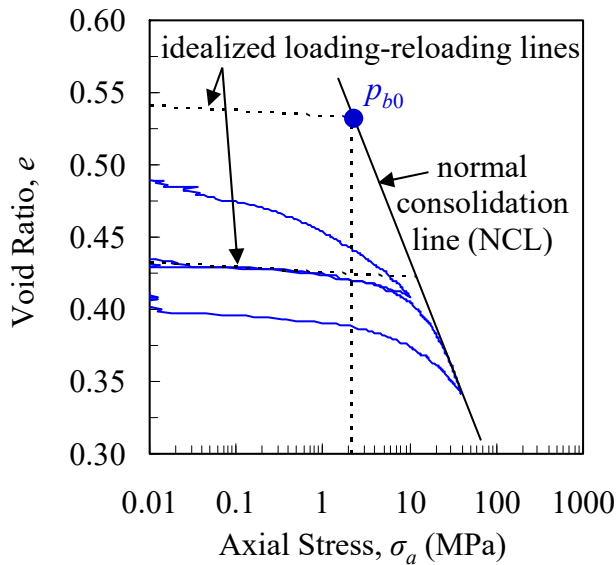
the Mohr-Coulomb friction angles were calculated as $\phi = 45^\circ$ and 40° for silica and zircon,



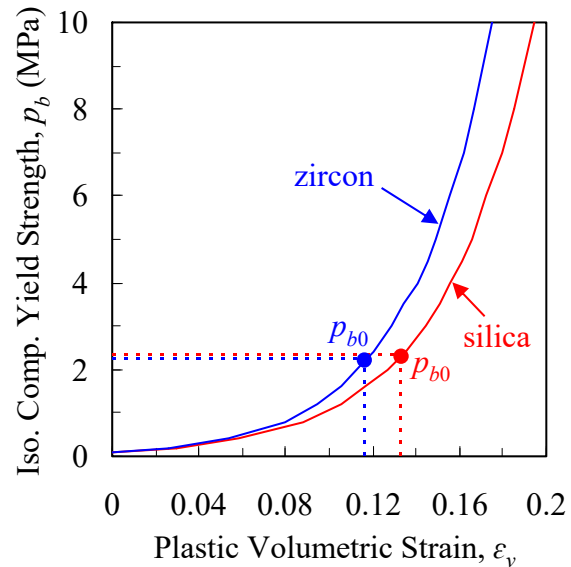
(a) Modified Mohr-Coulomb Diagram



(b) 1-D Compression Test for Silica Sand



(c) 1-D Compression Test for Zircon Sand



(d) Isotropic Compressive Yield Strength vs. Plastic Volumetric Strain

Figure 2.9 Friction angles (ψ) were determined from the Modified Mohr-Coulomb diagram (a). 1-D compression test results for silica (b) and zircon (c) sands were used to determine the hardening behavior (d).

respectively. Finally, the Drucker-Prager friction angle was calculated using the relation

$$\tan \beta = \frac{6 \sin \phi}{\sqrt{3}(3 - \sin \phi)} \quad [2.29]$$

to give $\beta = 55^\circ$ and 52° for silica and zircon, respectively. Conversion of the cohesion parameter from the modified Mohr-Coulomb diagram to the high temperature Drucker-Prager cohesion resulted in $d_{H.T.} = 0$ for both sands. Eq. [2.29] assumes the Drucker-Prager yield surface circumscribes the Mohr-Coulomb failure surface in deviatoric space, as shown in Figure 2.8(b). The room temperature cohesion ($d_{R.T.}$) was estimated through a finite element stress analysis performed on a uniaxial tension test for bonded sand^[16]. Starting at 1 MPa, $d_{R.T.}$ was incrementally increased until the maximum observed tensile strength could be predicted. This occurred at $d_{R.T.} = 1.85$ MPa. Since the Drucker-Prager Cap model in ABAQUS® predicts perfect plasticity in tension, the maximum predicted stress is also the yield stress.

Hardening/softening behavior for the Drucker-Prager Cap model is associated with plastic volumetric strains and was determined for both sands from room temperature 1-D compression tests. An un-bonded cylindrical test specimen (25.4 mm height and 38.1 mm diameter) was compressed in the axial direction at a rate of 0.254 mm/min. The sample was housed in a rigid ring to prevent displacement in the radial direction. Initial bulk densities (ρ_{b0}) were 1858 kg/m³ and 3169 kg/m³ for the silica and zircon sands, respectively. Although the test specimens were not packed, their bulk densities were higher than the measured room temperature core bulk densities used in the experiments (1751 kg/m³ for silica and 3062 kg/m³ for zircon). These differences are attributed to the binder in the cores, which reduced the volume fraction of sand grains. 1-D compression test results are plotted as void ratio (e) vs. $\log p$ for the silica and zircon sands in Figures 2.9(b) and (c), respectively. The void ratio is defined as the ratio of void volume (V_v) to solid volume (V_s) for the aggregate, i.e., $e = V_v/V_s$. The initial void ratio (e_0) is calculated from the initial bulk density using the relation $e_0 = (\rho_p/\rho_{b0}) - 1$, where ρ_p is the particle density ($\rho_p = 2650$ kg/m³ and 4700 kg/m³ for silica and zircon respectively). The tests were carried out in the sequence (A-B-C-D-E) shown in Figure 2.9(b). The test specimen ($e_0 = 0.424$) was loaded in segment A-B, unloaded in B-C, loaded again in C-D, and unloaded in D-E. From this procedure, a family of nearly-parallel curves can be seen in Figures 2.9(b) and (c) at pressures less than 10 MPa. In particular, segment B-C contains one unloading line and one reloading line, and both follow the same path. This implies that the unloading-reloading lines characterize the elastic response of the sand. This segment was then used as a guide to generate an idealized loading-reloading curve, whose slope is assumed to be independent of the initial bulk density. The idealized loading-reloading curves were then shifted upward to correspond to the initial void ratios from the experiments (0.52 for silica and 0.54 for zircon).

The normal consolidation line was determined from the slope of the 1-D compression curve at high pressures and assumed to be linear on $\log p$. In order to include all pressures associated with sand casting, the curve was extrapolated to low pressures, as shown in Figures 2.9(b) and (c). The position of the cap (see Figure 2.8(a)) at the onset of casting represents the initial hydrostatic compressive strength, p_{b0} , and is determined by the intersection of the idealized loading-reloading line and the normal consolidation line in

Figures 2.9(b) and (c). Any increase or decrease in p_b from the initial state is constrained to lie on the normal consolidation line. The change in void ratio is calculated from the plastic volumetric strain increment ($\Delta \varepsilon_v^{pl}$) using the relation $\Delta \varepsilon_v^{pl} = (e_2 - e_1)/(1 + e_1)$, where the subscripts denote the initial (1) and final (2) states. Thus, the evolution of p_b with $\Delta \varepsilon_v^{pl}$ defines the hardening/softening behavior for the bonded sands. This relation is plotted for both sands in Figure 2.9(d). It is clear from the figure that the compressive strength for zircon sand is higher than for silica sand.

Stress Simulation Procedures for Cylinder and Bracket Castings

Stress simulations of the cylinder and bracket casting experiments were performed using the general purpose finite element code ABAQUS[®]/explicit. An explicit integration scheme was chosen to avoid convergence issues associated with material softening when the material yields on the Drucker-Prager shear failure surface. The time step using the explicit method is conditionally stable. The critical time step is $\Delta t \leq 2/\omega_{\max}$, where ω_{\max} is the highest frequency (i.e., largest eigenvalue) of the system. This stability limit can be rewritten as

$$\Delta t = \min \left(\frac{L_e}{c_d} \right) \quad [2.30]$$

where L_e is the characteristic element dimension and is derived from an analytic upper bound expression for the maximum element eigenvalue. The effective dilatational wave speed (c_d) of the material is defined as

$$c_d = \sqrt{\frac{\lambda + 2\mu}{\rho}} \quad [2.31]$$

In Eq. [2.31], $\lambda = E\nu/[(1+\nu)(1-2\nu)]$ is the first Lamé constant, μ is the shear modulus, and ρ is the material density.

Inputting the mold and steel properties into Eq. [2.13] gives very large dilatational wave speeds that limit the time step and lead to impractical simulation times. For casting processes, however, inertial forces are not important, as deformations occur at rates much lower than the dilatational wave speed. Therefore, the time step may be significantly increased without affecting the simulation results. This is achieved in ABAQUS[®]/explicit through “mass scaling” in which the mass is artificially increased. To ensure that mass scaling does not significantly affect the results, the ratio of kinetic energy to total energy in the simulation should not exceed 5%.

For the simulation model of the cylinder, the cope was excluded because it did not contact the steel during casting. Contact interactions between the cylinder casting, core, and drag were defined using the general contact algorithm in ABAQUS[®]/explicit, which employs a penalty method. Friction between the contact surfaces was found to have a negligible impact on distortions and set to zero. Zero displacement boundary conditions

(i.e., $u_x=0$, $u_y=0$, $u_z=0$) were specified on the bottom of the drag to prevent rigid body translations and rotations. First-order tetrahedral elements were used for the entire model. Taking advantage of symmetry, only $\frac{1}{4}$ of the cylinder geometry was modeled. For the simulation model, the casting consisted of approximately 10,000 nodes and 50,000 elements, whereas the mold and core contained 17,000 nodes and 90,000 elements. Simulations were performed on an Intel® Xeon® E5-2687W v2 processor containing 8 cores with a CPU clock speed of 3.4 GHz. Simulation run times were approximately 2 hours.

Stresses and strains in the bracket and mold were calculated using the general purpose finite element code ABAQUS®. An explicit time integration scheme (i.e., ABAQUS®/explicit) was used for the present study in order to avoid numerical difficulties associated with the material softening that accompanies dilative behavior. For this strategy, the time step is conditionally stable and limited by how fast stresses can propagate through the material. The minimum time step is determined by the characteristic element dimension, elastic mechanical properties, and material density. In general, however, this calculation results in a very small time step, which leads to impractical computation times. For quasi-static processes, however, distortions occur at rates much lower than the speed at which the stress wave propagates. For situations such as these, mass scaling is employed in order to increase the stable time increment. A detailed explanation of how the time step is determined can be found in the ABAQUS® documentation^[30].

The finite element model is depicted in Figure 2.10. Taking advantage of symmetry, only $\frac{1}{2}$ of the experimental geometry was modeled. A symmetry plane was

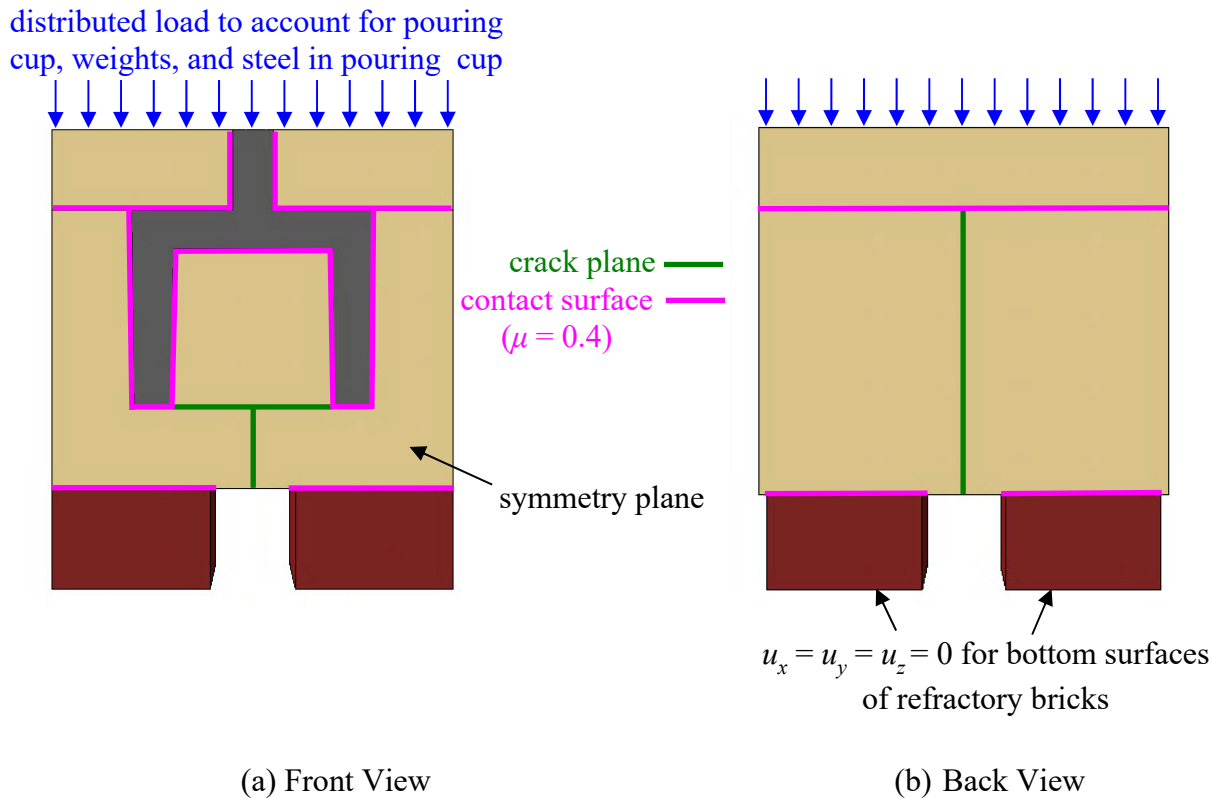


Figure 2.10 The finite element model included body forces, contact between the casting, mold, and refractory bricks (pink lines), crack planes (green lines), and a distributed load on top of the cope. Using the symmetry plane in (a), only $\frac{1}{2}$ of the geometry was modeled. Zero displacement boundary conditions were specified on the bottoms of the refractory bricks to prevent rigid body translations and rotations.

defined at the vertical casting mid-plane. The general contact algorithm in ABAQUS[®]/explicit was used to model the interaction between the casting and mold as well as between the mold and refractory bricks (contact surfaces are denoted by pink lines in Figure 2.10). Friction between the contact surfaces was modeled using a friction coefficient of 0.4. The model was constructed using 8-node linear brick elements. The casting and mold consisted of approximately 12,000 and 50,000 nodes, respectively. Simulations were performed on an Intel[®] Xeon[®] E5-2687W v2 processor containing 8 cores with a CPU clock speed of 3.4 GHz. Run times were approximately 8 hours. Initially, the crack planes in Figure 2.10 were not modeled in the stress simulation. The reason for its inclusion in subsequent simulations is explained in the results section 3.3 for the bracket castings below.

2.7 Description and Procedures for the Case Study of Dimensional Predictions

The part analyzed in this study is a drag socket, which is used on a mining excavator to splice cables together. It was cast at the Bradken foundry in London, Ontario. The casting (shown in Figure 2.11) has outer dimensions (in meters) of $1.91 \times 0.29 \times 0.6$ ($6.27 \times 0.95 \times 1.97$ ft) and weighs approximately 940 kg (2068 lbs). The drag socket contains several characteristics that makes it susceptible to distortions. For example, cores are needed to create the hollow interior of the main body as well as the two holes on the right side of Figure 2.11(b). Uneven cooling is also likely to generate distortions in the varying section thicknesses of the casting as well as the gating and risers (which are not shown).

A dimensional analysis was performed after shakeout, for which several casting features were measured. Using these measurements, pattern allowances (*PA*) were then calculated using the Eq. [1.1]. In total, ten features were selected from the part drawing and are numbered in Figure 2.11. The measured pattern allowances are summarized in Figure 2.12. Features 1, 2, 4, and 8 have pattern allowances greater than the patternmaker's shrink. This result can be explained by mold expansion. From Figure 2.11, it can be seen that these features are measured on the outer surface of the casting. During solidification, the rapidly heating mold expands and pushes the outer walls of the casting inward to reduce feature lengths (i.e., pattern allowances are increased). These features are unconstrained and therefore, will shrink an additional 2.1% (i.e., the patternmaker's shrink) after the initial "push-in" of the outer walls, resulting in pattern allowances greater than the patternmaker's shrink. Similarly, features 3, 7, and 10 are also measured from the outer surface and can be expected to experience a reduction in length during solidification. However, these features are also influenced by core restraint. In contrast to mold expansion, distortions created from core restraint increase the feature lengths (i.e., reduce pattern allowances). Therefore, for features 3, 7, and 10, distortions created by mold expansion and core restraint distortions cancel each other out to some degree. For these situations, the pattern allowances should be viewed with caution; even if the patternmaker's shrink is measured, significant distortions may have occurred but are hidden due to the "canceling out" explained above. Therefore, although the measured pattern allowances are close to the patternmaker's shrink for features 7 and 10 (1.95%), larger distortions may have occurred and potentially caused damage in the part. For situations in which features are measured on internal surfaces (i.e., features 5, 6, and 9), mold expansion increases the feature lengths (i.e., reduces pattern allowances). For example, mold expansion will expand the diameter

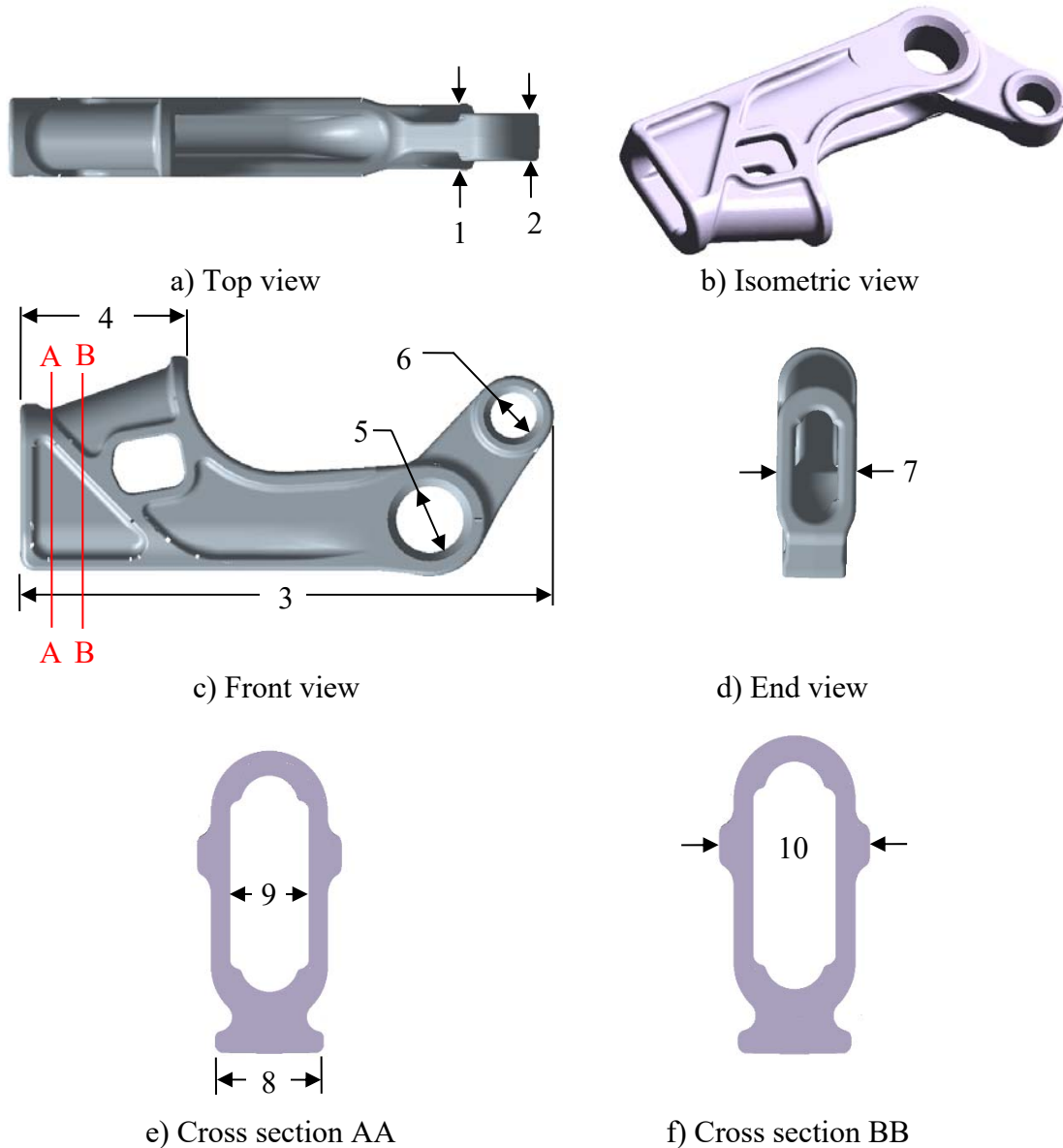


Figure 2.11 Casting geometry and feature locations.

of the large hole (feature 5) in Figure 2.11(c). Because core restraint will also expand the diameter, pattern allowances for features measured on internal surfaces should always be less than the patternmaker's shrink. This is indeed the case for this study, as the maximum pattern allowance of features 5, 6, and 9 is 0.62%. Because the features are affected by different phenomena and in different ways, their pattern allowances vary over a large range, as seen in table 1 ($-0.89 < PA < 3.11$). For validation purposes, this variation is desirable for this case study.

Temperatures were predicted using the casting simulation software package MAGAMSOFT®. The baseline input parameters for the simulations presented for the experiments and case studies (including temperature dependent thermophysical properties for the mold and casting, solid fraction, latent heat, and interfacial heat transfer coefficient)

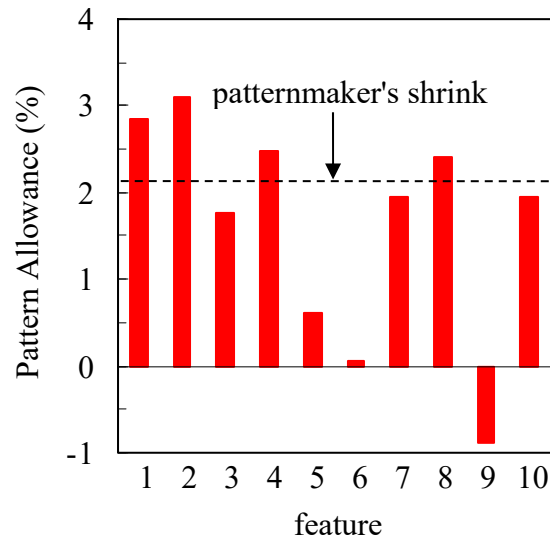


Figure 2.12 Measured pattern allowances for case study feature dimensions

are summarized in Figures 2.13 to 2.15. All components of the casting system (i.e., mold, casting, cores, risers, chills, etc.) were included in the simulation. Predicted temperature fields were output at a sufficient number of time steps to give a smooth temperature profile at every location in the model. The results were mapped onto the finite element mesh used in the stress simulations.

To predict distortions, stress simulations were performed using the general purpose finite element code ABAQUS®. The mold, gating, and risers were included in the simulations, as they their contributions to distortions could not be discounted. However, in order to protect the confidentiality of the casting design, these components will not be shown in the results. The constitutive models for the steel and bonded sands are described in sections 2.5 and 2.6. Due to its complex geometry, tetrahedral elements were used to

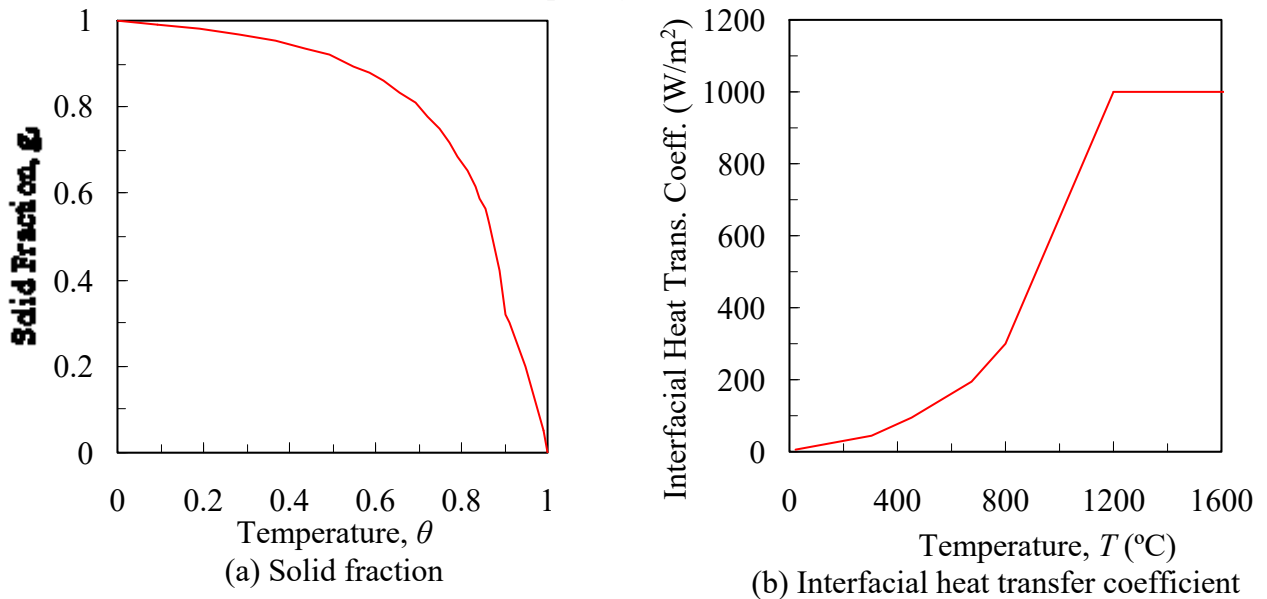


Figure 2.13 Solid fraction (a) and interfacial heat transfer coefficient (b).

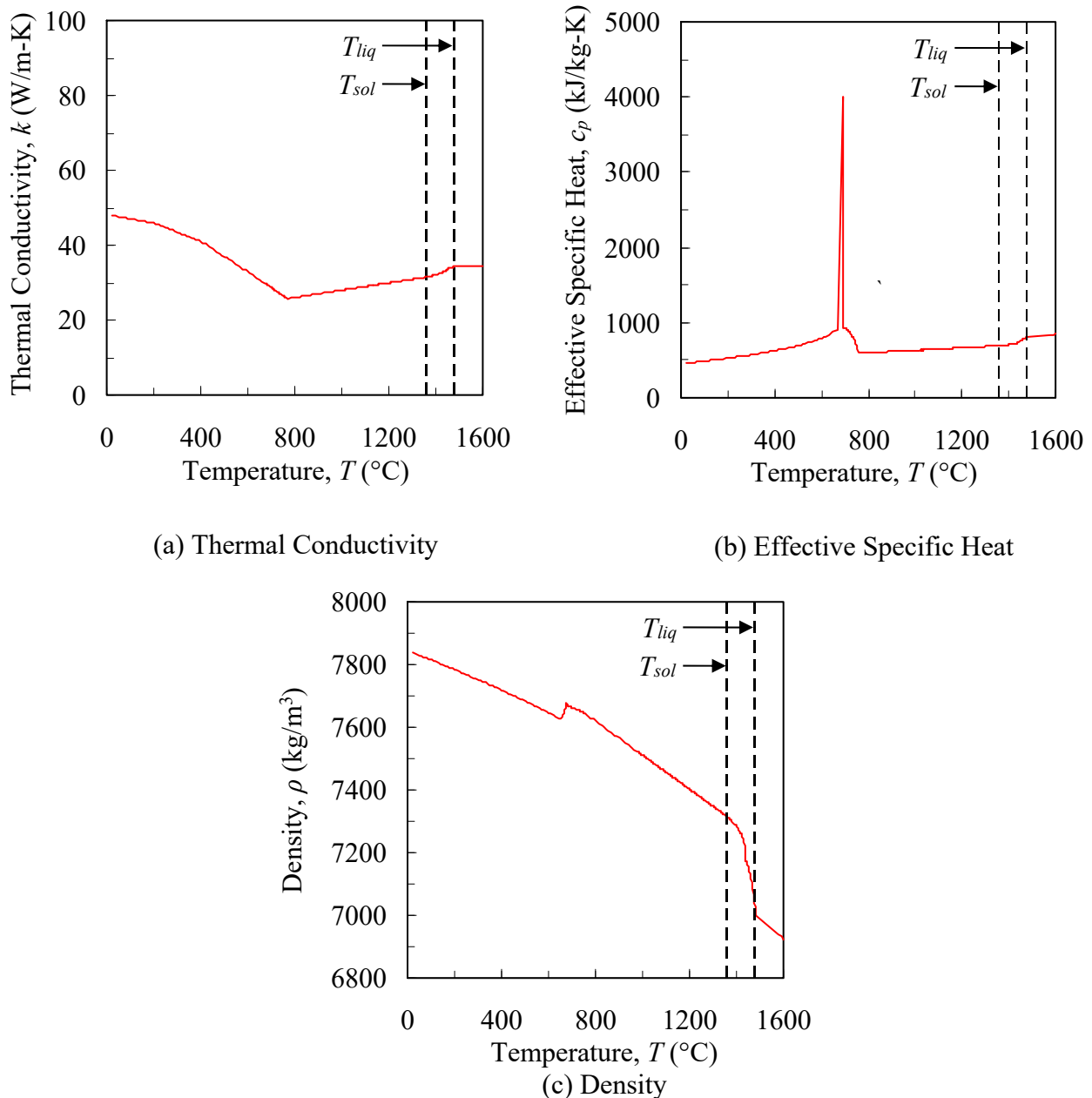


Figure 2.14 Thermophysical properties for the steel.

build the mesh. The model contained approximately 200,000 nodes and 1.1 million elements.

To quantify the distortions created by each phenomenon (i.e., mold expansion, core restraint, uneven cooling), three simulations were performed. The first simulation (termed “thermal”) calculated thermal strains only. The pattern allowances predicted in this simulation are equal to the patternmaker’s shrink. The thermal simulation serves as a baseline; any predicted feature length that deviates from that in the thermal simulation is a distortion. In the second simulation (termed “casting only”), the outer mold was excluded. Here, distortions due to mold expansion and core restraint are not considered. Thus, distortions can only be created by uneven cooling in this simulation. The third simulation

(termed “full”) includes the complete casting system and therefore, considers all the phenomena responsible for distortions. The predicted pattern allowances from this simulation will be compared to the measurements to determine the predictive capability of the computational model.

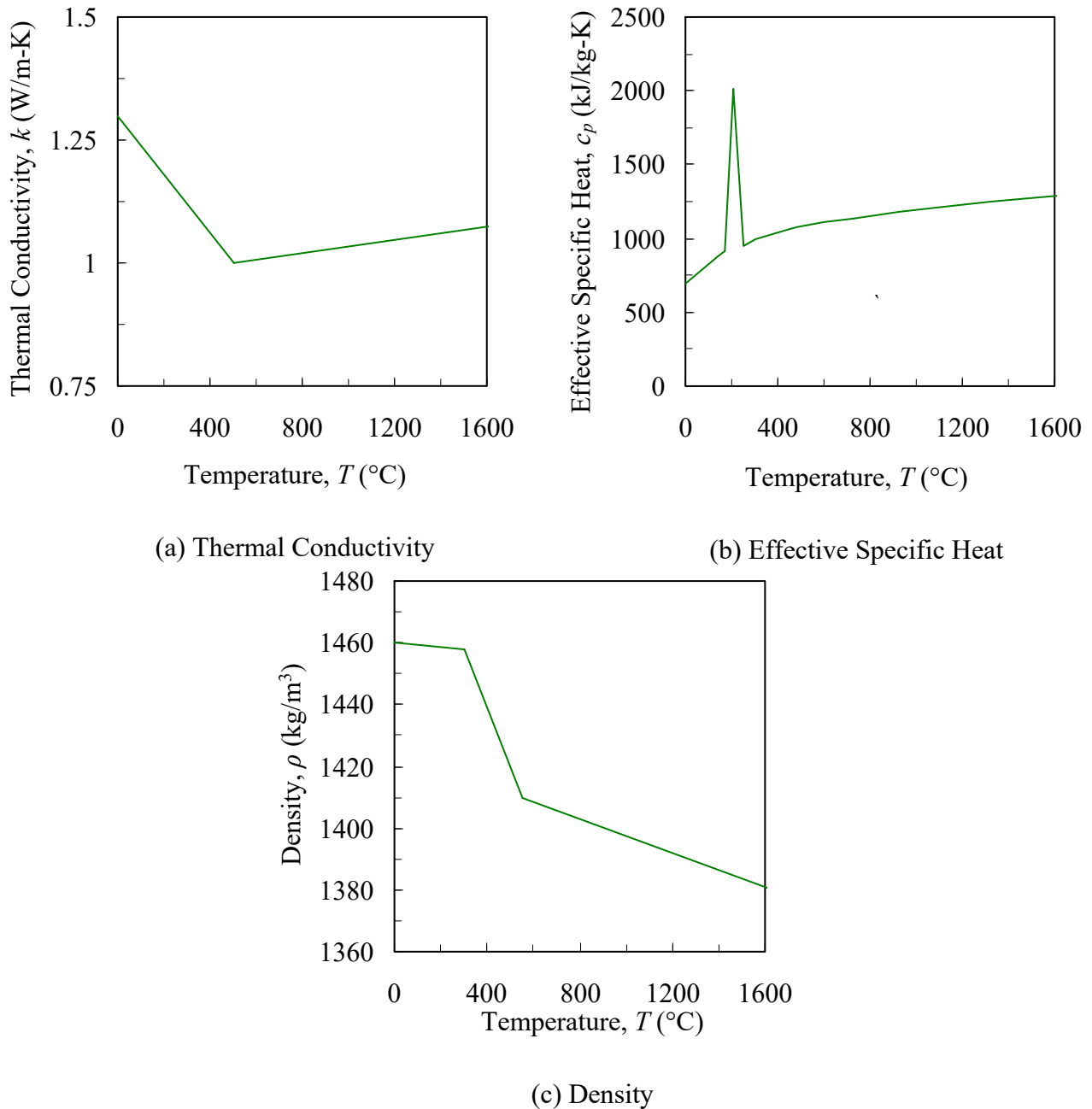


Figure 2.15 Thermophysical properties for the bonded sand.

3. Results and Discussion

3.1 Experimental and Simulation Results for Bar Castings

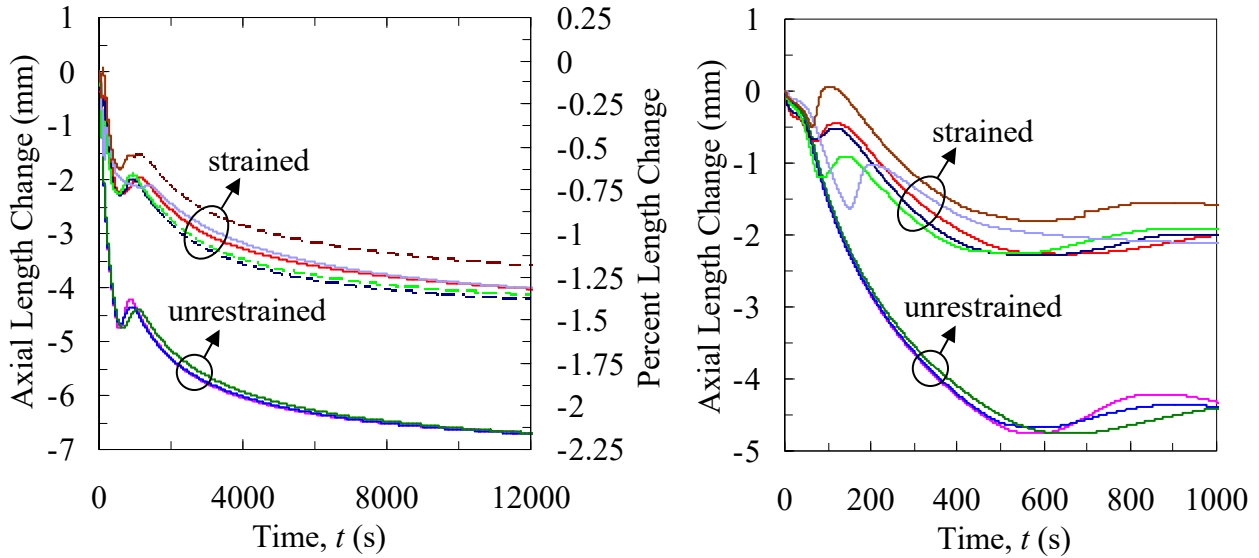
Bar Casting Experimental Results

A total of eight casting experiments, 5 strained and 3 unrestrained, were performed. In order to identify individual bars, a numbering system was adopted (e.g., strained 1, unrestrained 1). In addition, a unique color was assigned to each bar in order to distinguish between curves on all results plots. These identifiers are also provided in Table 2.1.

Since type B thermocouples lose their accuracy at room temperature, data was acquired until the castings cooled to approximately 373 K (100 °C). The time range (12000 s) needed to record the results down to this temperature is henceforth referred to as the complete time scale. Several important features occurring at early times are difficult to see on this scale. Therefore, intermediate and initial time scales (showing the initial 1000 s and 250 s, respectively) are also utilized to present the experimental results.

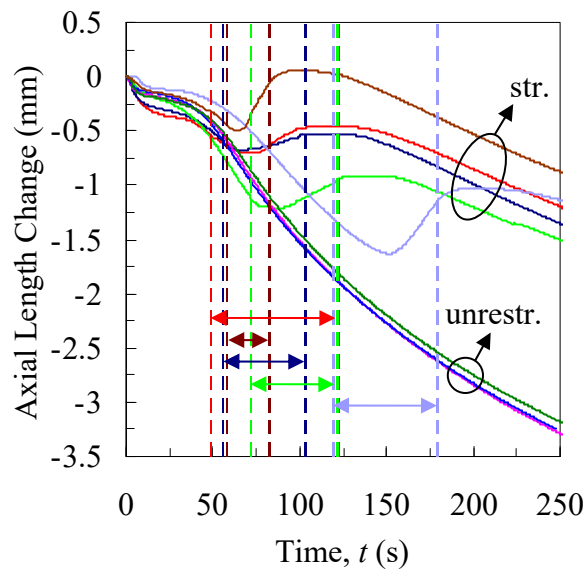
The measured axial length changes, plotted as a function of time, are shown for all experiments in Figure 3.1. For the unrestrained bar experiments, excellent reproducibility of the measurements can be seen, as the three curves essentially lie on top of each other. Starting from the initial time ($t=0$ s), the unrestrained axial length decreases (as a result of thermal contractions) until approximately 500 s. At this time, a volumetric expansion (due to the solid-state phase transformation from austenite to pearlite and α -ferrite) occurred and is manifested as a positive slope beginning at 600 s. Because the bar temperatures varied spatially, this transformation commenced at different times throughout the casting. As a result, the axial length increases over an expanded period of approximately 300 s, after which it decreases monotonically until room temperature.

For the strained bar experiments, the restraint force impacted the axial length change substantially (see Figure 3.1). Initially, the axial lengths decreased similarly to those of the unrestrained bar experiments. However, shortly after the restraint force was applied, the strained bars elongated, which can be seen in Figure 3.1(c) as a positive slope for all strained curves. During this time, the strained and unrestrained curves diverge, as considerable viscoplastic strains were generated. The straining periods (i.e., the period during which the turnbuckle was engaged) for all strained bar experiments are represented in Figure 3.1(c) by double-headed arrows bounded by vertical dashed lines. Note that the onset of straining and the straining period varied among the 5 strained bar experiments. This was done on purpose in order to achieve different temperature ranges for the deformations. In other words, the five strained bar experiments were not intended to duplicate each other. At the end of the straining period, the axial length change remained constant for a brief period before continuing to decrease, as thermal strains dominated. At some point during cooling, the steel gained sufficient strength, after which yielding no longer occurred; at all ensuing times, the measured axial length changes for the strained bar experiments were due to thermal strains only. This can be clearly observed in Figure 3.1(a); after 1500 s, the strained and unrestrained bars contracted at the same rate (i.e., strained and unrestrained curves are parallel), which implies the presence of thermal strains only. Hence, for the experiments in which the quartz probes failed at late times (strained 2, 3, and 4), the displacements could be reconstructed (shown as dashed lines) with confidence by using data from other experiments (either strained or unrestrained).



(a) Complete Time Scale

(b) Intermediate Time Scale



(c) Initial Time Scale

Figure 3.1 Measured axial length change for the strained and unrestrained bar experiments plotted on complete (a), intermediate (b), and initial (c) time scales. The double-headed arrows that are bounded by vertical dashed lines of the same color in (c) represent the straining periods.

The measured restraint forces for the strained bar experiments are plotted as a function of time on the primary vertical axis in Figures 3.2(a) – 3.2(c). In addition, the nominal stresses (defined as the restraint force divided by the nominal cross-sectional area of the bar) are plotted on the secondary axis. At some time during the initial 200 s,

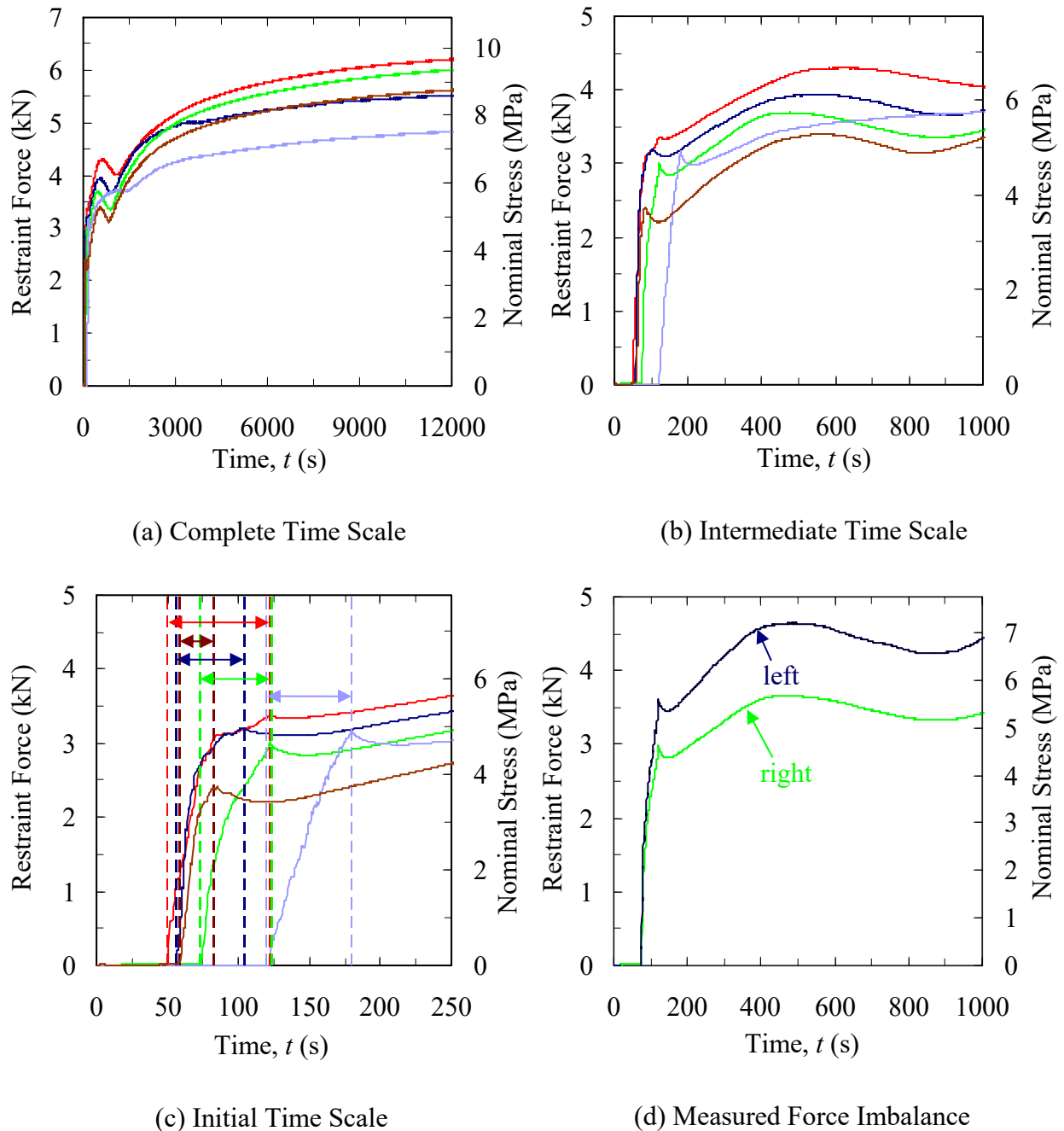


Figure 3.2 Measured restraint force for the strained bar experiments plotted on complete (a), intermediate (b), and initial (c) time scales. The double-headed arrows that are bounded by vertical dashed lines of the same color in (c) represent the straining periods. A measured force imbalance (strained bar 4 shown) was observed between the “right” and “left” load bolts (locations shown in Figure 2.1(a)) for all strained experiments.

engagement of the turnbuckle rapidly increased the restraint force (nominal stress) to roughly 3 kN (5 MPa). From the initial time scale in Figure 3.2(c), the straining period (shown as a double-headed arrow) for each experiment is determined as the time span from when the force begins to increase until a local maximum is reached. The decrease

immediately following this peak is due to stress relaxation resulting from creep effects. After this brief decrease, the ensuing thermal contractions acted to increase the restraint force, albeit at a slower rate. Once again, the effect of the solid-state phase transformation can be seen beginning at approximately 600 s, as volumetric expansion of the bar caused a relaxation in the restraint, resulting in a slight decrease of the restraint forces. Upon completion of this transformation, the forces continued to slowly increase up to 12000 s.

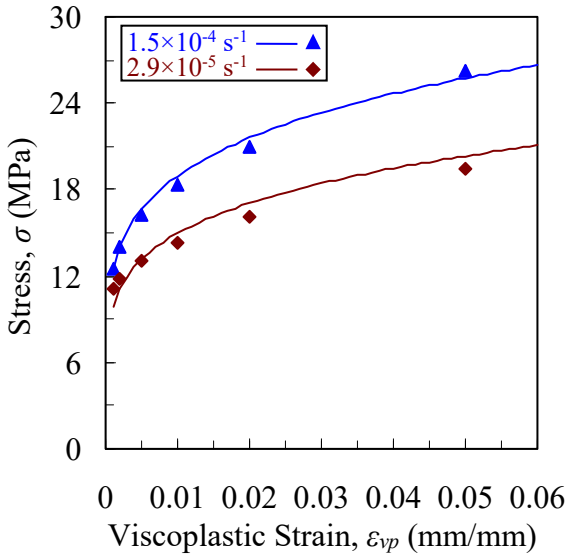
A comparison between the forces measured at either end of the casting revealed a difference. An example for one of the experiments (strained bar 4) is shown in Figure 3.2(d); the “left” and “right” curves refer to the location of the load bolts in Figure 2.1(a). The figure clearly shows that the left force is larger than the right force. The difference increases throughout the straining period to reach a value of approximately 1 MPa after 100 s. This difference (roughly 20%) is due to a sprue-mold interaction and will be accounted for by an additional boundary condition in the finite element simulations.

The strained 5 sprue diameter (1.5 inches) was larger than the other sprue diameters (1 inch). As a result, several differences can be seen on the displacement and force plots; due to a larger hot spot (directly under the sprue), a longer waiting period was required before engaging the turnbuckle to ensure the casting had reached coherency and could transmit stresses. This can be seen in Figure 3.2(c); the restraint force began increasing after 120 s, whereas the buildup of the other forces commenced earlier (between 50 s and 75 s). Accordingly, elongation of the bar also occurred later, as shown in Figure 3.1(c). Additionally, the larger sprue created larger temperature gradients along the axial direction of the bar. Therefore, the solid-state phase transformation for the entire bar (which is manifested as a “wobble” in the displacement curves) occurred over a longer period for strained bar 5 than the other bars, as seen in Figure 3.1(a).

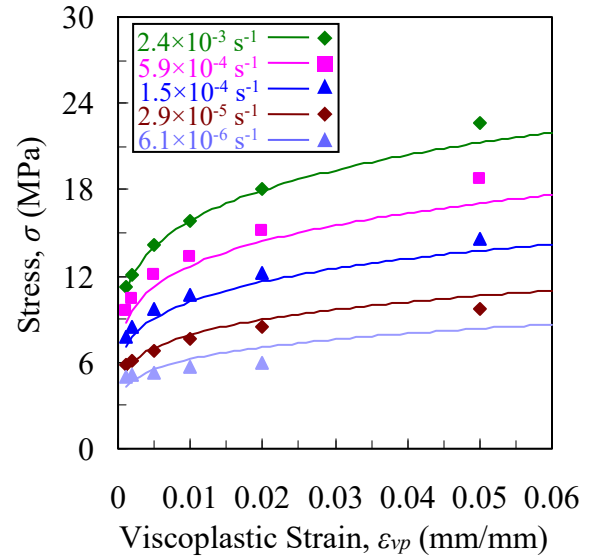
An example of measured temperatures for one of the experiments (strained bar 5) is shown in Figures 2.4(a) and 2.4(b). Due to space limitations, the thermocouple measurements for all experiments cannot be presented here. By taking a discrete time derivative of the measured temperatures, the cooling rate plot of Figure 2.4(c) is obtained. The liquidus temperature (T_{liq}), which represents the onset of solidification and latent heat release, is given by the initial local minimum in the cooling rate curve. As can be seen from Figure 2.4(c), the cooling rate increases with decreasing temperature, which can be attributed to a decreasing rate of latent heat release during solidification. The cooling rate reaches a local maximum when solidification is complete. The corresponding temperature is termed here, for simplicity, the solidus temperature (T_{sol}). Note that due to variations in the steel chemistry (see Table 2.1), the measured liquidus and solidus temperatures were different in each experiment.

Figure 3.3 shows examples of the excellent agreement between measured and predicted stress-strain curves that is obtained using the present viscoplastic parameters. The comparisons are for a 0.29 % carbon content, two different temperatures (1223 K (950 °C) and 1373 K (1100 °C)), and a large range of strain rates. Similar agreement was obtained for all data in Wray^[4] and Suzuki et al.^[5]

Recall from the axial length change measurements (Figure 3.1) that the strained and unrestrained curves are essentially parallel after 1500 s (i.e., after the solid-state phase transformation), and all strains at lower temperatures are purely thermal. Therefore, the stress model cannot be validated at temperatures below the austenite range using data from the present experiments, as no distortions occurred at temperatures below the solid state



(a) 950 °C



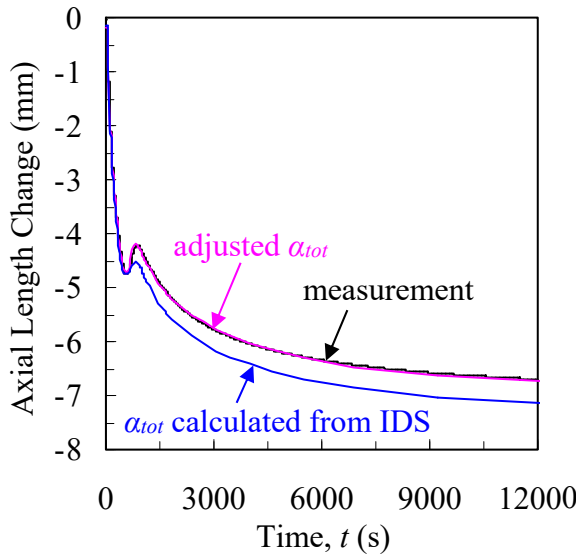
(b) 1100 °C

Figure 3.3 Comparison between measured (from Wray^[3]) and predicted stresses plotted at several strain rates as a function of viscoplastic strain at 1223 K (950 °C) (a) and 1373 K (1100 °C) (b).

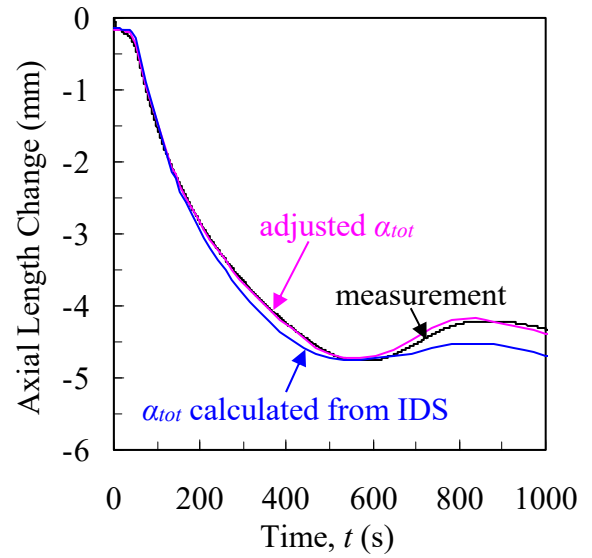
phase transformation. For this reason, viscoplastic parameters were not estimated below 973 K (700 °C). Rather, the initial yield stress, σ_0 , was set to an arbitrarily high value in order to prevent the prediction of viscoplastic strains at lower temperatures.

Unrestrained Bar Simulation Results

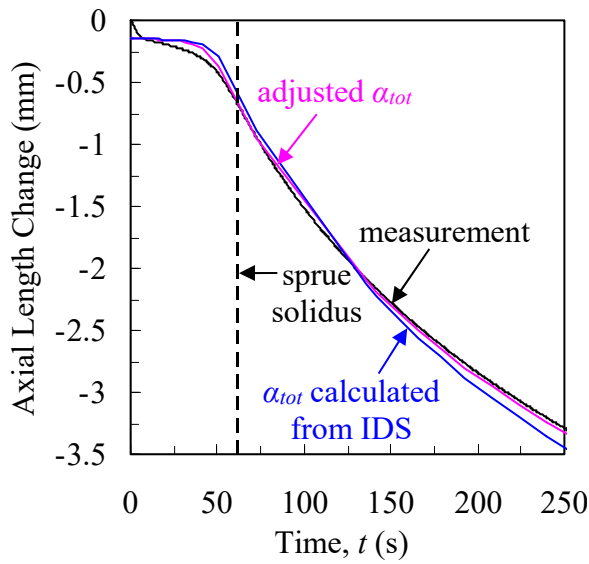
Length changes for the unrestrained bars owed to thermal strains only. The sole parameters contributing to the thermal strains are the total linear thermal expansion coefficient, α_{tot} , and the temperature for the onset of thermal contraction, T_{th} (see Eq. [9]). For the initial simulation, α_{tot} was determined from IDS using Eq. [10], whereas T_{th} was set to the measured solidus temperature (1683 K (1410 °C)). The resulting predicted axial length change (blue curves) for unrestrained bar 1 is plotted as a function of time and compared to the measured data (black curves) in Figure 3.4. The measured solidus temperature at the sprue location (see Figure 2.1) is denoted by the black vertical dashed line in Figure 3.4(c). One difference between the curves can be seen during the initial 10 s (see Figure 3.4(c)), before any substantial solidification of the steel occurs. The measured axial length decreases during the initial 10 s, whereas the predicted axial length remains nearly constant during this period. The measured rapid contraction during the initial 10 s can be attributed to expansion of the sand mold into the steel. This mold expansion accounts for a 0.15 mm decrease in the length of the bar. Since the mold was not included in the simulation, the effect of mold expansion could not be predicted. For this reason, the curves for the predicted length change in Figure 3.4 are shifted downward by 0.15 mm. After 10s, there are still several areas of disagreement between the measured and predicted



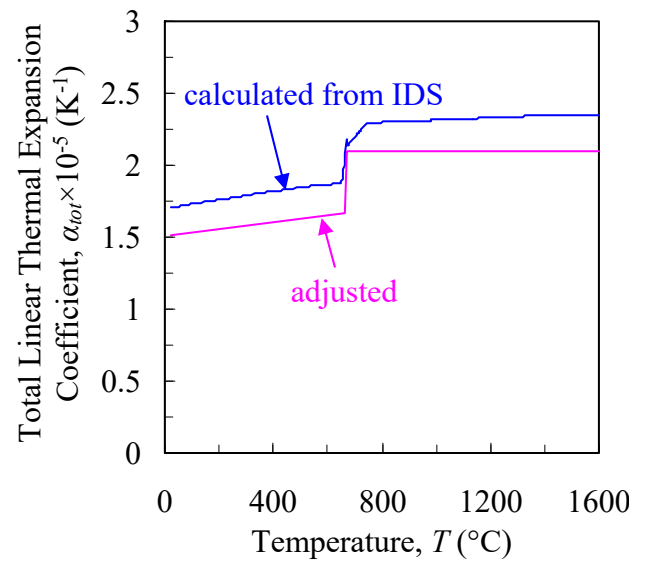
(a) Complete Time Scale



(b) Intermediate Time Scale



(c) Initial Time Scale



(d) Total Linear Thermal Expansion Coefficient

Figure 3.4 Measured and predicted axial length changes for the unrestrained bar 1 experiment plotted on complete (a), intermediate (b), and initial (c) time scales. (d) Total linear thermal expansion coefficient.

length changes when using the thermal expansion coefficient from IDS and the solidus temperature for the onset of contractions. The minor discrepancies between 10 and 50 s can likely be attributed to small inaccuracies in the predicted temperature fields at early times, immediately after pouring. More importantly, during the remainder of the cooling period, the predicted contraction rate for the bar consistently exceeds the measured rate. This leads

to an over-prediction of about 0.5 mm in the axial length change at 12000 s, when the bar is near room temperature (see Figure 3.4(a)).

To better match the measured and predicted contraction curves, modifications to both α_{tot} and T_{th} were required. First, the total linear thermal expansion coefficient was adjusted as shown in Figure 3.4(d); the entire curve was shifted downward in order to decrease the rate of contraction in the simulation. Also, the magnitude of the step at 948 K (675 °C) (representing the decomposition of austenite to pearlite and α -ferrite) was slightly increased to predict additional expansion during the solid-state phase transformation. These adjustments resulted in the measured and predicted axial length change curves to be exactly parallel during the entire cooling period. To eliminate the remaining shift between the two curves, the temperature for the onset of thermal contractions was increased to $T_{th} = 1703$ K (1430 °C). This temperature corresponds to a solid fraction of $g_s = 0.98$, as opposed to $g_s = 1$ for the initial simulation. Using the adjusted α_{tot} and T_{th} , excellent agreement between the measured (black curves) and predicted (pink curves) axial length changes can be observed in Figure 3.4 at all times.

The procedure used to adjust the temperature for the onset of thermal contractions, T_{th} , is illustrated in more detail in Figure 3.5. The figure compares the measured axial length change during the first 250 s with predictions for three different T_{th} : 1683 K (1410 °C) ($g_s = 1$), 1703 K (1430 °C) ($g_s = 0.98$), and 1723 K (1450 °C) ($g_s = 0.94$). After the first 50 s, the curves are parallel to each other, but only the $g_s = 0.98$ curve matches the measurements. At such high solid fractions, only isolated pools of liquid remain within the coherent solid network; hence, it is realistic for thermal contraction to commence before complete solidification.

For all remaining simulations (unrestrained and strained), the thermal strains were

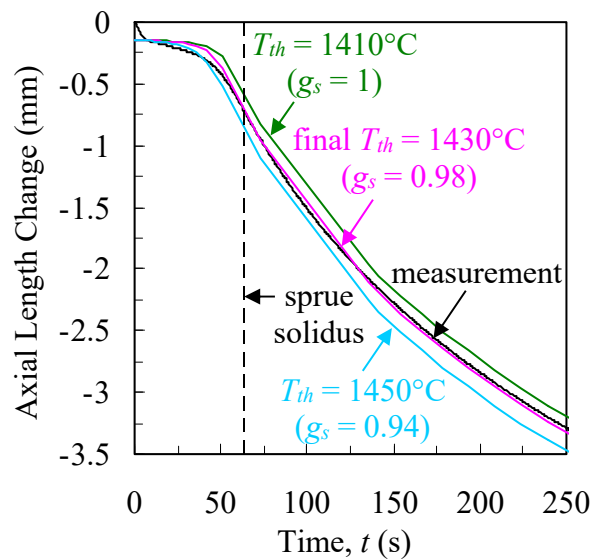


Figure 3.5 Parametric study showing the sensitivity of the predicted axial length change (from unrestrained bar 1) to changes in temperature at the onset of thermal contraction, T_{th} .

calculated using the adjusted α_{tot} in Figure 3.4(d). However, because the measured solidus temperature varied (from 1648 K (1375 °C) to 1688 K (1415 °C)) among the experiments (due to differences in the steel chemistries), a different T_{th} was used in each simulation. Using the same procedure as illustrated in Figure 3.5, the corresponding solid fractions for the onset of thermal contractions varied between 0.95 and 0.98. This variation can be attributed to uncertainties in determining the solidus temperature.

Strained Bar Simulation Results

An example of the accumulated viscoplastic strains predicted by the stress simulation (for strained bar 1) is shown in Figure 3.6. Due to the hotspot that is created by the sprue near the middle of the bar, the majority of the viscoplastic strain may be expected to occur at that location, since steel yields more easily at higher temperatures. However, the simulation results in Figure 3.6 indicate that the bar's axial distortions are distributed relatively evenly throughout its entire length. The spot of high strains predicted near each end of the bar is due to the cast steel contracting around the embedded restraining rod and nut. Figure 3.6 also indicates that the application of the additional force boundary condition at the base of the sprue results in the predicted axial length changes to be slightly larger on the left side of the sprue than on the right side. For the case shown in Figure 3.6, additional stress simulations were performed in which g_s^{coh} and g_s^{coal} were varied. Due to space limitations, the results are not shown here. It was found that, as expected, the present

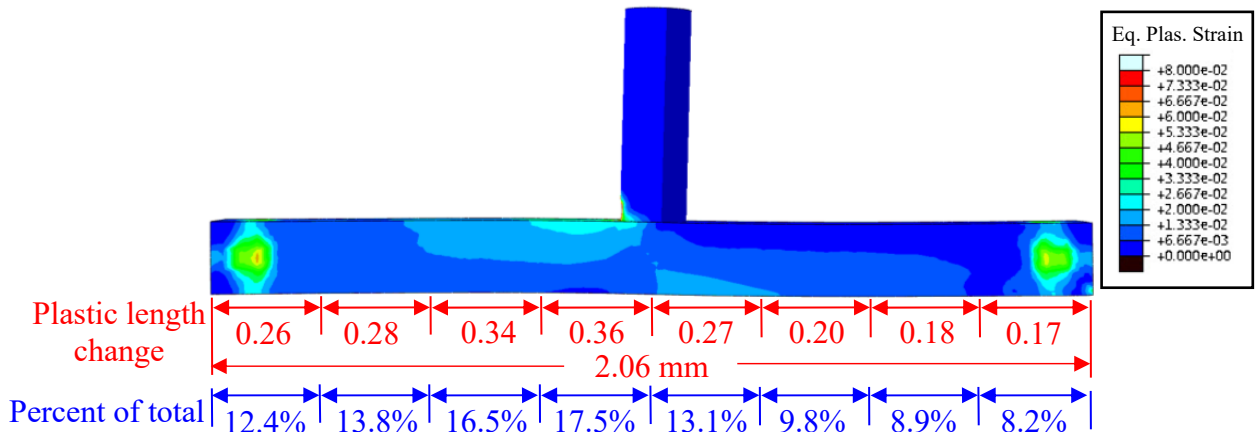
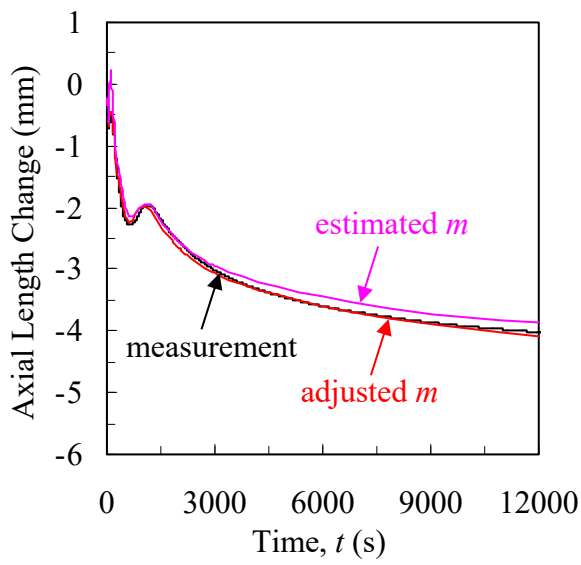


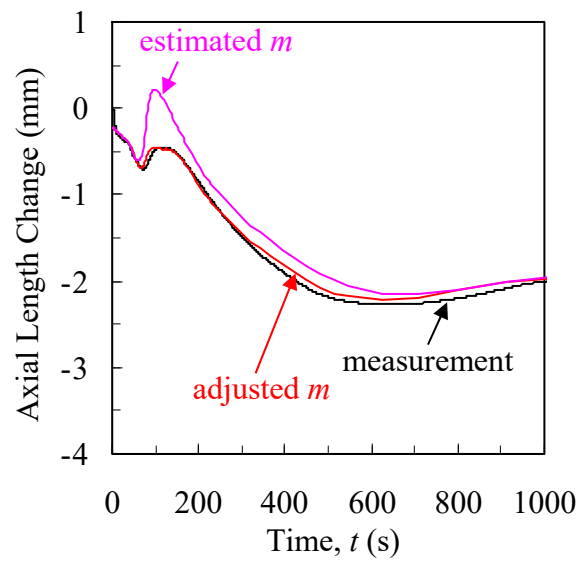
Figure 3.6 Total accumulated viscoplastic strains predicted for the strained bar 1 experiment.

predictions are insensitive to changes in both g_s^{coh} and g_s^{coal} .

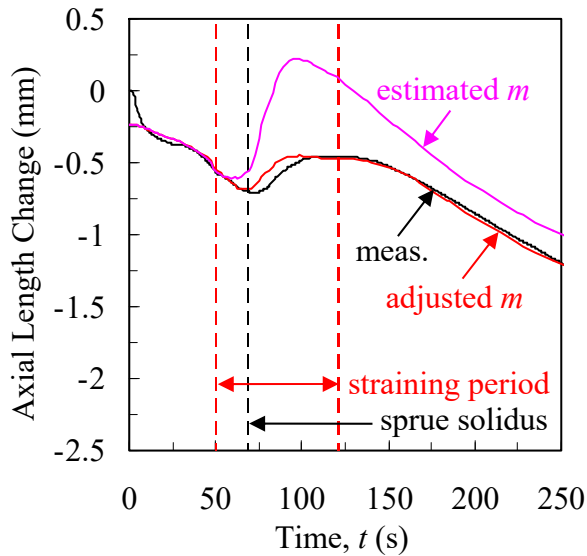
The measured and predicted axial length changes for the strained bar 1 experiment are compared in Figure 3.7. Initial predictions, labeled as “estimated m ” (pink lines), were obtained using the viscoplastic constitutive model parameters determined from tests with reheated specimens, as detailed in reference [19]. When viewed on the complete time scale (Figure 3.7(a)), the agreement of the initial predictions with the measurements appears to be good. However, Figure 3.7(c) shows that during the straining period an excessive



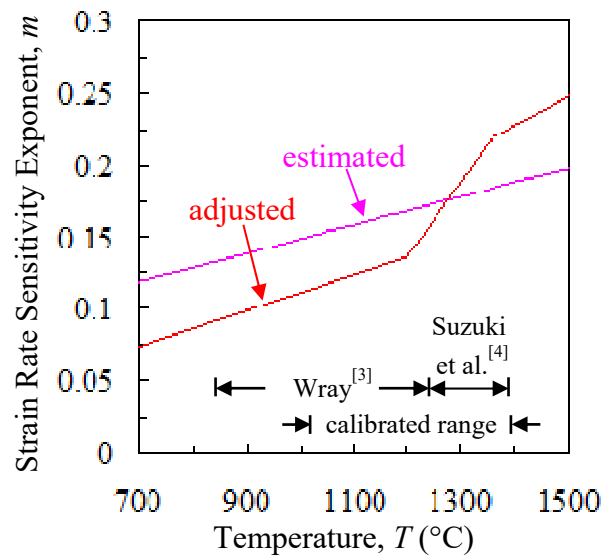
(a) Complete Time Scale



(b) Intermediate Time Scale



(c) Initial Time Scale



(d) Strain Rate Sensitivity Exponent

Figure 3.7 Measured and predicted axial length changes for the strained bar 1 experiment plotted on complete (a), intermediate (b), and initial (c) time scales. Predicted distortions were sensitive to changes in the strain rate sensitivity exponent (d) only within the calibrated range.

amount of viscoplastic strain is predicted. The predicted length increase due to the straining is about 0.8 mm, whereas the measured one is only 0.25 mm. In order to reduce this disagreement, a trial-and-error process was performed in which the strain rate sensitivity exponent, m , was adjusted until the measured and predicted length changes agreed at all times. The final adjusted m curve is shown in Figure 3.7(d) and compared to the initial

estimate. As can be seen from Figures 3.7(a) to 3.7(c), the adjustment produced excellent agreement between the measured and predicted axial length changes for this experiment, especially during the straining period.

The strain rate sensitivity exponent in Figure 3.7(d) was adjusted from 973 K (700 °C) to 1773 K (1500 °C). However, because distortions were induced mainly at higher temperatures (see Figure 2.5), the predicted distortions should be insensitive to variations in m at lower temperatures. Through a parametric study, the predicted distortions were found to be sensitive to changes in m for strained bar 1 from 1298 K (1025 °C) $\leq T \leq$ 1673 K (1400 °C). This range, termed the “calibrated range”, contains the temperatures for which the computational model has been calibrated from the experimental measurements and is included in Figure 3.7(d). Similar ranges were determined for all other strained bar experiments.

The adjusted m curve in Figure 3.7(d) is characterized by two segments and a transition region. The first segment (973 K (700 °C) $\leq T \leq$ 1473 K (1200 °C)) was shifted downward from the estimated curve, while the second segment (1633 K (1360 °C) $\leq T \leq$ 1773 K (1500 °C)) was shifted upward. The transition region (1473 K (1200 °C) $< T <$ 1633 K (1360 °C)) connects the two segments to form a piecewise continuous linear curve. Although the discontinuities between subdomains (located at 1473 K (1200 °C) and 1633 K (1360 °C)) are likely unphysical (i.e., a smooth continuous curve should be expected), additional experimental data would be needed to fine-tune the curves and eliminate the kinks. Interestingly, the temperature span of the first segment corresponds to that of the Wray^[4] measurements (1123 K (850 °C) $\leq T \leq$ 1523 K (1250 °C)), while the second segment roughly coincides with the Suzuki et al.^[5] temperature range (1523 K (1250 °C) $\leq T \leq$ 1673 K (1400 °C)). These similarities suggest that parameter estimation from the Wray^[4] measurements leads to an over-prediction of casting stresses, whereas using the Suzuki et al.^[5] measurements leads to an under-prediction. To show this apparent correlation, the temperature ranges for the Wray^[4] and Suzuki et al.^[5] measurements are included in Figure 3.7(d) and all subsequent m curve plots.

Choosing which parameter to adjust in the dynamic yield equation, Eq. [16], was determined through a process of elimination. The estimated strain hardening exponent, n , (Figure 2.7(a)) and initial yield stress, σ_0 , (Figure 2.7(b)) both decrease with increasing temperature. However, these parameters would need to be increasing functions of temperature above 1633 K (1360 °C) to achieve agreement between the measured and predicted length changes. Such changes would imply that the strength and hardening increase with temperature, both of which are unexpected. Therefore, σ_0 , n , and the reference strain, ϵ_0 , (which is calculated from σ_0 and n) were not modified. Another possibility was to modify the reference strain rate, $\dot{\epsilon}_0$, through adjustments to either the Arrhenius prefactor, A , or the activation energy, Q . However, because A only depends on carbon content (which did not vary significantly among the experiments), only small variations in this parameter would be expected. Also, Q would have to be adjusted as an increasing function of temperature, which is unphysical. This leaves the strain rate sensitivity exponent, m . Strain rate impacts stresses and distortions in steels mainly at high temperatures. This implies that m should increase with temperature, which is indeed the case for both the estimated (Figure 2.7(a)) and adjusted (Figure 3.7(d)) strain rate sensitivity exponents. Therefore, m was chosen as the adjustable parameter.

Another example of matching measured and predicted length changes is shown for the strained bar 5 experiment in Figure 3.8. Here, the length change during the straining period is vastly under-predicted when using the initial estimated m variation from the reheated specimens. This results in the predicted final length of the bar near room temperature to be about 1.5 mm shorter than what was measured. Adjusting the strain rate sensitivity exponent m in the simulation as shown in Figure 3.8(d), however, results in

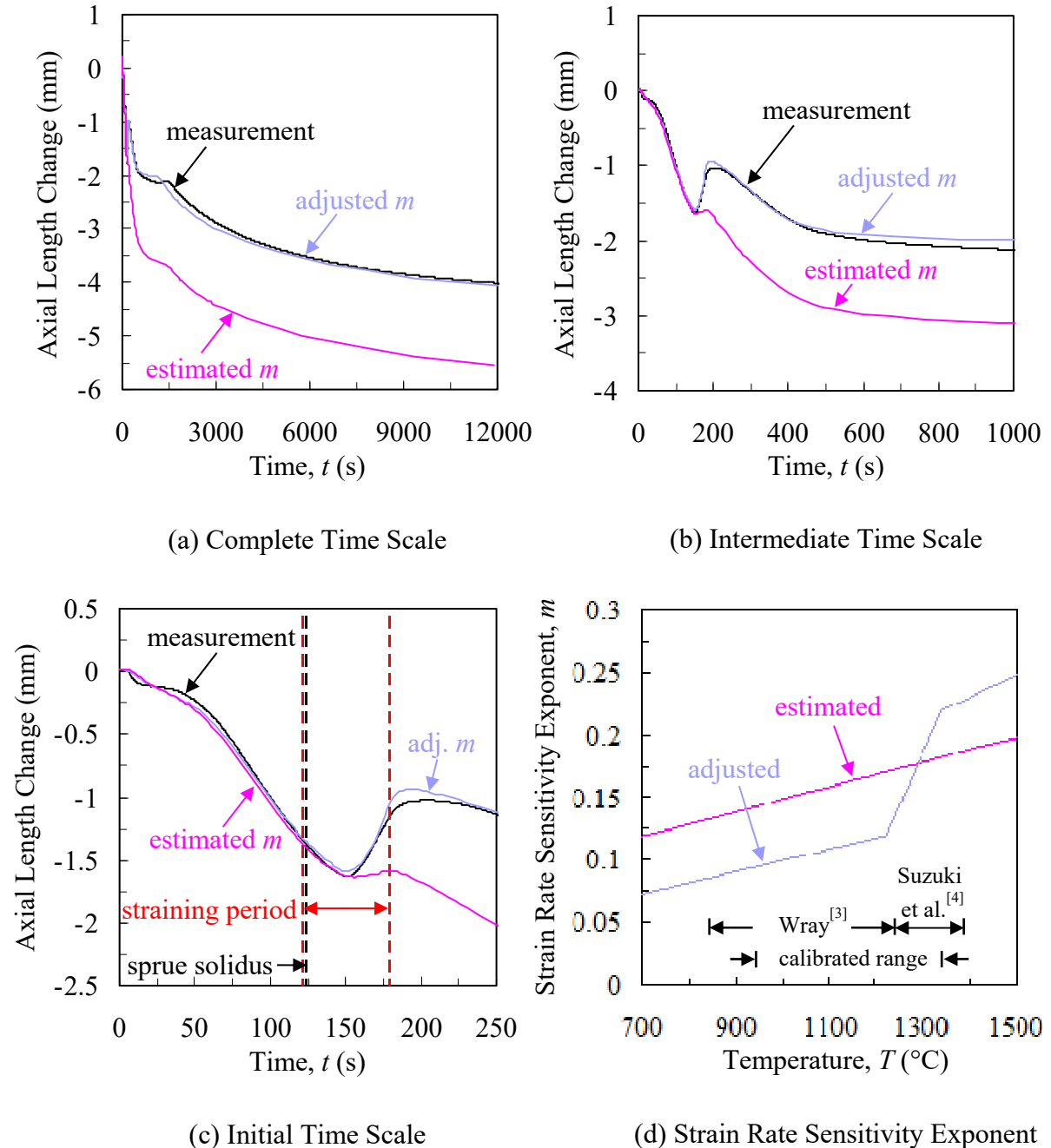


Figure 3.8 Measured and predicted axial length changes for the strained bar 5 experiment plotted on complete (a), intermediate (b), and initial (c) time scales. Predicted distortions were sensitive to changes in the strain rate sensitivity exponent (d) only within the calibrated range.

excellent agreement in the length changes at all times during the experiment. Note that the adjustments made to m in Figure 3.8(d) are similar in nature to the ones for the strained bar 1 experiment in Figure 3.7(d). This similarity is unexpected, because the straining in the two experiments (strained bar 1 and 5) was performed quite differently. By comparing the measured axial length changes in Figures 3.7(c) and 3.8(c), it can be seen that bar 1 was strained when it had contracted (freely) by about 0.5 mm, whereas bar 5 was strained much later when it had contracted already by 1.3 mm. Hence, strained bar 1 experienced the majority of the viscoplastic strains at higher temperatures than strained bar 5. As expected, the calibrated range for strained bar 5 ($1223 \text{ K } (950 \text{ }^{\circ}\text{C}) \leq T \leq 1623 \text{ K } (1350 \text{ }^{\circ}\text{C})$) was lower than that for strained bar 1 ($1298 \text{ K } (1025 \text{ }^{\circ}\text{C}) \leq T \leq 1673 \text{ K } (1400 \text{ }^{\circ}\text{C})$). In order to achieve agreement in the measured and predicted length changes for both experiments, the strain rate sensitivity exponent m had to be increased at higher temperatures (above $1573 \text{ K } (1300 \text{ }^{\circ}\text{C})$) and decreased at lower temperatures (below $1473 \text{ K } (1200 \text{ }^{\circ}\text{C})$). Simply shifting the m curve up or down does not produce good agreement for both experiments.

To further demonstrate the necessity for the adjustments to the strain rate sensitivity exponent, a parametric study was performed for the strained bar 2 experiment, as shown in Figure 3.9. In this figure, predicted results are shown for the initial simulation (using the initially estimated m curve) and for the final simulation using an adjusted m curve. Again, the initial m curve produces poor agreement and the adjusted m curve achieves excellent agreement between the measured and predicted axial length changes for this experiment. Furthermore, the adjustments made to m (Figure 3.9(d)) are similar in nature to the ones for the strained bar 1 and 5 experiments (see above). The calibrated range for strained bar 2 spans from $1273 \text{ K } (1000 \text{ }^{\circ}\text{C})$ to $1648 \text{ K } (1375 \text{ }^{\circ}\text{C})$, which falls between the bar 1 and 5 ranges. Figure 3.9 also shows simulation results for two additional simulations (termed “iteration 1” and “iteration 2”) where different m curves were tried. For the first iteration, the strain rate sensitivity exponent was only adjusted at high temperatures (i.e., the Suzuki et al.^[4] range) and the initially estimated values were used at lower temperatures (i.e., the Wray^[3] range), as shown in Figure 3.9(d). In this iteration, Figure 3.9(c) indicates that insufficient distortions are predicted during the straining period. For the second iteration, the strain rate sensitivity exponent was matched to the final adjusted curve at lower temperatures, but the initially estimated m curve was used in the high-temperature range. As a result, excessive distortions are predicted during the straining period. This clearly demonstrates that adjustments to the strain rate sensitivity exponent at both low and high temperatures (i.e., both the Wray^[4] and Suzuki et al.^[4] temperature ranges) are needed in order to match predicted and measured axial length changes. Based on these adjustments, the measurements of both Wray^[3] and Suzuki et al.^[4] appear to be inadequate for determining the mechanical behavior of steel during casting.

Figure 3.10(a) shows that excellent agreement was achieved between measured and predicted axial length changes for all five strained bar experiments. This figure is limited to the first 250 s, because afterwards the strains are predominately thermal and the axial length change curves are almost parallel. The axial length changes are different in each experiment because of variations in the straining period (beginning and duration), the sprue diameter (for strained bar 5), and the steel composition. Hence, each of the 5 experiments provides independent data with which the strain rate sensitivity exponent could be calibrated. The final adjusted strain rate sensitivity exponent curves are compared for all experiments in Figure 3.10(b). They all show the same behavior, and a single

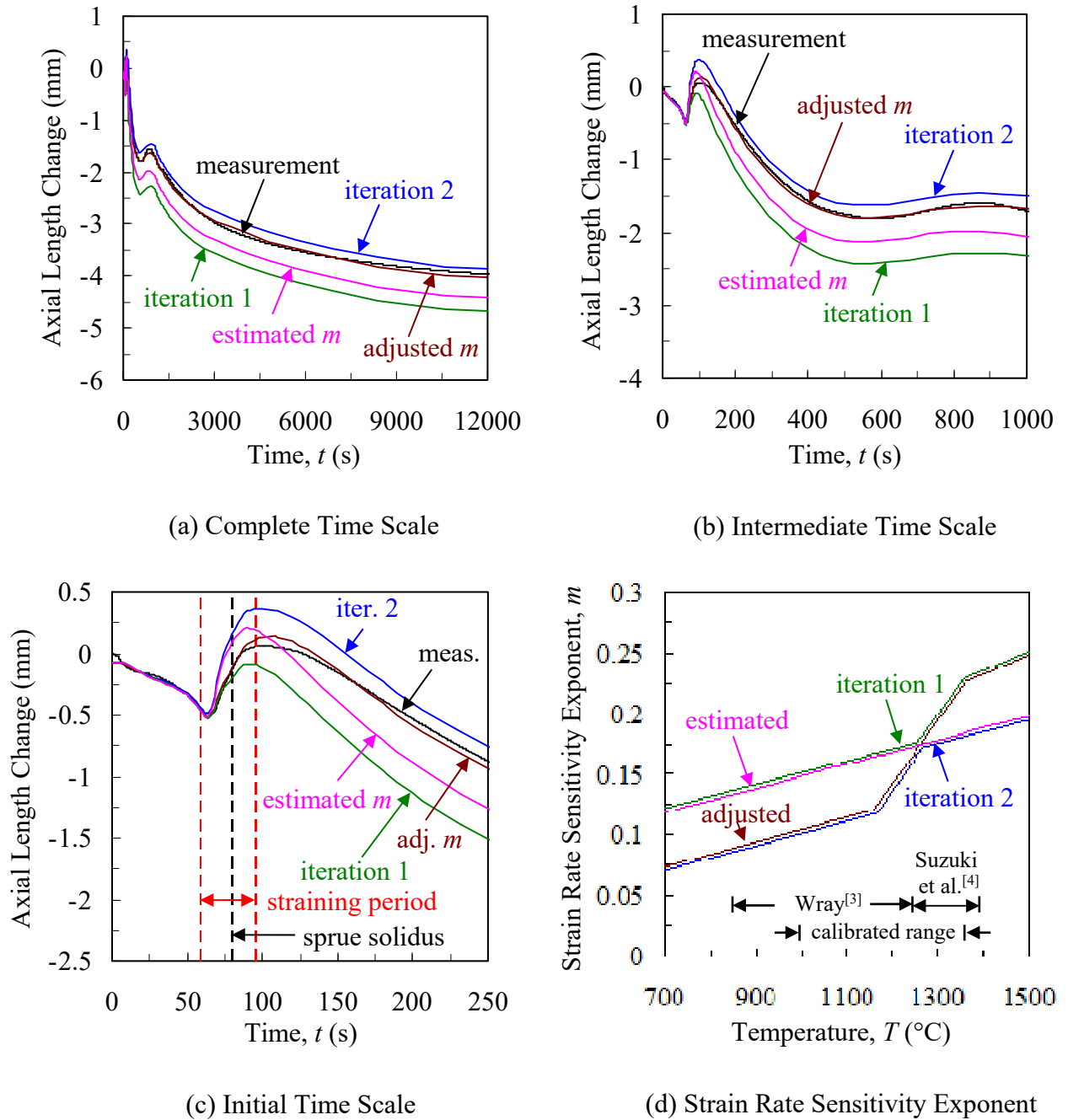


Figure 3.9 Predicted axial length change for the strained bar 2 experiment plotted on complete (a), intermediate (b), and initial (c) time scales. Predicted distortions were sensitive to changes in the strain rate sensitivity exponent (d) only within the calibrated range. Two additional stress simulations (iterations 1 and 2) demonstrated the need to adjust m in both the Wray^[3] and Suzuki et al.^[4] temperature ranges.

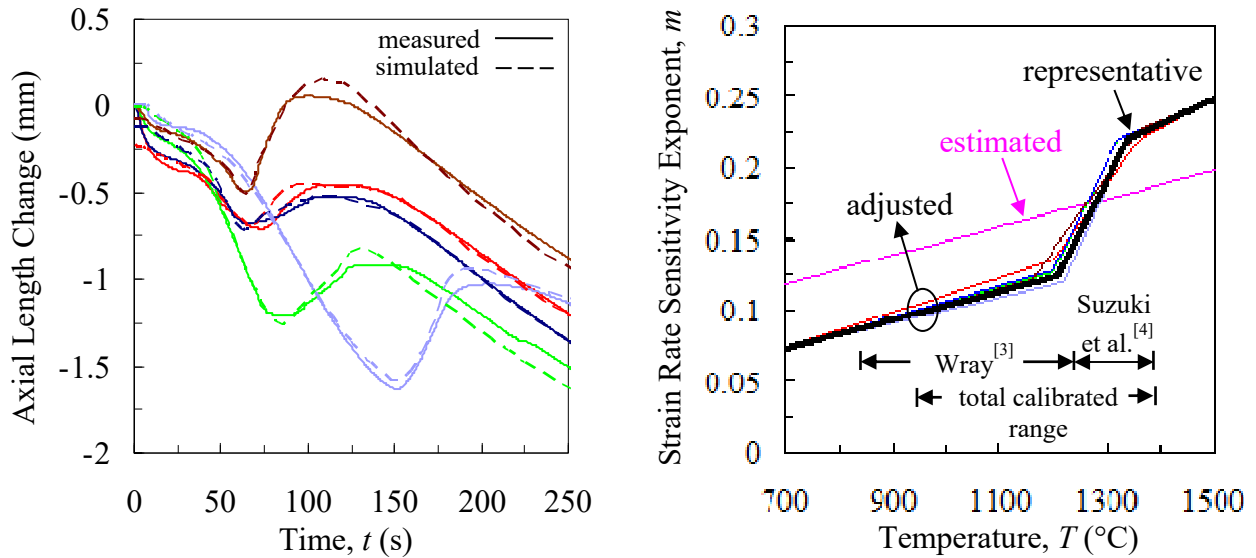
“representative” m curve can be constructed (thick black line in Figure 3.10(b)) that produces good agreement between measured and predicted axial length changes in all experiments. The piecewise expression for this curve is provided in Table 3.1. In addition,

the total calibrated range in Figure 3.10(b) combines the calibration ranges from all strained bar experiments and represents the temperatures for which the computational model has been calibrated for the present study.

Table 3.1 Expression for representative strain rate sensitivity exponent from Figure 3.10(b).

Strain Rate Sensitivity Exponent	Temperature, T (°C)
$6.373 \times 10^{-3} + 9.804 \times 10^{-5} T$	$700 \leq T \leq 1210$
$-7.592 \times 10^{-1} + 7.308 \times 10^{-4} T$	$1210 < T \leq 1360$
$-3.125 \times 10^{-2} + 1.875 \times 10^{-4} T$	$T > 1360$

The difference between the estimated and adjusted strain rate sensitivity exponent curves in Figure 3.10(b) represents the major finding for this study. The adjusted m curve, together with the other parameters in Figure 2.7, comprise the set of viscoplastic parameters needed to model the mechanical behavior of austenite during casting. To illustrate the differences between constitutive datasets using the estimated and adjusted m , representative stress-strain curves (at 1273 K (1000 °C), 1473 K (1200 °C), and 1673 K (1400 °C) for a 0.25%C steel and 1.5×10^{-5} 1/s strain rate) were generated and are shown in Figure 3.11. At 1273 K (1000 °C) and 1473 K (1200 °C), the predicted stresses using the estimated m are considerably higher (48% at 1273 K (1000 °C) and 28% at 1473 K (1200 °C)) than those using the adjusted m . At 1673 K (1400 °C), the opposite is true; the



(a) Axial Length Change

(b) Strain Rate Sensitivity Exponent

Figure 3.10 Measured and simulated axial length changes for all strained bar experiments shown in (a). The estimated, adjusted, and representative strain rate sensitivity exponents are summarized in (b). The total calibrated range ($1223 \text{ K (} 950 \text{ °C)} \leq T \leq 1673 \text{ K (} 1400 \text{ °C)}$) represents the temperature range over which the computational model has been calibrated for the present study.

predicted stresses are higher by 13% when using the adjusted m . These significant differences demonstrate that estimating mechanical constitutive parameters using reheated steel specimens may not be appropriate for stress simulations of casting processes. They also show the importance of calibrating the constitutive model using in-situ measurements.

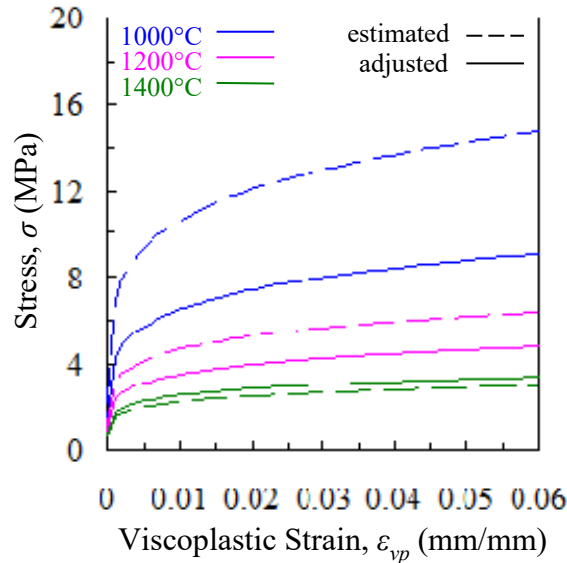


Figure 3.11 Comparison between predicted stresses for constitutive datasets using estimated and adjusted strain rate sensitivity exponents for a 0.25% carbon content and 1.0×10^{-5} 1/s strain rate.

3.2 Experimental and Simulation Results for Cylinder Castings

Experimental Results

The changes in the inner diameter measured by the LVDTs are plotted in Figures 3.12(a) and (b) on complete and 600 s time scales, respectively. The complete time scale (40000 s) represents the approximate time needed to cool the casting to room temperature. Shortly after the onset of filling ($t=0$), the inner diameters for the silica cores expanded to a maximum value (ranging from 1.15 mm to 1.3 mm) after 200 s. For the zircon core experiments, the inner diameters in experiments 1 and 2 expanded at approximately the same rate as the silica cores during the initial 25 s, whereas minimal expansion was measured in experiments 3 and 4 during this period. After 25 s, minimal additional expansion was measured for all zircon core experiments, as the curves are nearly horizontal until 250 s. In general, the zircon cores expanded far less than the silica cores, which can be attributed to differences in the thermal expansion coefficients. This is partly due to phase transformations in silica sand that generated considerably more thermal expansion than zircon. At approximately 250 s, the inner diameters for all experiments (silica and zircon) began to contract, as solidification neared completion and thermal contractions commenced in the steel. As a result, the inner diameters decreased until a local minimum at

approximately 4000 s and then increased until a local maximum at about 5000 s. This “wiggle” is a manifestation of the volumetric expansion in the casting that accompanies the solid state phase transformation from austenite to pearlite and α -ferrite. After 5000 s, the inner diameters decreased until room temperature. After 250 s, it is evident that all curves in Figure 3.13 contract (or expand during the phase transformation) at the same rate, i.e., all curves are parallel. In addition, the measured inner diameter contraction in the period $250 < t < 40,000$ s is equal to the patternmaker’s shrink for steel. These observations suggest that only thermal strains (i.e., no distortions) contributed to the LVDT measurements after 250 s. This is indeed the case and will be validated by the thermal strain predictions in a section given below. From this result, it can now be concluded that all distortions were generated by core expansion before solidification had completed. Core restraint did not create any distortions.

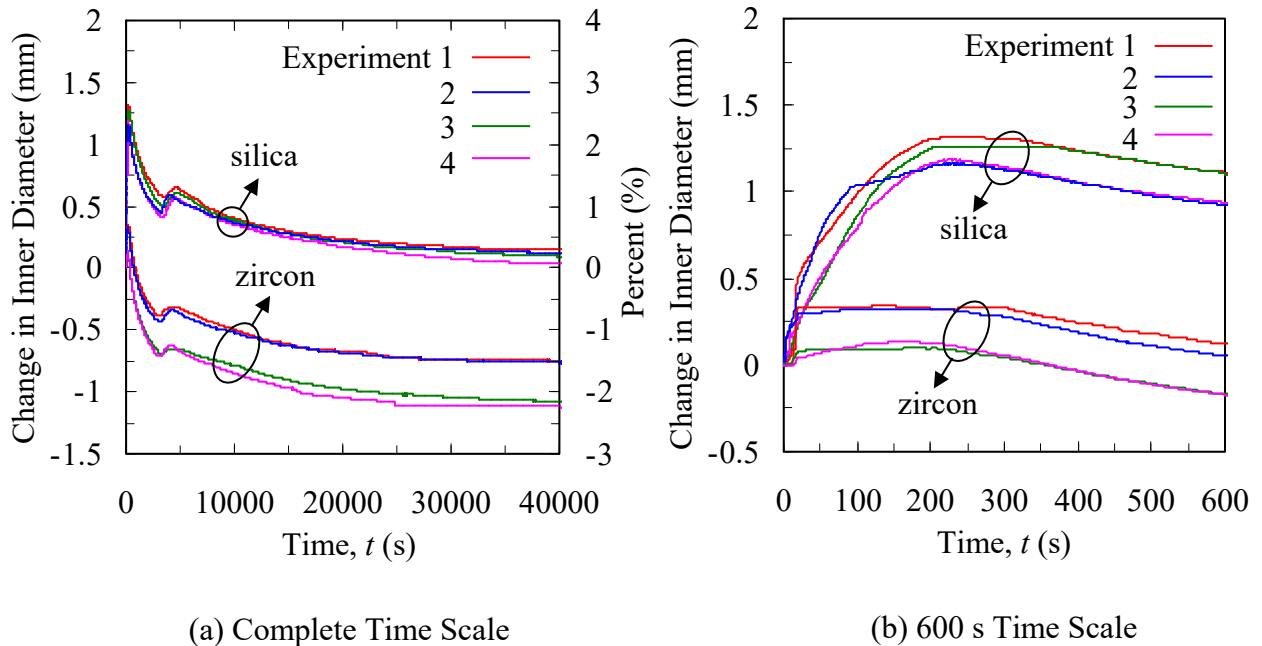
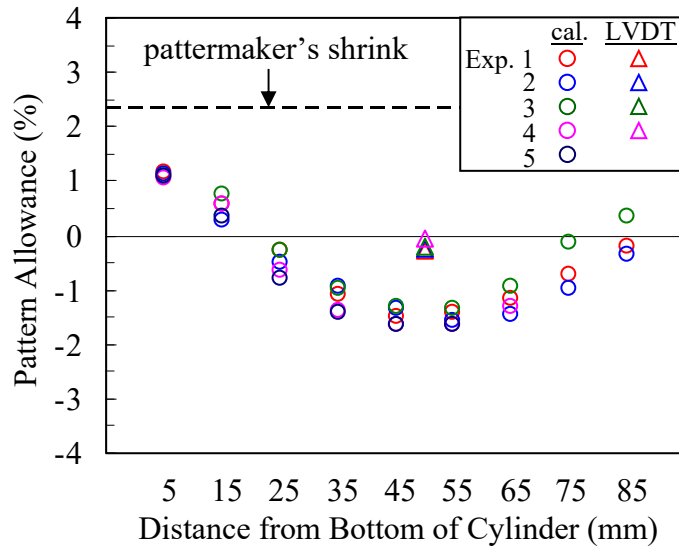


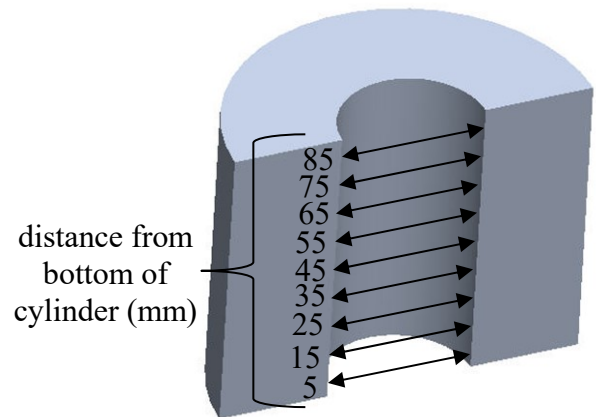
Figure 3.12 Measured change in the inner diameter at the cylinder’s mid-height for the silica and zircon core experiments plotted on complete (a) and 600 s (b) time scales.

In addition to the LVDT measurements, pattern allowances for the inner diameters were measured using Eq. [1.1] and are shown for the silica and zircon cores in Figures 3.13(a) and (b), respectively. The core (rather than pattern) dimensions were used to calculate pattern allowances. Measurements were taken with digital calipers at the feature locations shown in Figure 3.13(c). The pattern allowances are shown as circular symbols, with each color representing a different experiment. Any feature locations that contained large cracks or defects are not included in the figures. Each pattern allowance is the average of 16 measurements, taken circumferentially about the cylinder’s inner diameter. Scatter in the plots can be attributed to surface roughness of the casting and possibly slight differences in the core bulk densities. The average standard deviation for the measurements was approximately 0.15 mm (0.3% PA). The dashed horizontal lines in Figures 3.13(a) and (b) denote the patternmaker’s shrink of the steel ($\sim 2.3\%$ for a circular geometry) and serve as a reference; distortions are quantified as deviations from this line. In general, the silica

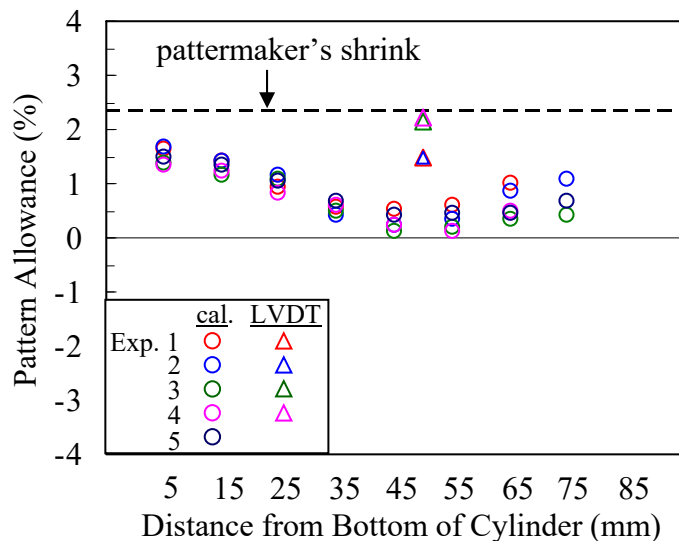
cores distorted more than the zircon cores, i.e., the silica core pattern allowances are smaller than those for the zircon cores. As in the LVDT measurements, these differences can again be attributed to differences in thermal expansion coefficients. The largest core expansions (for both silica and zircon cores) were observed at the mid-height of the cylinder, while smaller expansions occurred near the ends. As a result, the inner diameter of the cylinder evolved into a barrel-shaped profile (see Figure 3.13(d)), which can be



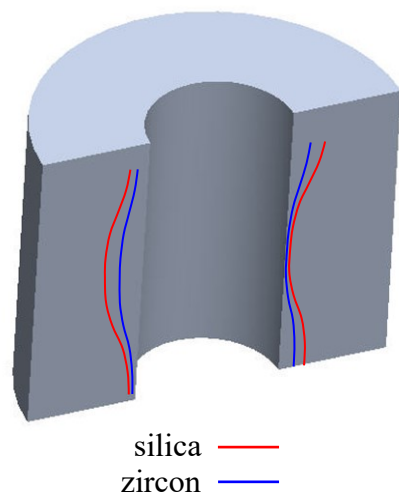
(a) Inner diameter pattern allowances for silica core experiments



(c) Feature locations



(b) Inner diameter pattern allowances for zircon core experiments



(d) Final inner diameter profile

Figure 3.13 Pattern allowances were measured for the silica (a) and zircon (b) core experiments at the feature locations shown in (c). The measurements revealed barrel-shaped inner diameter profiles (d).

explained by the local solidification times. At early casting times, the steel was mostly liquid and provided little restraint. As a result, the core easily expanded into the mold cavity. The solid fraction increased until eventually the steel reached coherency, which was accompanied by a dramatic increase in strength that prevented any further mold expansion. Since the inner diameter near the top and bottom of the cylinder solidified before the mid-height inner diameter, the largest expansion occurred at the mid-height.

Another observation from Figure 3.13 is that a large amount of scatter can be seen in the pattern allowances near the top of the cylinder. Recall that the mold was filled by pouring molten steel directly into the mold cavity (i.e., no gating system was used). In order to prevent spilling steel on the foundry floor, the mold cavity was never completely filled, which resulted in an air gap between the casting and cope. The thickness of this gap varied somewhat among the experiments, which affected cooling rates and the associated times to coherency.

Pattern allowances at the mid-height of the cylinder can also be calculated from the LVDT measurements by replacing the numerator in Eq. [1.1] with the negative change in the inner diameter at 40000 s (see Figure 3.12(a)). These values are shown as triangular symbols in Figures 3.13(a) and (b). Unfortunately, a discrepancy can be seen between the LVDT and calipers pattern allowances, as the LVDT values are higher than those from the calipers. In other words, the calipers measured more core expansion than the LVDTs. The repeatability of the LVDT measurements after 250 s (see Figure 3.12) suggests they are correct (this will be validated by the thermal strain simulations in a section that follows). Therefore, the discrepancy must have occurred during the initial 250 s. Most likely, the quartz rods were not embedded in the mostly liquid steel at early times and “slipped”. As a result, some amount of core expansion was not measured by the LVDTs. To remedy this, the LVDT measurements in Figure 3.13 were shifted upwards so that the LVDT and calipers pattern allowances coincided. The adjusted curves are shown in Figure 3.14. Note

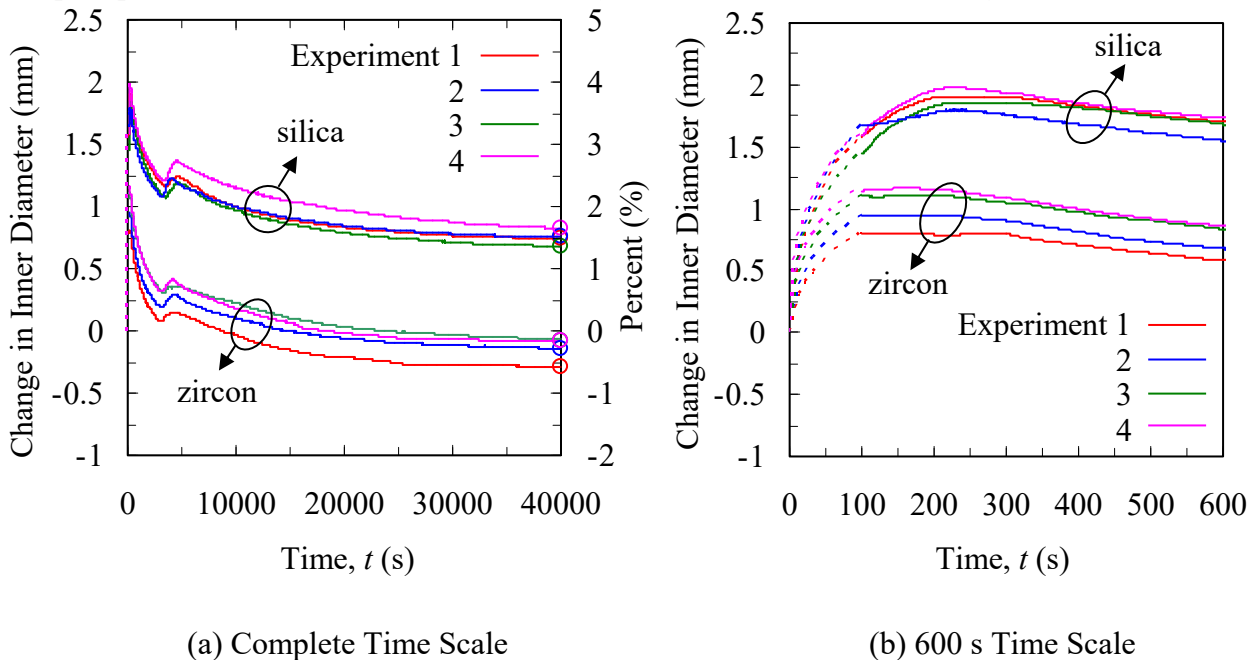


Figure 3.14 Adjusted LVDT measurements. The LVDT curves in Figure 2 were modified to match the pattern allowance measurements, which are represented by the circular symbols on the secondary axis in (a).

that the circular symbols on the secondary vertical axis in Figure 3.14(a) represent the calipers measurements. Then, the LVDT curves were modified during the initial 100 s to smoothly increase from zero to the shifted measurements. These modifications are shown as dashed lines in Figure 3.14(a). The resulting curves will be used below to validate the stress model predictions.

Cylinder Casting Thermal Simulation Results

Using the estimated properties, the predicted temperatures did not agree with the thermocouple measurements. To match the predicted and measured temperatures, several properties were adjusted through a trial-and-error process. The main modifications were made to the thermal conductivity for the bonded sands and latent heat of fusion for the steel. After the adjustments, the predicted and measured temperatures for the silica and zircon core experiments were in excellent agreement at all times (see Figures 3.15(a) and (b)). Very little difference was observed between the measured temperatures from the zircon and silica core experiments. Therefore, a single set of transient temperature fields can be used to predict distortions for the zircon and silica core experiments. Predicted solid fraction contours (shown at 25 s, 50 s, 100 s, and 200 s) in Figure 3.15(c) demonstrate the uneven solidification in the cylinder that led to the barrel-shaped profile of the inner diameter.

The predicted temperature fields were saved at a sufficient number of time steps (approximately 100) to ensure a smooth temperature profile at all nodes. The results were then mapped onto the finite element mesh used in the stress analysis (see below).

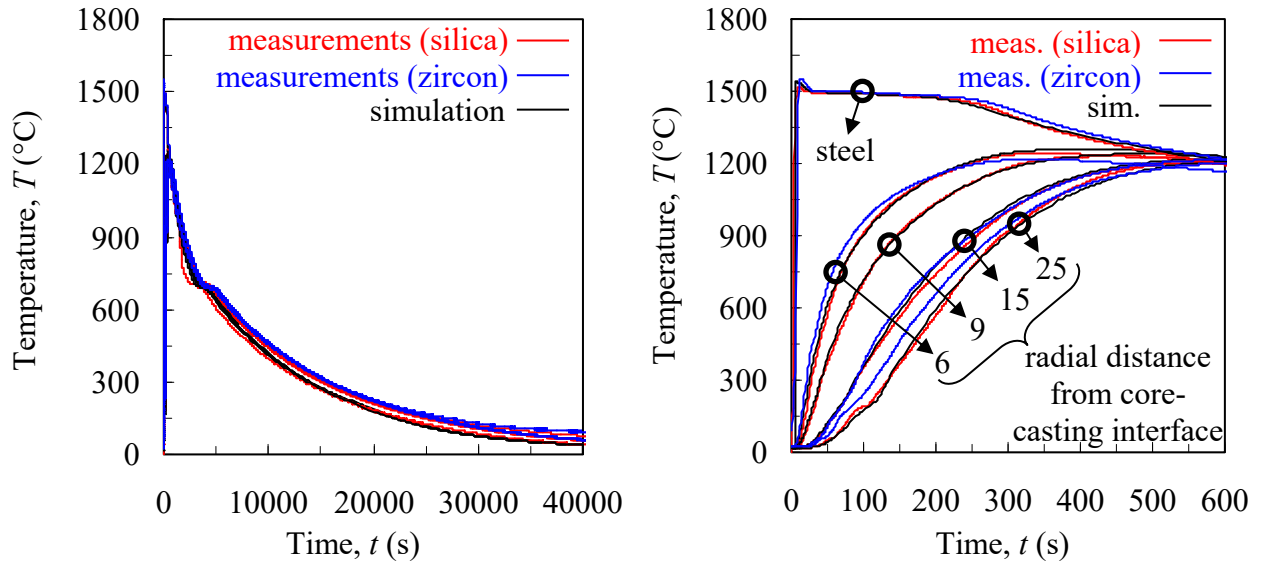
Cylinder Casting Thermal Strain Predictions

Preliminary finite element simulations were used to predict the evolution of thermal strains in both the casting and core. The importance of these simulations is twofold. First, the predicted thermal strains in the casting can be subtracted from the LVDT measurements to reveal the evolution of casting distortions. Second, the predicted thermal strains in the core will verify whether thermal expansion of the bonded sand can account for the cylinder's inner diameter expansion during solidification. If not, another mechanism must be considered. Two simulations were performed, in which the casting and core were simulated separately. Minimal boundary conditions were enforced to prevent rigid body translations and rotations.

The predicted change in inner diameter for the steel cylinder due to thermal strains is compared with the silica and zircon LVDT measurements on complete and 600 s time scales in Figures 3.16(a) and (b), respectively. The temperature dependent linear thermal expansion coefficient of the steel (shown in Figure 3.16(c)) was calibrated by Galles and Beckermann^[19] and the steel was set to begin thermally contracting at $g_s = 0.97$.^[19] During the initial 250 s, the thermal strain simulation curve is horizontal, as no changes in the inner diameter were predicted. Beginning at 250 s, thermal contractions commenced in the steel and reduced the inner diameter, which can be seen as a decrease in the thermal strain simulation curve. From $t = 250$ s until the onset of the solid state phase transformation (at approximately 4000 s), the thermal strain simulation curve decreases at the same rate as the silica and zircon LVDT measurements. The kink in the linear thermal expansion curve at

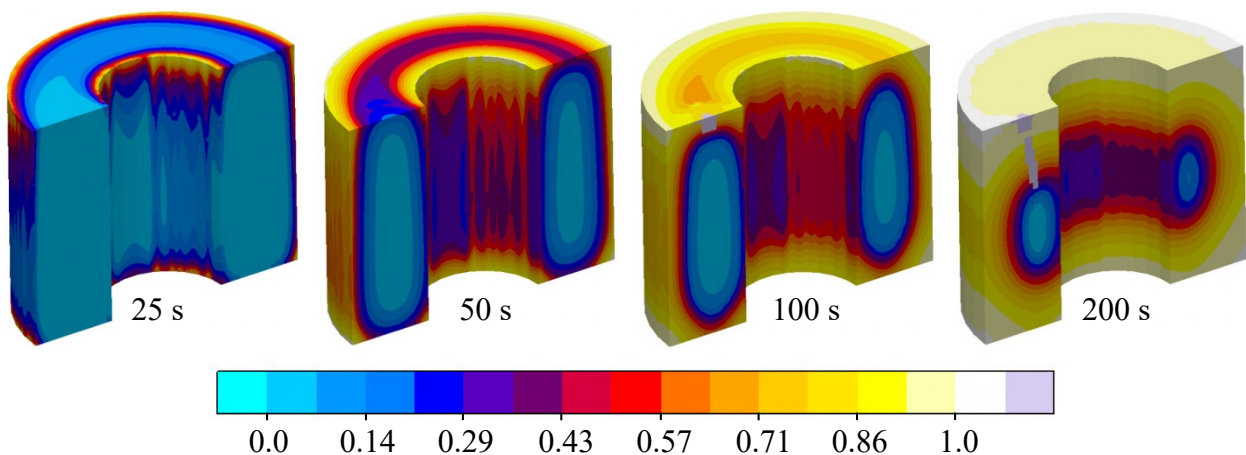
approximately 700°C (see Figure 3.16(c)) is included to predict the volumetric expansion associated with the phase transformation. After the transformation, the thermal strain prediction curve decreases at the same rate as the LVDT measurements. It is obvious that the measured and simulated curves are parallel after 250 s. This verifies the previous assertion that all changes in the inner diameters after 250 s were created by thermal strains in the solidified steel. Hence, to reiterate, all casting distortions in this study were created by core expansion during solidification. Core restraint after solidification did not generate distortions.

The predicted thermally induced change in the diameter for the silica and zircon cores at mid-height are compared to the LVDT measurements on complete and 600 s time scales in Figures 3.17(a) and (b), respectively. Thermal strains in the cores were calculated



(a) Complete time scale

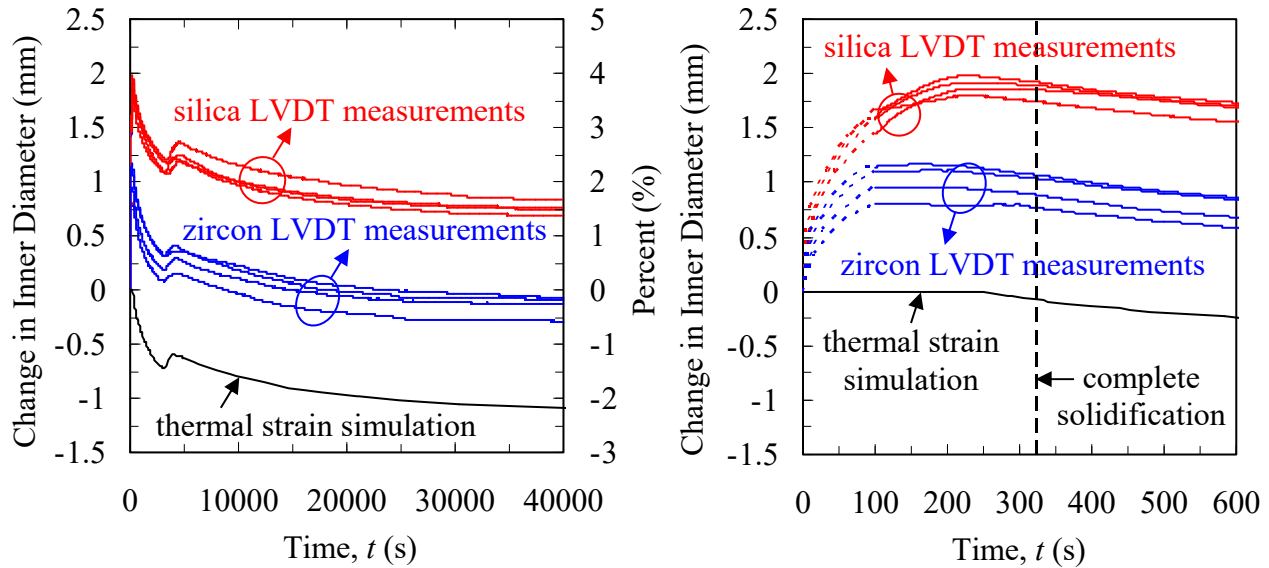
(b) 600 s time scale



(c) Fraction Solid

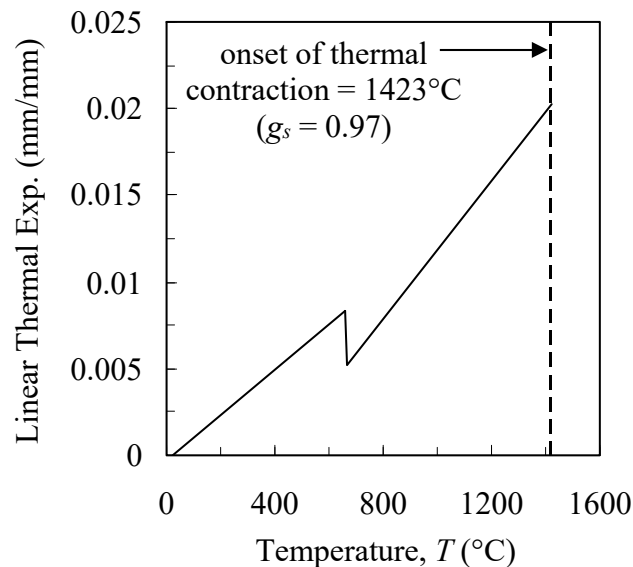
Figure 3.15 Comparison between measured and predicted temperatures for the silica and zircon core experiments on complete (a) and 600 s (b) time scales. The thermocouple at the 9 mm location for the zircon core experiment failed. Solid Fraction contours (c) illustrate uneven solidification.

using the temperature dependent linear thermal expansion coefficient in Figure 3.17(c), which was measured in separate experiments using a dilatometer. The curves in Figure 3.17(c) illustrate the vast difference in thermal expansions between the different sands. In particular, phase changes in silica sand at 560°C and 1470°C generate considerable expansion, whereas no such events occur in zircon sand. In general, the predicted core



(a) Complete Time Scale

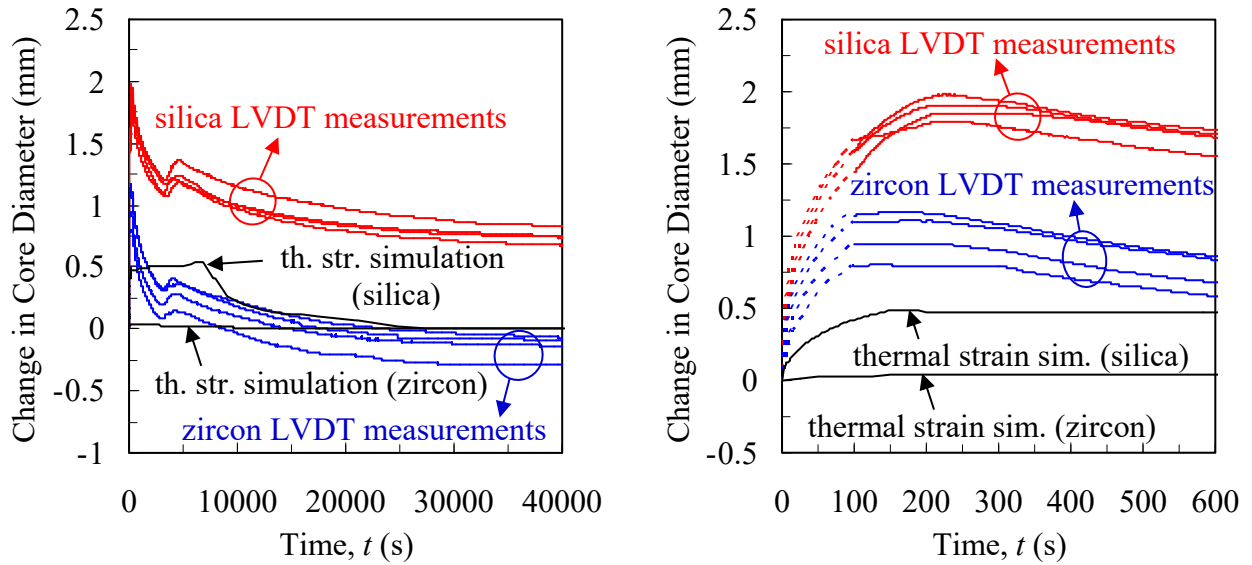
(b) 600 s Time Scale



(c) Linear Thermal Expansion of Steel

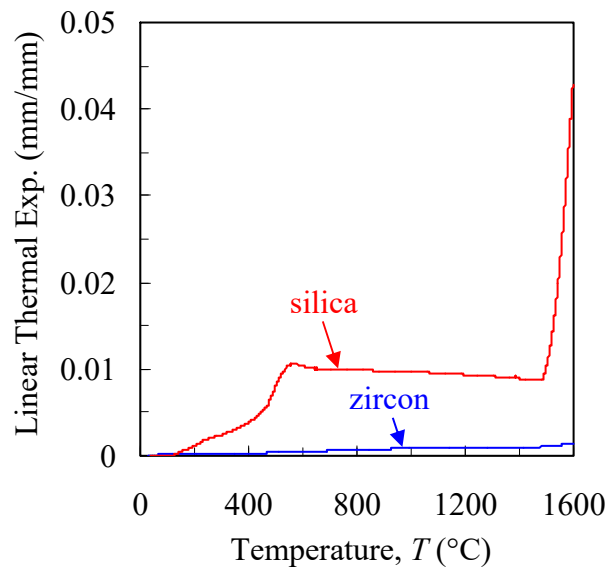
Figure 3.16 Comparison between the LVDT measurements and predicted thermal strains in the cylinder on complete (a) and 600 s (b) time scales. Thermal strains were calculated using the linear thermal expansion coefficient in (c), which was calibrated by Galles and Beckermann.¹⁹

expansions greatly under-predicted both the silica and zircon LVDT measurements. For example, the simulation only predicted a 0.5 mm (roughly 25% of the measurement) increase in diameter for the silica core after 200 s. Similarly, the predicted expansion at 200 s for the zircon core (~ 0.1 mm) is far less than the measured inner diameter expansions, which ranged from 0.75 mm to 1.25 mm. After approximately 8000 s, the outer diameters



(a) Complete Time Scale

(b) 600 s Time Scale



(c) Measured Linear Thermal Expansion of Bonded Sands

Figure 3.17. Comparison between the LVDT measurements and predicted thermal strains in the silica and zircon bonded sands on complete (a) and 600 s (b) time scales. Thermal strains were predicted using the measured linear thermal expansions in (c).

for the silica and zircon cores begin to thermally contract until the predicted changes in core diameters were reduced to zero at room temperature (40,000 s). These contractions, however, have no influence on the pattern allowances in the cylinder, as distortions were only generated during the initial 200 s.

Such large discrepancies between the measurements and predictions during the initial 200 s suggest that another mechanism contributed to the cylinder's inner diameter expansion. Initially, it was postulated that the cristobalite phase transformation in silica sand (see the sharp increase at approximately 1470°C in Figure 3.17(c)) may have been affected by atmospheric conditions inside the core, which in turn caused the transformation to occur at a lower temperature. Unfortunately, this argument cannot be made for the zircon core experiments because zircon sand does not experience phase changes. However, at the time, the zircon core experiments had yet to be performed. Therefore, through a parametric study, it was found that the measured inner diameter expansion could be predicted by reducing the cristobalite transformation temperature to 1300°C. Based on this result, a new experiment was designed as depicted in Figure 3.18(a). A rectangular plate (300 mm length \times 38 mm thickness \times 150 mm depth) was cast in a silica sand mold. Bonded sand samples were packed in thin-walled quartz tubes (25 mm inner diameter and 1 mm wall thickness) that were inserted through pre-drilled holes in the bottom of the drag so that the top of the tubes were positioned flush with the bottom of the mold cavity. The mold was filled using a simple gating system that consisted of a pouring cup and sprue. After the casting cooled to room temperature, the quartz tubes were carefully extracted from the mold. The bonded sand was then removed in 1-mm thick layers (see Figure 3.18(b)) and tested using x-ray diffraction. Cristobalite is quasi-stable at room temperature, as kinetic barriers prevent its transformation back to quartz. From the samples, the closest 1 mm layer from the mold-metal interface was found to contain less than 5% of the cristobalite phase. Smaller amounts were found in subsequent layers, as shown in Figure 3.18(b). These small amounts of cristobalite could only account for about 0.01 mm of additional expansion in the experiment. Therefore, the unexplained core expansion in the silica core experiments could not be explained by cristobalite formation.

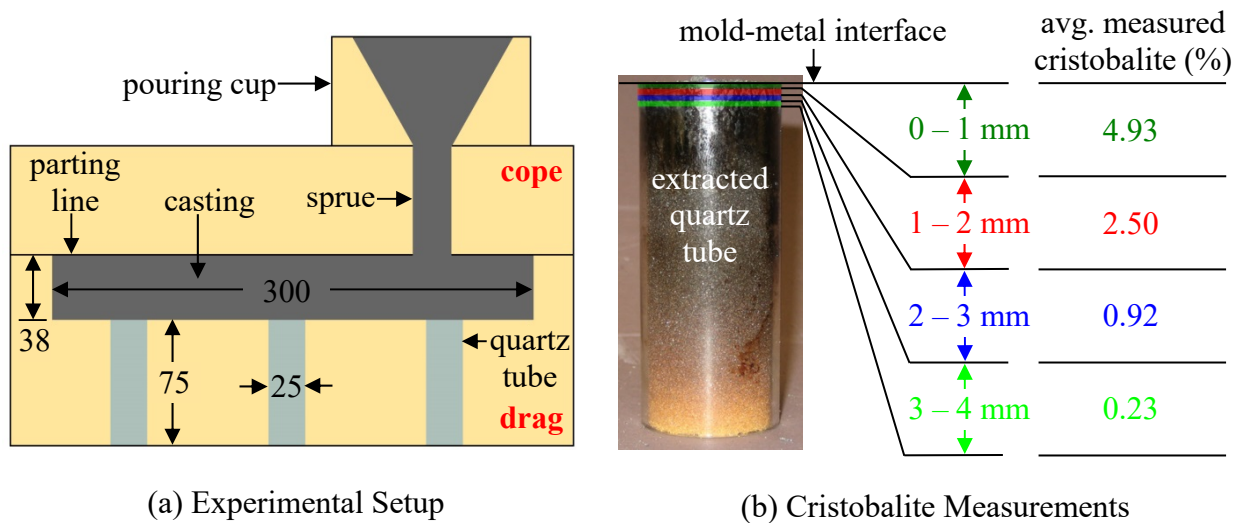


Figure 3.18. Experimental setup (a) used to measure the formation of cristobalite in bonded silica sand. Layers of sand were removed in 1 mm layers from the extracted quartz tube in (b) and tested using x-ray diffraction. All dimensions in mm.

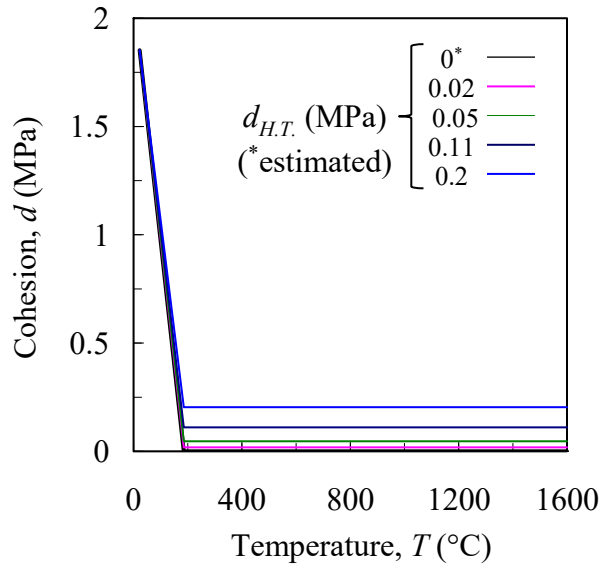
A plausible explanation is that sand dilation caused the unexplained core expansion. Dilation is illustrated in Figure 1.2; the initial state of dense sand contains small air voids between the grains (Figure 1.2(a)). After a shear force is applied, however, the irregularly-shaped sand grains translate and/or rotate and cause the voids to grow, resulting in volumetric expansion of the sand aggregate (Figure 1.2(b)). The rapid flow of heat from the casting heats the refractory core from the outside inward, generating large temperature gradients. This uneven heating is conducive to the formation of shear forces. Saada *et al.*^[18] suggested that dilatant behavior occurred for temperatures greater than 120°C. For this study, the Drucker-Prager Cap model features the ability to predict dilation.

Cylinder Casting Stress Simulations

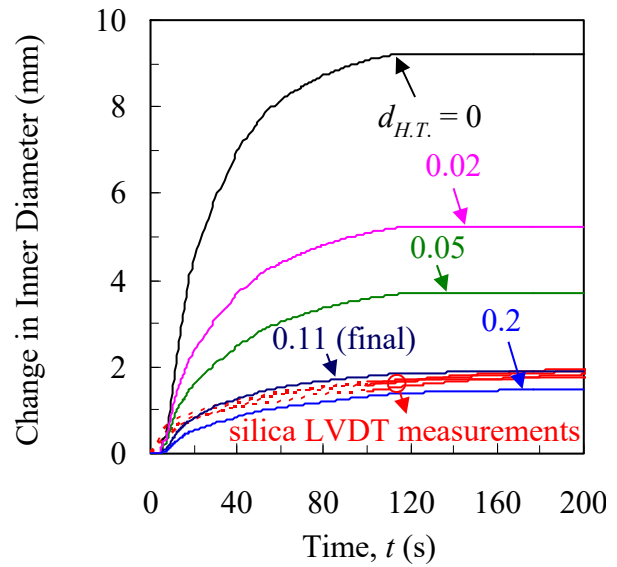
The stress simulations required several inputs. The estimated elastic properties (E and ν), Drucker-Prager Cap parameters (β , d , α , R), and hardening curves (see Figure 2.9(d)) for the bonded sands are described in Section 2.6. The initial hydrostatic compressive strengths ($p_{b0} = 2.4$ MPa and 2.3 MPa for the silica and zircon cores, respectively) were determined from the void ratio (e) vs. $\log p$ plots (see Figures 2.9(b) and (c)) using the initial bulk density of the bonded sands. The elasto-visco-plastic properties for the steel were taken from Galles and Beckermann.^[19] The thermal expansion coefficients for the steel and bonded sands are shown in Figures 3.16(c) and 3.17(c), respectively. Finally, the calculated temperature fields were inputted from MAGMASOFT®.

Using the inputs, the finite element stress analysis predicted stresses and strains in the casting, core, and drag. For the initial simulation, excessive dilation was predicted and the simulated change in inner diameter far exceeded the LVDT measurements. This is in stark contrast to the free core expansions that only predicted a small fraction of the LVDT measurements (see Figure 3.17). In order to match the measured and simulated core expansions, parametric studies were performed to determine which parameter to adjust. Only the high temperature properties were considered, as negligible distortions can be expected at the lower temperatures. In order to avoid an arbitrary matching procedure, it was decided to adjust a single parameter. Parametric studies revealed that the only modification that could match the predicted inner diameter evolution to the LVDT measurements was through the high temperature cohesion parameter, $d_{H.T.}$. Recall that the high temperature properties were estimated from dry, un-bonded sand, which has no cohesion. During casting, the room temperature cohesion ($d_{R.T.}$) of bonded sand thermally degraded with increasing temperatures. However, binder pyrolysis is a kinetic process and the bonded sands can be expected to yield before pyrolysis has completed. Therefore, some amount of cohesion should be expected during yielding. Through a parametric study, the measured and predicted inner diameter expansions for the silica experiments were matched for $d_{H.T.} = 0.11$ (see Figure 3.19(a)). Using the same procedure, $d_{H.T.}$ was adjusted from 0 to 0.08 to for the zircon experiments.

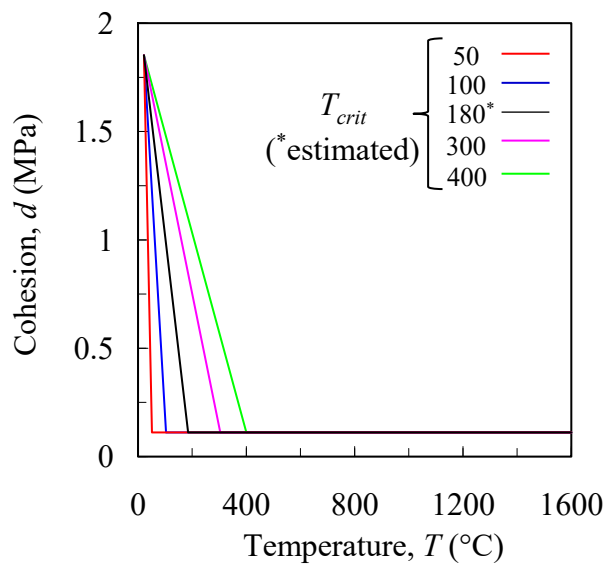
Until now, it has been suggested that minimal yielding occurred in the bonded sands at lower temperatures (i.e., before binder pyrolysis). To show this, a parametric study on the critical temperature (T_{crit}) for the cohesion parameter was performed. Recall that the critical temperature defines the transition from bonded to un-bonded sand due to



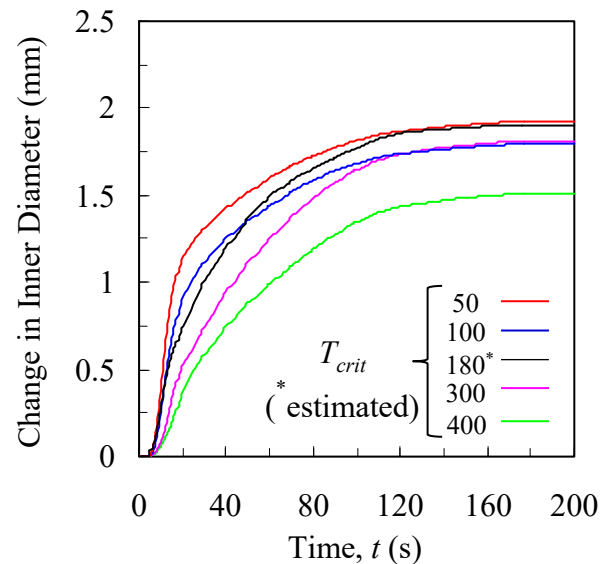
(a) Cohesion Parameter



(b) Effect of $d_{H.T.}$ on Silica Core Expansion



(c) Cohesion Parameter



(d) Effect of Critical Temperature on Silica Core Expansion

Figure 3.19 The high temperature cohesion parameter ($d_{H.T.}$), was adjusted as shown in (a) to match the simulated change in inner diameter to the LVDT measurements for the silica cores (b). A parametric study investigated the effect of changes in the critical temperature, T_{crit} , (c) on the predicted change in inner diameter (d).

binder pyrolysis. Any changes to the critical temperature will alter the low temperature properties. Figure 3.19(c) illustrates how variations in the critical temperature between

50°C and 400°C affect the cohesion parameter. The sensitivity of the predicted inner diameter evolution to these differences is shown in Figure 3.19(d). The variations in the predicted change in inner diameter are relatively small (< 0.3 mm) when the transition temperature is below 300°C. This result supports the intuition that the low temperature properties play a small role for the prediction of pattern allowances.

Using the adjusted cohesion values for the silica and zircon bonded sands, the inner diameter evolutions were predicted within the measurement scatter at all times, as shown in Figure 3.20. Recall that all changes in the inner diameter after solidification were caused by

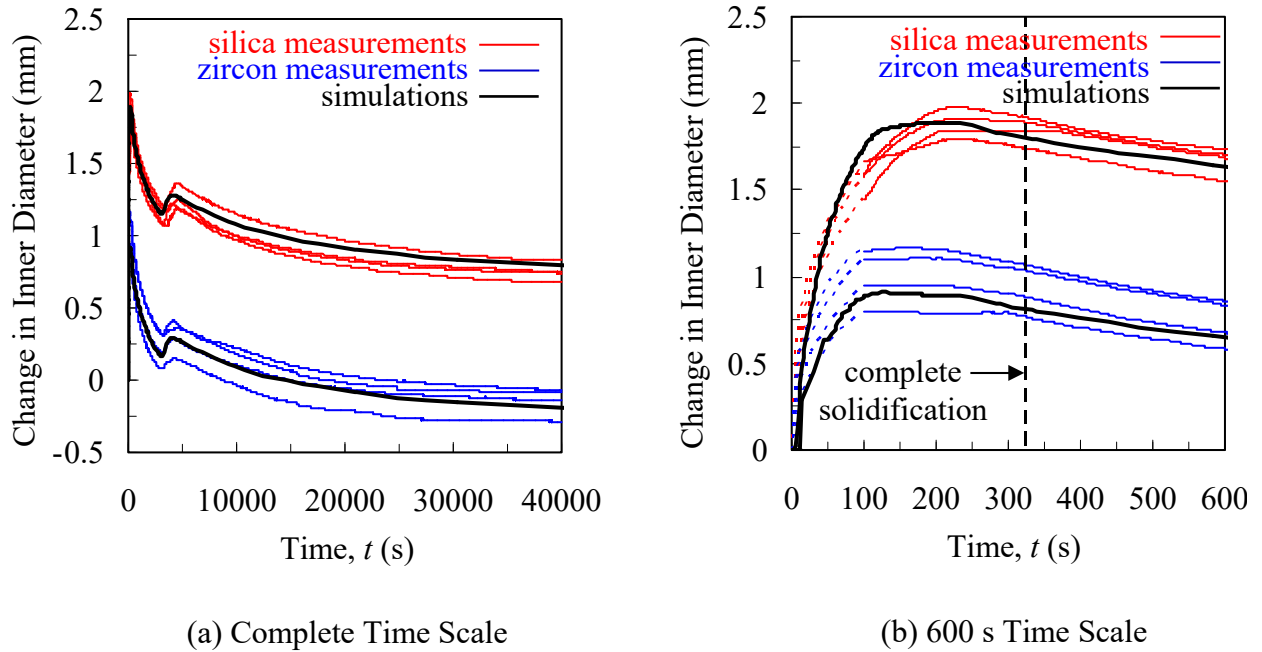


Figure 3.20 Comparison between measured and predicted changes in the inner diameter for the silica and zircon core experiments after adjusting the high temperature cohesion.

thermal strains (see Figure 3.16). Thus, the adjustment to the cohesion parameter only affected the predicted inner diameter evolution before solidification. In addition, the simulations predicted the pattern allowances accurately (see Figure 3.21). Only the zircon pattern allowances at the 5 mm location were not predicted within the scatter of the measurements. This disagreement can be attributed to uncertainties in the predicted temperatures shortly after filling. The final datasets used in the simulations are summarized in Tables 3.2 and 3.3 for the silica and zircon sands, respectively.

Table 3.2 Mechanical properties and Drucker-Prager Cap parameters for the silica bonded sands.

Temperature (°C)	E (MPa)	ν	β	d (MPa)	R	α
20	3403	0.3	55°	1.85	0.45	0.01
180	60	0.3	55°	0.11	0.45	0.01
1600	60	0.3	55°	0.11	0.45	0.01

Table 3.3 Mechanical properties and Drucker-Prager Cap parameters for the zircon bonded sands.

Temperature (°C)	E (MPa)	ν	β	d (MPa)	R	α
20	3403	0.3	52°	1.85	0.45	0.01
180	60	0.3	52°	0.08	0.45	0.01
1600	60	0.3	52°	0.08	0.45	0.01

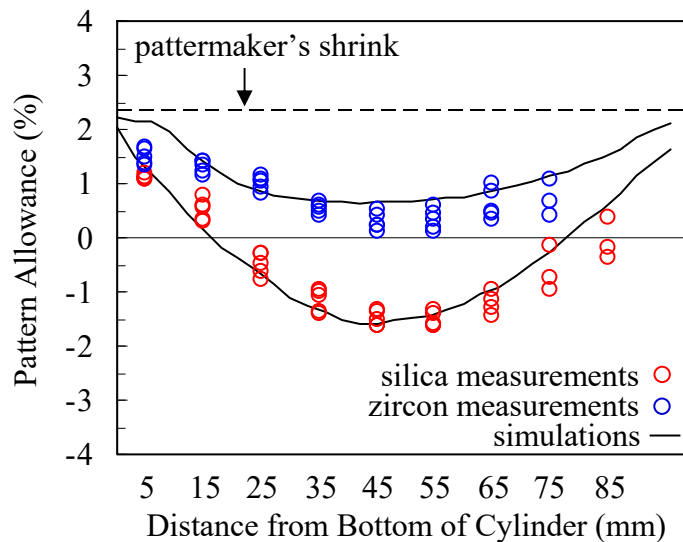


Figure 3.21 Comparison between measured and predicted pattern allowances for the silica and zircon core experiments after adjusting the high temperature cohesion.

Figure 3.22 shows contours of temperatures (a), von Mises stress (b), pressure (c), and equivalent plastic strains (d) at 50 s, 200 s, and 40,000 s (i.e., room temperature). The barrel-shaped profile can be seen after 50 s and is fully-evolved after 200 s. At 50 s, von Mises stresses, which are a necessary condition for the prediction of dilation, can be seen in excess of 0.25 MPa throughout the core. The combination of these shear stresses with low pressures give rise to significant equivalent plastic strains in the core after 50 s (see Figure 3.22(d)). A strong correlation between the equivalent plastic strain and temperature contours can also be seen at 50 s, as significant plastic strains are only predicted in the high temperature regions of the mold. This comparison illustrates the minimal yielding that was predicted in the bonded sands at low temperatures.

Parametric Studies

The lack of high temperature mechanical measurements raises questions concerning the accuracy of the bonded sand properties used in this study. Certainly, some amount of temperature dependence in the properties can be expected. However, the impact of this

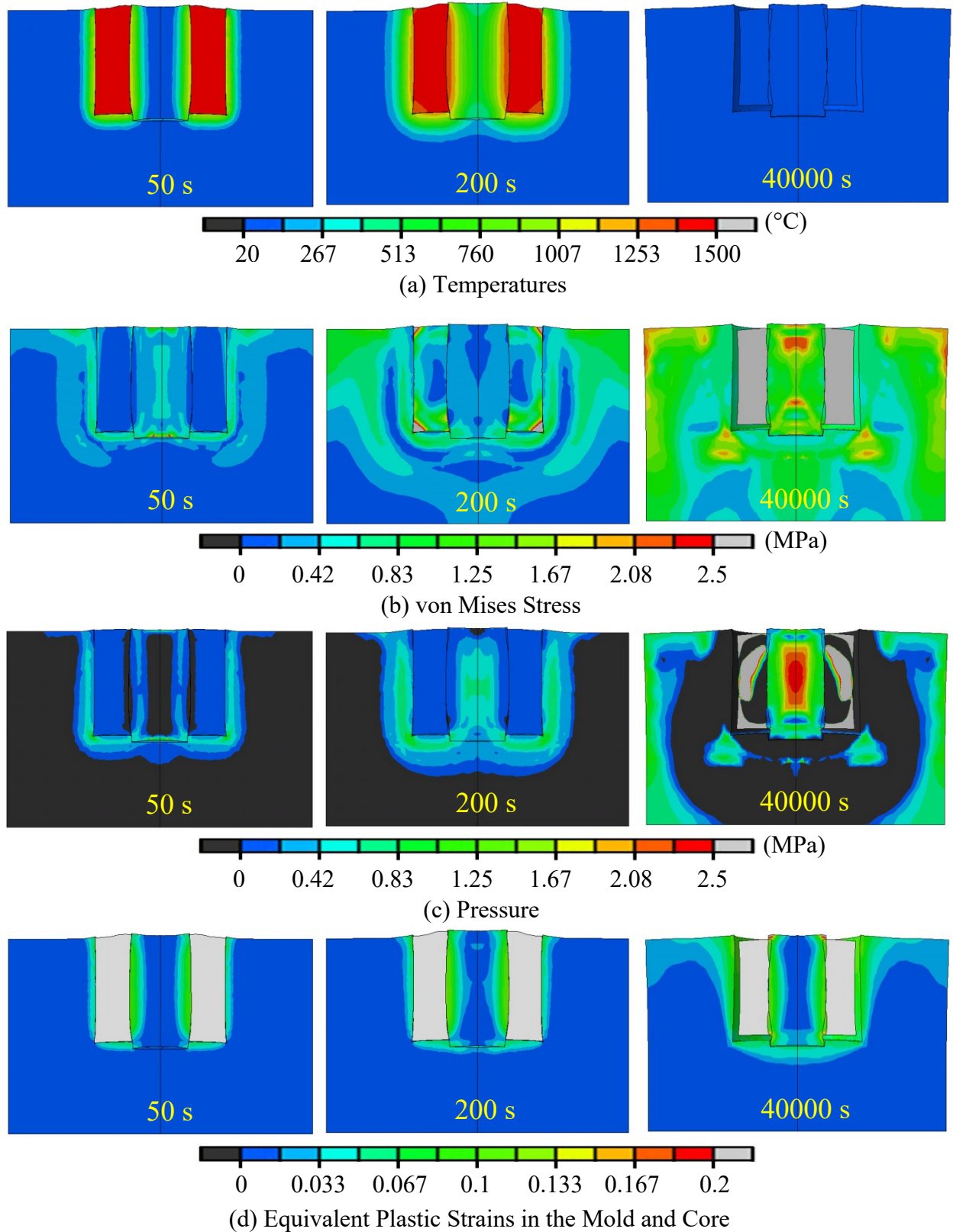


Figure 3.22 Contours of temperature (a), von Mises stress (b), pressure (c), and equivalent plastic strains (d) at 50 s, 200 s, and 40,000 s (room temperature) for the silica core experiments. Distortions magnified by a factor of 5.

dependency on the predicted stresses and strains is unclear. Therefore, this section investigates the uncertainties that are associated with the high temperature bonded sand properties through a series of parametric studies on the silica core experiments (similar results can be expected for the zircon core experiments). These studies will shed light on which high temperature parameters are most important and provide a basis for future testing needs.

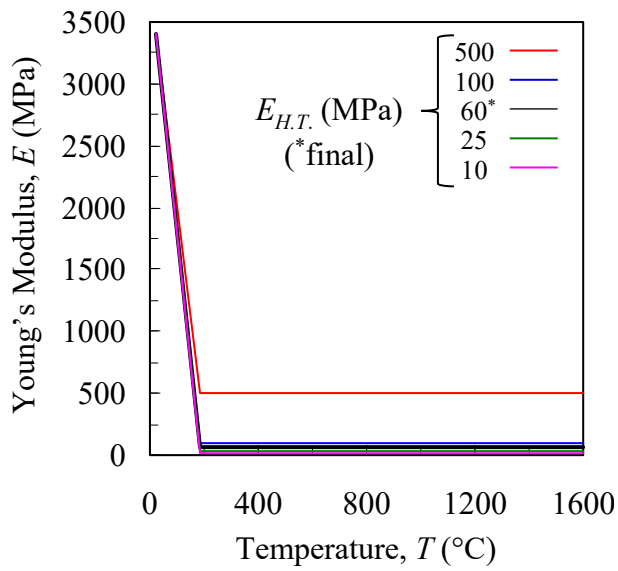
Figure 3.23 illustrates the sensitivity of the predicted inner diameter evolution to changes in Young's modulus. In Figure 3.23(a), $E_{H.T.}$ is varied from 10 MPa to 500 MPa. Using these curves, the predicted inner diameter evolutions in Figure 3.23(b) become increasingly sensitive as $E_{H.T.}$ decreases. For example, the predicted expansion at 200 s decreases by approximately 0.2 mm (9% reduction) when decreasing $E_{H.T.}$ from 500 to 100 MPa. However, decreasing $E_{H.T.}$ from 25 to 10 MPa has a tremendous impact on the predictions, as the predicted expansion at 200 s decreases from 1.3 mm to 0.5 mm (62% reduction). Therefore, setting E as a constant above T_{crit} is reasonable as long as its high temperature value is above 100 MPa. Otherwise, a temperature dependency should be considered above the critical temperature.

In addition to $E_{H.T.}$, the critical temperature for Young's modulus was also varied, as shown in Figure 3.23(c). From the simulation results in Figure 3.23(d), it is obvious that the inner diameter evolution is only sensitive to changes in the critical temperature for $T_{crit} > 180^{\circ}\text{C}$. The parametric study on T_{crit} for the cohesion parameter (see Figures 3.19(c) and (d)) produced similar conclusions. Therefore, based on the parametric studies on T_{crit} , it can be stated with confidence that minimal core expansion due to dilation occurred for temperatures less than 180°C .

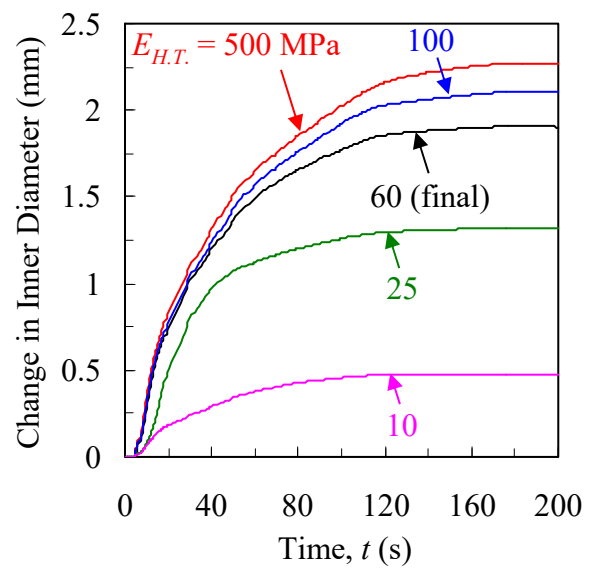
Figure 3.24 shows that the predicted inner diameter evolution is also sensitive to variations in the cap eccentricity, R , which was varied from 0.45 to 3. This result is somewhat counter-intuitive because yielding on the cap surface is associated with compaction, which was not important for the cylinder experiments. The sensitivity of the predicted change in the inner diameter to R can be understood from Figure 3.24(a). An increase in R reduces the span of the shear failure surface, which in turn decreases the amount of predicted dilation. As a result, increasing the value of R decreases the maximum predicted core expansion.

The effect of changes in the normal consolidation line (NCL) were also investigated. The NCL was determined from the slope of 1-D compression test curves at high pressures. Depending on the interpretation of these curves, it could be argued that a different slope should be used, e.g., the "NCL (new slope)" curve in Figure 3.25(a). The result of this adjustment is drastic, as the maximum predicted inner diameter expansion (see Figure 3.25(b)) is roughly half of that from the simulation using the estimated value.

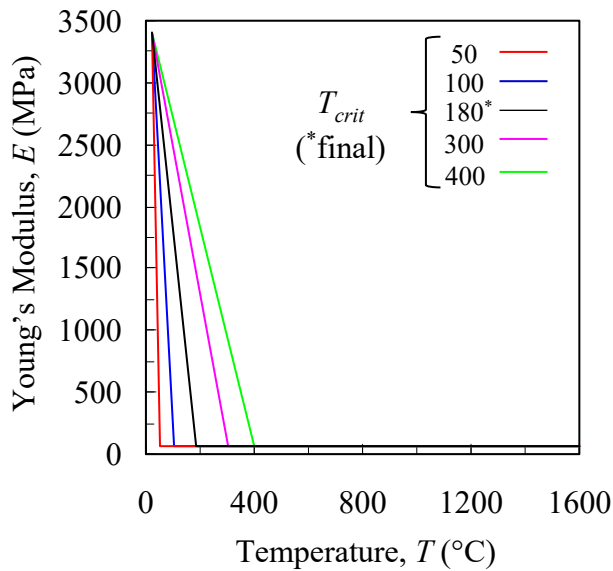
At high temperatures, the hydrostatic compressive strength, p_b , of the bonded sand can be expected to decrease somewhat. This reduction can be modeled by shifting the NCL to the left at high temperatures as shown in Figure 3.25(c). The "NCL 1" curve reduces the high temperature hydrostatic compressive strength to 75% of the room temperature value, whereas the "NCL 2" reduces the high temperature value by 50%. As expected, these reductions reduce the maximum predicted inner diameter expansion as shown in Figure 3.25(d).



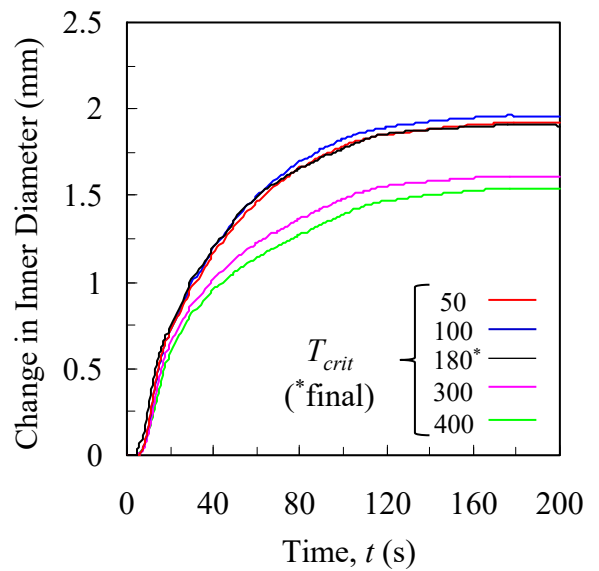
(a) Young's Modulus



(b) Change in Inner Diameter



(c) Young's Modulus



(d) Change in Inner Diameter

Figure 3.23 Parametric study on Young's modulus demonstrating the effect of changes to $E_{H.T.}$ (a) and T_{crit} (c) on the predicted change in inner diameter (shown in (b) and (d)) for the silica core experiments.

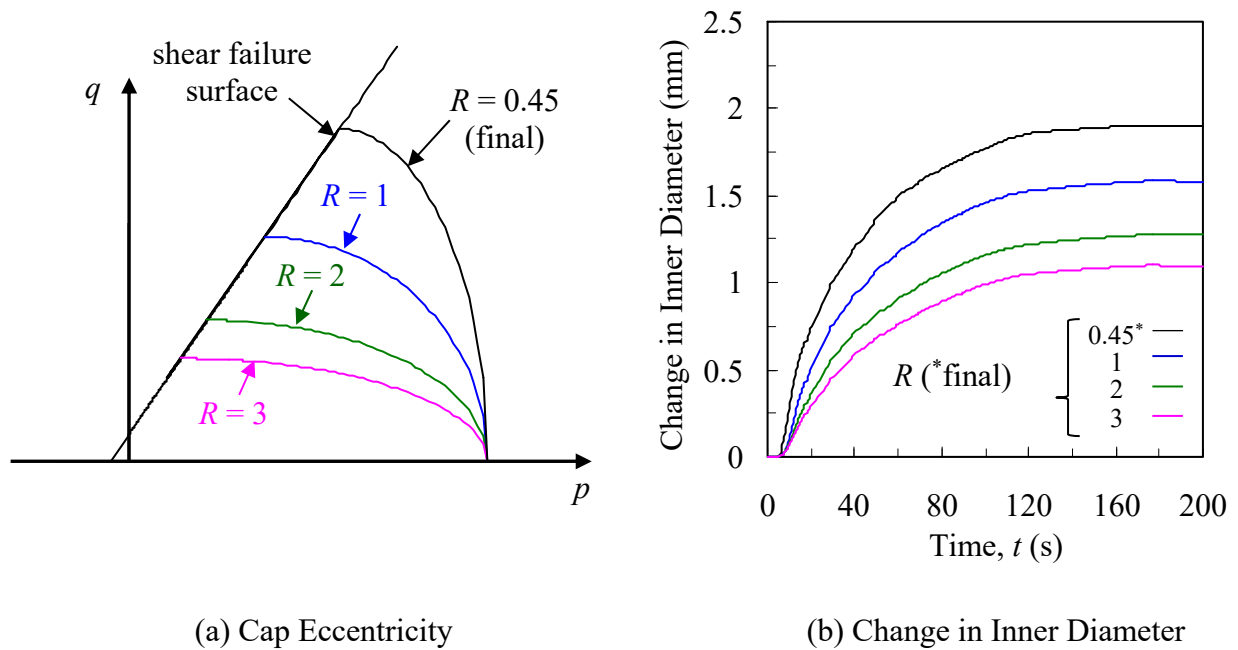
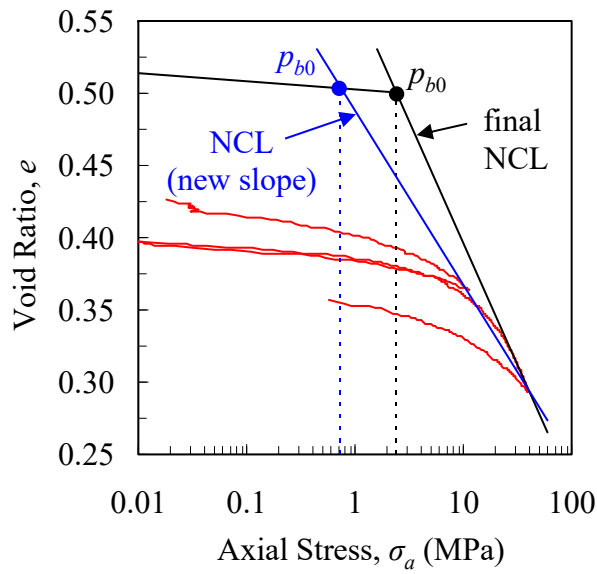
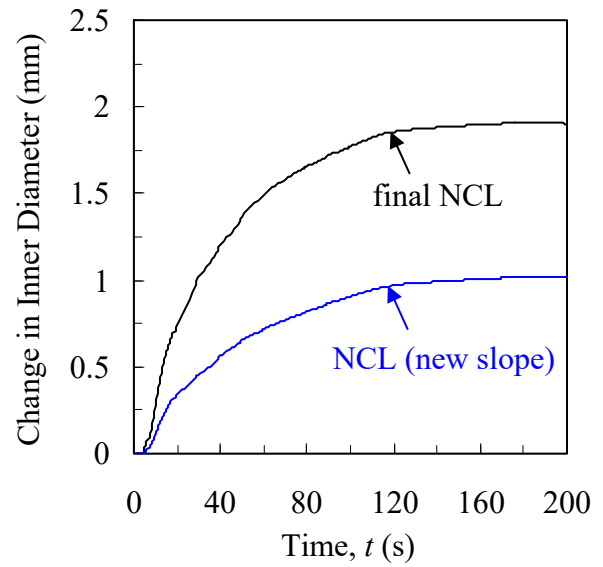


Figure 3.24 Parametric study demonstrating the effect of the cap eccentricity (R) on the predicted change in inner diameter for the silica core experiments.

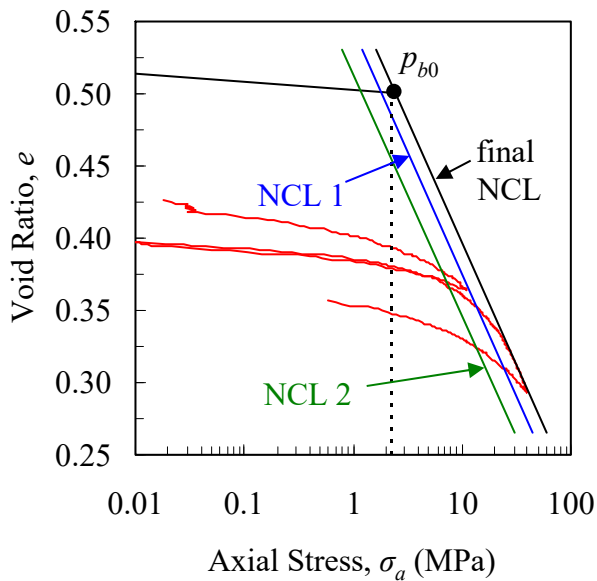
The final parametric study is concerned with controlling process conditions rather than studying high temperature properties. For this study, the effect of the initial bulk density on the finite element predictions was investigated. The initial bulk density was varied between 1700 and 1800 kg/m³. Such variations in the density cause significant variations in the predicted change in inner diameter (see Figure 3.26). These differences illustrate the importance of controlling the packing density during mold construction.



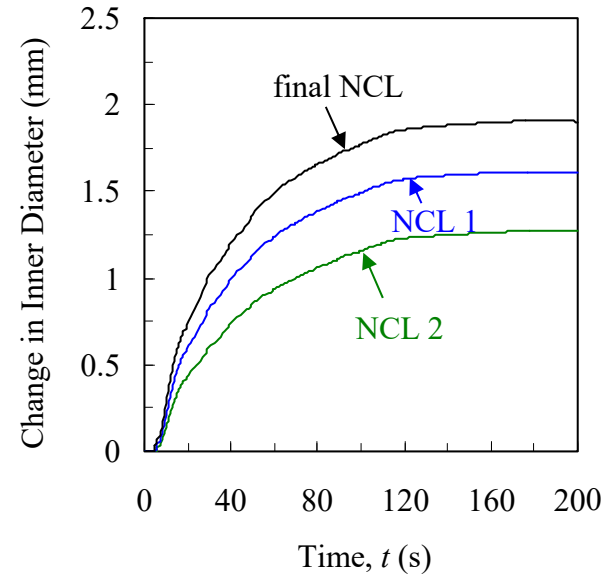
(a) Adjustment to Slope of Normal Consolidation Line



(b) Effect of Changes in Normal Consolidation Line Slope



(c) Shifted Normal Consolidation Lines



(d) Effect of Shifting the Normal Consolidation Line

Figure 3.25 Parametric studies demonstrated how changing the slope (a) of and shifting (c) the normal consolidation line (NCL) affects the predicted change in the inner diameter (shown in (b) and (d)) for the silica core experiments.

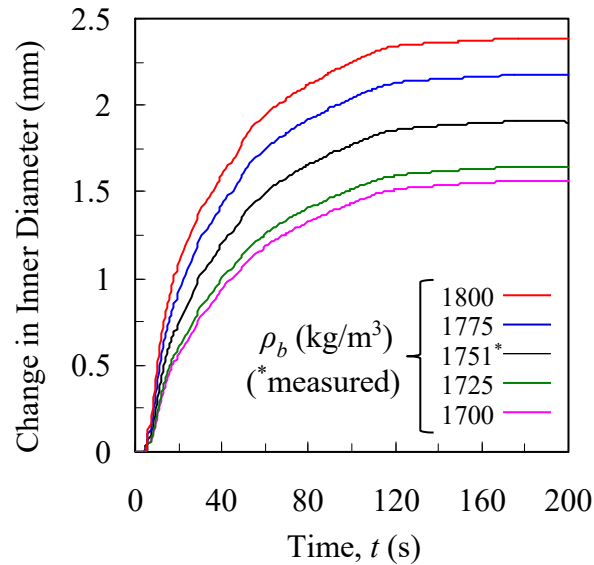


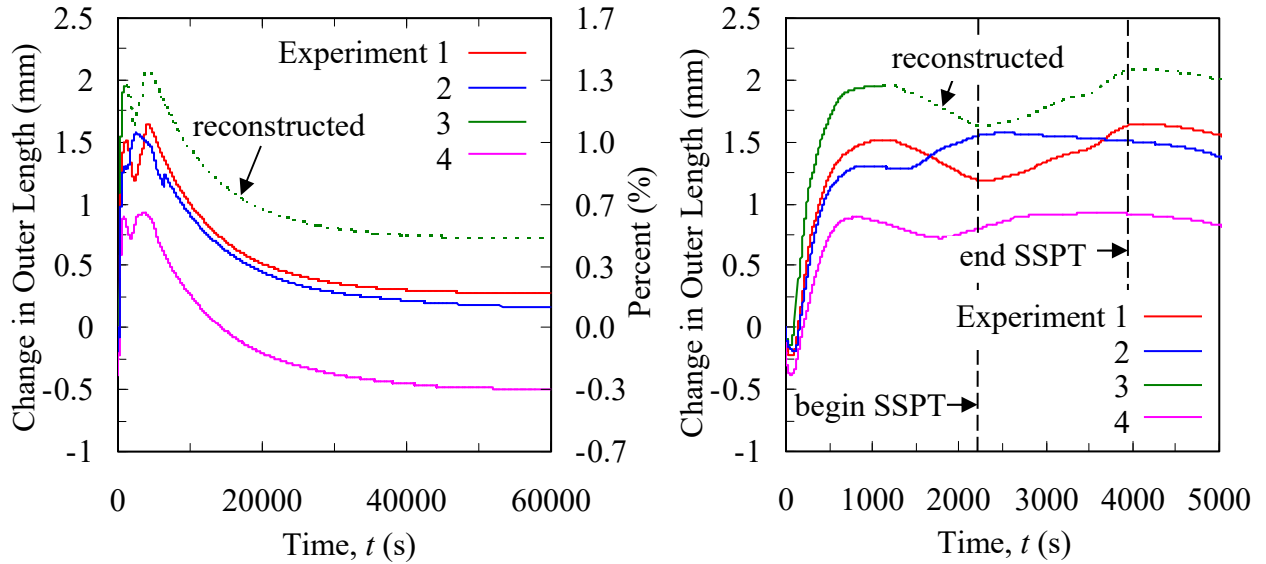
Figure 3.26 Parametric study demonstrating the effect of the initial bulk density on the predicted change in the inner diameter for the silica core experiments.

3.3 Experimental and Simulation Results for Bracket Castings

Experimental Results

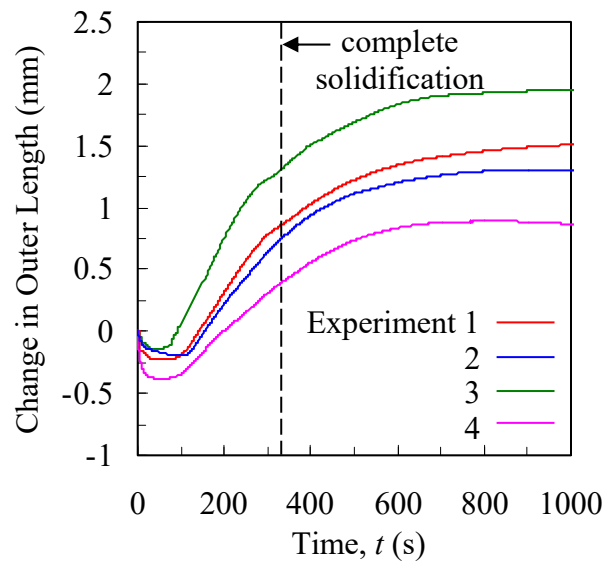
The measured LVDT displacements are plotted in Figure 3.27 as the change in outer length (see Figure 2.3(b) for feature location) vs. time. Results are shown on complete (60,000 s), 5000 s, and 1000 s time scales in Figures 3.27(a), (b), and (c), respectively. The complete time scale represents the approximate time needed to cool the casting to room temperature. The reduced time scales (5000 s, 1000 s) are needed to observe events that are difficult to see on the complete time scale. Each curve represents a separate experiment. Note that for experiment 3 (green curve), one of the quartz rods failed at approximately 1000 s. After this time, the curve was recreated using data from experiment 1 and is represented by a dashed line.

The curves in Figure 3.27 contain several characteristic features which give insight as to when casting distortions occurred and what caused them (i.e., mold expansion or mold constraint). During the initial 50 s, the outer lengths decreased some amount between 0.1 mm (Experiment 3) and 0.4 mm (Experiment 4). This reduction was caused by mold expansion, which was induced by rapid heating of the bonded sand near the mold-metal interface. At these early times, the steel had not yet reached coherency and could be easily displaced by the expanding mold. The consequence of mold expansion, which impacted the entire casting surface, was a volumetric reduction of the casting; the displaced molten steel was forced back into the pouring cup. At approximately 100 s, the outer length increases, as the bracket legs were pushed apart. Such an outward push was only possible if the inner mold acted as a fulcrum, about which each leg pivoted. Complete solidification of the bracket (approximated from the measured cooling rate in the steel) occurred around 325 s (denoted by the vertical dashed line in Figure 3.27(c)), after which the outer length



(a) Complete Time Scale

(b) 5000 s Time Scale



(c) 1000 s Time Scale

Figure 3.27 Measured change in outer length for the bracket experiments plotted on complete (a), 5000 s (b), and 1000 s (c) time scales. The vertical dashed lines in (b) denote the beginning and end of the solid state phase transformation (SSPT) from austenite to α -ferrite and pearlite for experiment 1.

increased by roughly 0.5 mm until reaching a local maximum at approximately 1000 s. During this period, the fully-solid bracket was still very weak and could be easily distorted

by inner mold restraint. The LVDT curves begin to decrease shortly after 1000 s, as the cooling steel had gained sufficient strength and could now overcome the core restraint, pulling the bracket legs inward. This decrease continued until a local minimum, which denotes the onset of the solid state phase transformation in the steel from austenite to pearlite and α -ferrite. The subsequent increase in outer length was the result of the volumetric expansion in the steel associated with the phase transformation. The end of the phase transformation is manifested as a local maximum in the curves, after which the outer lengths decreased monotonically until room temperature. The beginning and end of the phase transformation for experiment 1 are denoted as vertical dashed lines (labeled “begin SSPT” and “end SSPT”). Depending on the experiment, the beginning and end times of the transformation varied, which can be attributed to differences in casting chemistries. For example, the phase transformation for experiment 2 commenced long before those in the other experiments. The carbon content (see Table 3.4) for experiment 2 (0.14%) was considerably lower than the other experiments (0.27-0.33%) and likely had an impact on the temperatures at which the phase transformation began and ended. Other differences can be seen in Table 3.4 (i.e., %P for Experiment 2, %Ni for Experiment 4) that may have also impacted the phase transformation temperatures. After the solid state phase transformation was complete, the outer lengths decreased at the same rate (i.e., all curves are parallel) until room temperature. This observation suggests that all changes in the outer length after the phase transformation were caused by thermal strains (the thermal strain simulations will validate this hypothesis).

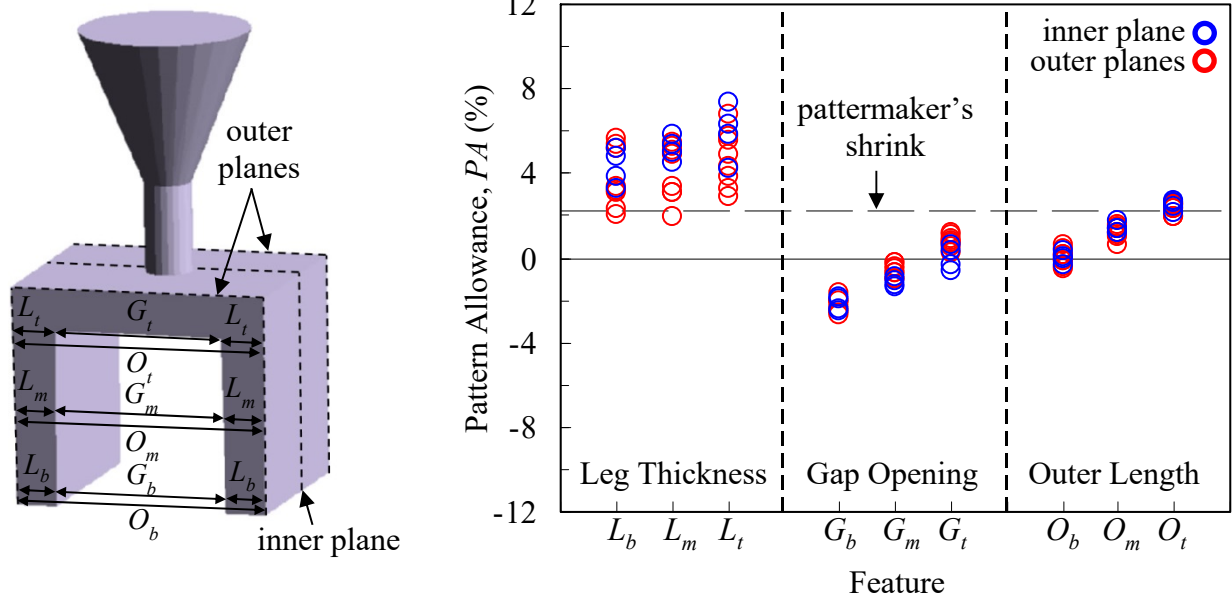
Noticeable scatter in the curves can be seen between individual experiments, as the outer length increased to almost 2 mm for experiment 3 after 1000 s as opposed to only 0.9 mm for experiment 4. These differences can likely be attributed to the packing density (the effect of packing density on predicted distortions is demonstrated below), which signifies the importance of controlling process variables. Recall that the molds were hand-packed, lending to considerable uncertainty in the bulk density of the molds.

Table 3.4 Experimental casting chemistries. The remaining balance is %Fe.

Experiment	%C	%Si	%Mn	%P	%S	%Cr	%Mo	%Ni	%Al	%Cu
1	0.33	0.59	0.39	0.015	0.020	0.01	0.01	0.01	0.069	0.03
2	0.14	0.38	0.26	0.093	0.013	0.02	0.01	0.01	0.001	0.07
3	0.30	0.57	0.41	0.031	0.026	0.01	0.00	0.00	0.056	0.01
4	0.27	0.23	0.61	0.012	0.009	0.63	0.19	2.0	0.021	0.04

In addition to the LVDT measurements, pattern allowances (*PA*) were measured for the leg thickness (*L*), gap opening (*G*), and outer length (*O*) on two outer and one inner planes, as shown in Figure 3.28(a). The subscripts indicate that the measurements were taken at the bottom (*b*), mid-height (*m*), or top (*t*) of the bracket legs. The bottom and top measurements were taken 5 mm above the bottom of the bracket legs and 5 mm below the bottom surface of the top section, respectively. The measured pattern allowances are shown in Figure 3.28(b). The patternmaker’s shrink (i.e., pattern allowance due to thermal strains) is indicated in Figure 3.28(b) by a vertical dashed line and serves as a reference. Any deviation from this line represents a distortion. Keep in mind that a larger pattern allowance signifies a greater reduction in the feature length during casting. In general, the leg thickness (*L*) pattern allowances exceeded the patternmaker’s shrink. The additional reduction (over the patternmaker’s shrink) in *L* was caused by mold expansion during

solidification, which “squeezed” the legs and reduced their thicknesses. Then, from the end



(a) Bracket Feature Locations

(b) Measured Pattern Allowances

Figure 3.28 Pattern allowances were measured on inner and outer planes for the features shown in (a). Standard deviations for the measurements in (b) ranged from 0.1 – 0.2 mm.

of solidification until cooling to room temperature, L thermally contracted unconstrained and was reduced an additional amount equal to the patternmaker's shrink. On average, the inner plane pattern allowances (blue symbols) were slightly larger than the outer plane pattern allowances (red symbols) for L . This is because the outer planes solidified before the inner planes. Once the solidifying steel becomes coherent (i.e., can transmit stresses), any further reduction in L due to mold expansion is unlikely. Hence, shorter solidification times will lead to smaller pattern allowances for L , which also explains why the average pattern allowance for L_t is greater than those for L_b and L_m . The leg thickness pattern allowance measurements also contain more scatter than the gap opening or outer length measurements. The standard deviation for the measurements ranged from 0.1-0.2 mm, depending on surface roughness. This variation caused the most scatter in the pattern allowances for L , whose nominal dimension (25 mm) is much smaller than G (100 mm) and O (150 mm). For the gap opening (G), all measured pattern allowances were less than the patternmaker's shrink. In contrast to the pattern allowances for L , mold expansion caused G to increase (this can be visualized from Figure 3.28(a)), reducing the pattern allowance. In addition, inner mold constraint pushed the legs outward and reduced the pattern allowances further. As a result, the combined effect of inner mold expansion and inner mold constraint led to negative pattern allowances for the majority of the gap opening features. In other words, the majority of these feature lengths increased during casting. In general, the pattern allowances for $G_b < G_m < G_t$, which should be expected as long as the bracket legs remain planar. The inner plane pattern allowances were somewhat smaller than the outer plane pattern allowances for G . This difference can again be attributed to

local solidification times in the bracket. On average, the outer length (O) pattern allowance measurements are closer to the patternmaker's shrink than those for L or G . In particular, O_i appears to have experienced minimal distortions, as all the pattern allowance measurements are close to the patternmaker's shrink. However, it is clear from Figure 3.28(a) that $O = 2L + G$. Essentially, the addition of L and G “cancelled out” distortions, resulting in pattern allowance measurements that were deceptively close to the patternmaker's shrink.

From Figures 2.3(b) and 3.28(a), it can be seen that O_{LVDT} and O_b are the same feature. The negative change in inner diameter at 60,000 s (see Figure 3.27(a)) was used in the numerator of Eq. [1] to determine the pattern allowances for O_{LVDT} . These values are compared to the pattern allowances for O_b in Figure 3.29. For $O_{LVDT} = O_b$, the symbol will fall on the 45° line in the figure. Experiment 4 (pink symbol) nearly falls on this line, whereas larger discrepancies between O_{LVDT} and O_b can be seen for the other brackets. These differences can be attributed to slippage between the quartz rods and casting during solidification, as explained by Galles and Beckermann¹⁹. To remedy this, the LVDT measurements will be adjusted slightly during the initial 50 s to match the calipers measurements. In general, these adjustments are minor and do not affect the overall shapes of the measurement curve. The main effect of the adjustments is that differences between the LVDT curves were minimized during the initial 50 s. All subsequent plots that show LVDT measurements will now use the adjusted curves (see Chapter 5), which are labeled

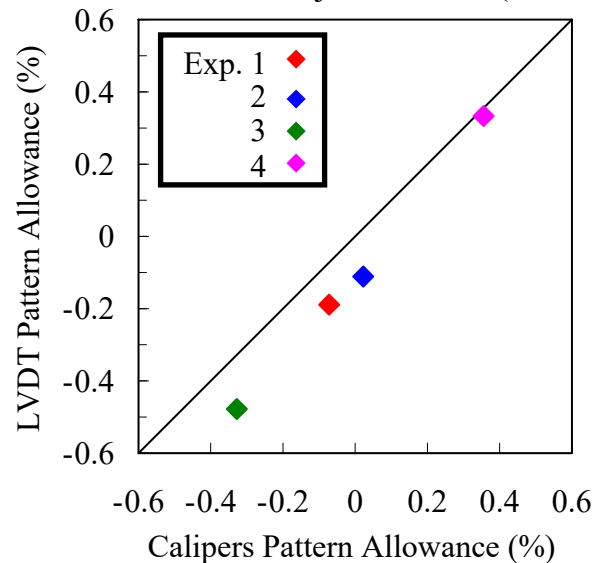


Figure 3.29 Comparison between the LVDT and calipers pattern allowances for feature O_b on the inner plane (see Figure 3).

appropriately.

Casting Bracket Thermal Simulation Results

Using the commercial casting software code MAGMASOFT[®],^[20] temperatures were calculated in the casting and mold from the time of filling until the casting cooled to room temperature. Virtual thermocouples were placed in the simulation model at the

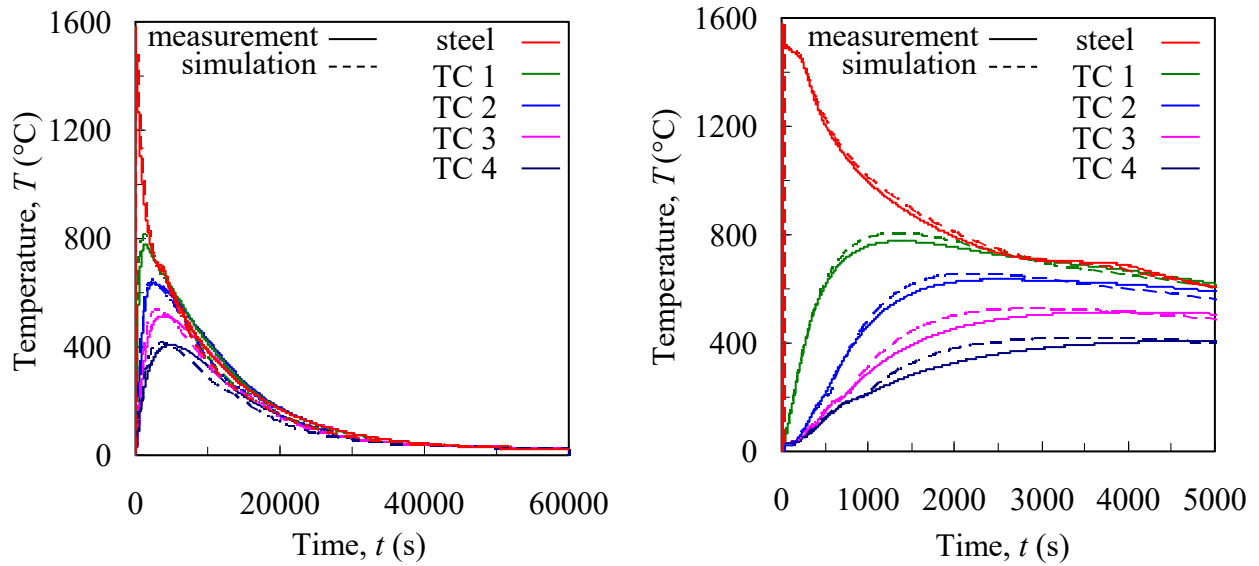
experimental locations. Predicted temperatures at these locations were later compared to the measured temperatures for validation. Simulation inputs included temperature dependent thermophysical properties (i.e., density, specific heat, thermal conductivity) for the steel and bonded sand, as well as latent heat of solidification and the temperature dependent solid volume fraction for the steel. The interfacial heat transfer coefficient (IHTC) governs the heat transfer across the mold-metal interface and accounts for the evolution of an air gap during cooling. Inclusion of the IHTC allows for a decoupling of the thermal-mechanical problem.

The input parameters were calibrated for PUNB bonded silica sand by Galles and Beckerman^[19] using a procedure described elsewhere.^[22,23] In general, the predicted and measured temperatures agreed reasonably well. The IHTC was then modified slightly, which resulted in excellent agreement between the measured and predicted temperatures, as shown in Figures 3.30(a) and (b) on complete and 2500 s time scales, respectively. Figure 3.30(c) illustrates the uneven solidification that is predicted in the bracket. It can be seen that the bottoms of the bracket legs are over 50% solidified at 25 s. Around this time, the steel reaches coherency, after which minimal mold expansion can be expected. These predictions coincide with the LVDT measurements in Figure 3.27(c); the majority of the decrease in outer length occurs during the initial 25 s, after which minimal amounts are observed between 25 s and 50 s. Temperature fields were written at a sufficient number of time steps (in order to ensure a smooth temperature profile at every node) and then copied onto the finite element mesh.

Casting Bracket Thermal Strain Predictions

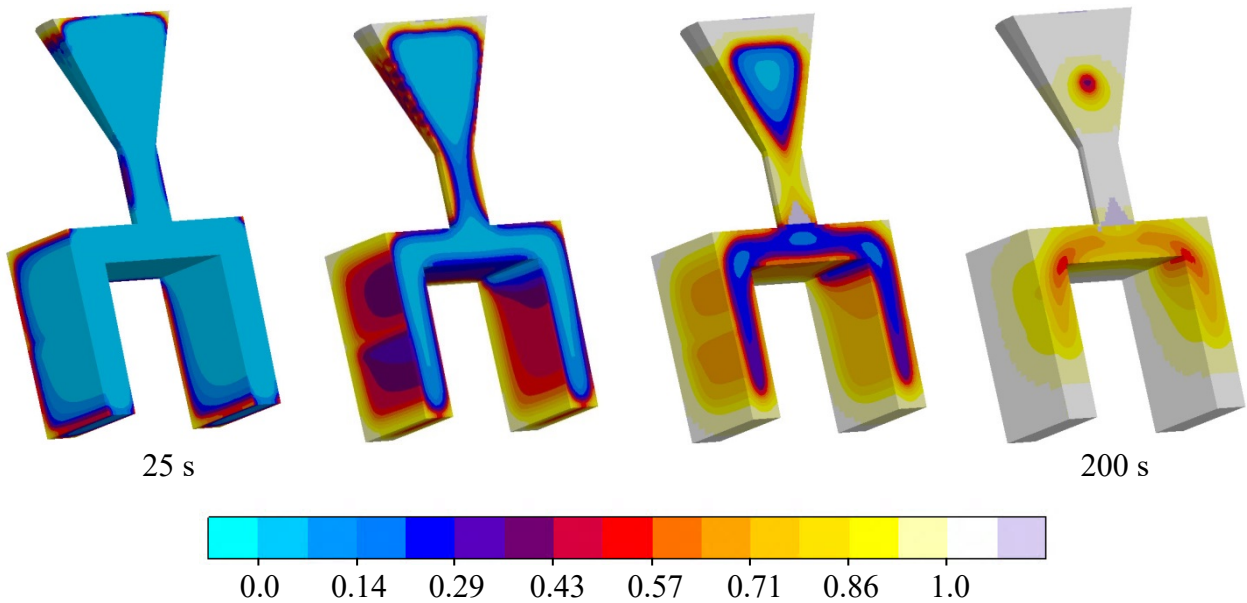
Preliminary finite element simulations calculated the thermal strains in the bracket. A comparison of these predictions with the LVDT measurements will reveal when distortions occurred and thus, provide invaluable insight to the mechanism that created them. The mold was excluded from the simulation in order to prevent any distortions due to mechanical interactions between the mold and bracket. Thus, only the bracket was simulated, for which minimal boundary conditions were specified to prevent rigid body translations or rotations. Young's modulus for the steel was set to a very low value (1×10^{-6} MPa), ensuring that negligible mechanical strains due to thermal stresses were predicted.

The predicted evolution of the outer length due to thermal strains is compared to the LVDT measurements on complete, 5000 s, and 1000 s time scales in Figures 3.31(a), 3.31(b), and 3.31(c), respectively. Thermal strains in the steel were calculated using the linear thermal expansion curve in Figure 3.31(d), which was calibrated by Galles and Beckermann.^[19] The "kink" in the linear thermal expansion curve at approximately 700°C is included to predict dimensional increases associated with the solid state phase transformation. The onset of thermal contraction is based on the findings of Galles and Beckermann^[19] and was set to $g_s = 0.97$. Hence, thermal strains will not be predicted until shortly before complete solidification. This can be seen in Figure 3.31(c), in which the thermal strain simulation curve begins to decrease at 300 s, about 25 s before complete solidification. Clearly, the measured outer length is distorted during this time frame (see experimental results section for a detailed explanation). From 100 s to 300 s, the LVDT curves increased. Because the top section of the bracket had not yet started to thermally contract, the increase in outer length during this period can only be attributed to inner mold expansion (and not inner mold restraint). At 300 s, the onset of thermal contractions were



(a) Complete time scale

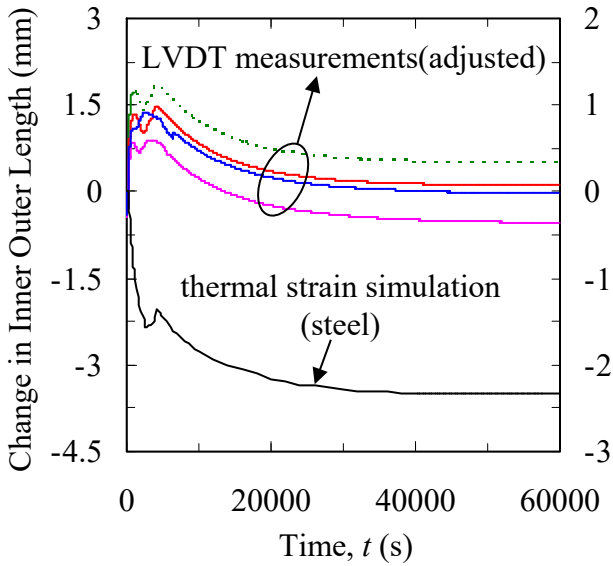
(b) 2500 s time scale



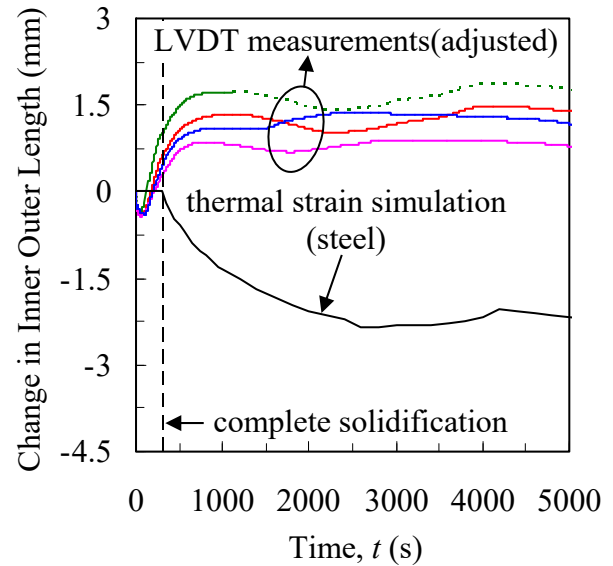
(c) Fraction Solid

Figure 3.30 Comparison between measured and predicted temperatures on complete (a) and 5000 s (b) time scales. The predicted fraction solid contours in (c) illustrate uneven solidification.

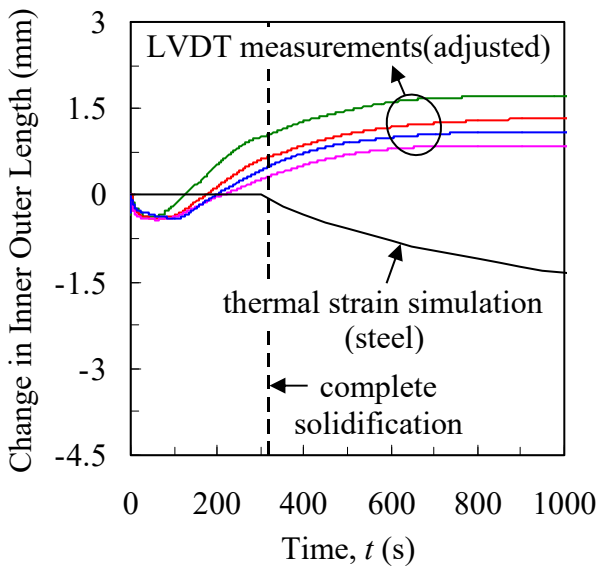
predicted and pulled the legs inward. As a result, the thermal strain simulation curve decreases until a local minimum at approximately 2500 s, which represents the onset of solid state phase transformation. Prior to the thermal strain simulation, it was already obvious from the increasing LVDT curves that the outer length was distorted from 300 s to 1000 s during the experiments. Now, by comparing the measured and simulated slopes of



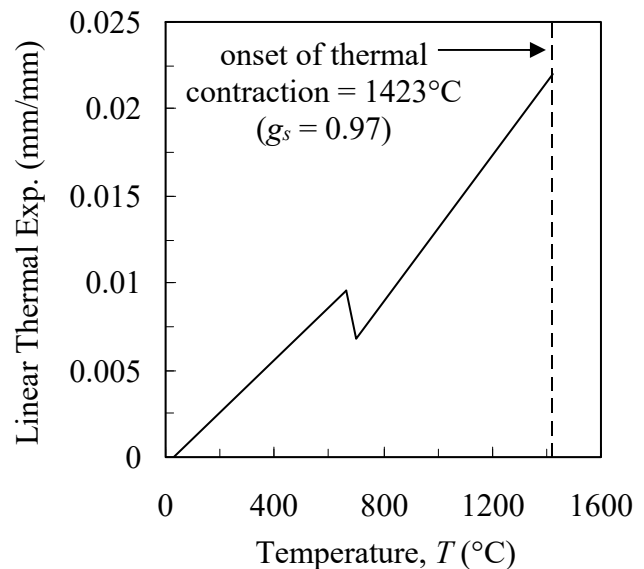
(a) Complete Time Scale



(b) 5000 s Time Scale



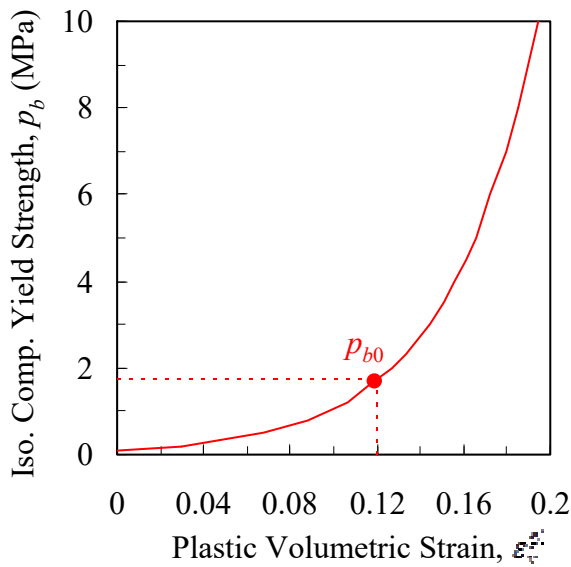
(c) 1000 s Time Scale



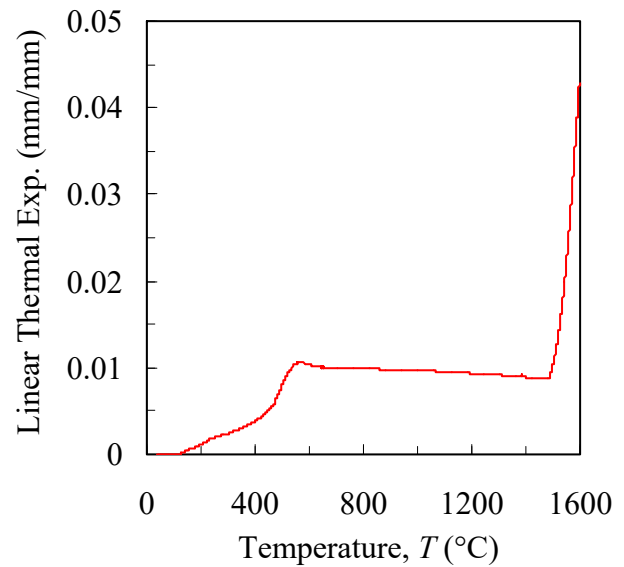
(d) Linear Thermal Expansion of Steel

Figure 3.31 Comparison between the predicted change in outer length due to thermal strains in the steel and the LVDT measurements. Thermal strains in the steel were calculated using the linear thermal expansion in (d).

the curves after 1000 s, it is also evident that distortions were generated until the beginning of the solid state phase transformation. During this period, inner mold restraint prevented the outer length from contracting at the same rate as the thermal strain prediction. Although the increase in measured and simulated outer lengths does not necessarily match during the phase transformation, it is unlikely that distortions were generated during this period. As



(a) Isotropic Compressive Yield Strength vs. Volumetric Strain



(b) Measured Linear Thermal Expansion of Bonded Silica Sand

Figure 3.32 The plot in (a) governs the evolution of the hydrostatic compression strength (p_b) for the bonded sand with increments of plastic volumetric strain and defines the hardening behavior. Here, a positive plastic volumetric strain represents a reduction in volume. The initial hydrostatic compressive strength (p_{b0}) was calculated from the initial bulk density. Thermal strains in the bonded sand were predicted using the linear thermal expansion behavior shown in (b).

previously stated, differences in the LVDT measurements during the solid state phase transformation are likely due to variations in the casting chemistry (see Table 3.4). After the phase transformation, the LVDT measurements and thermal simulation curve are parallel (i.e., contract at the same rate), signifying that all dimensional changes after the phase transformation are due to thermal strains.

Bracket Casting Stress Simulation Results

Inputs for the stress simulations include the elastic mechanical properties and viscoplastic parameters for the steel^[19] and bonded sand (given in Table 3.5), thermal expansion coefficients for the steel (Figure 3.31(d)) and bonded sand (Figure 3.32(b)), and the calculated temperature fields from MAGMASOFT®. The hardening behavior of the bonded sand must also be specified and is governed by Figure 3.32(a), which plots the hydrostatic compressive strength (p_b) of the bonded sand as a function of plastic volumetric strain. In order to determine the initial hydrostatic compressive strength (p_{b0}), the initial bulk density (i.e., packing density) of the bonded sand is also required^[41] Unfortunately, the bulk density was not measured prior to the experiments. Instead, a representative bulk density ($\rho_b = 1710 \text{ kg/m}^3$) was estimated from a hand-packed bonded sand sample. From this initial bulk density, p_{b0} was determined to be 1.7 MPa.

Table 3.5 Mechanical properties and Drucker-Prager Cap parameters for the silica bonded sands.

Temperature (°C)	E (MPa)	ν	β	d (MPa)	R	α
20	3403	0.3	55°	1.85	0.45	0.01
180	60	0.3	55°	0.11	0.45	0.01
1600	60	0.3	55°	0.11	0.45	0.01

Using the inputs, a stress simulation predicted the change in outer length, which is compared to the LVDT measurements in Figure 3.33. The observed decrease in outer length during the initial 50 s (due to mold expansion) was reasonably predicted, as the stress simulation curve decreases to -0.4 mm. After 50 s, however, the stress simulation curve does not match the LVDT measurements. In particular, the LVDT curves increase at a much higher rate than the stress simulation curve between 100 s and 1000 s. In other words, the bracket legs were pushed outward much faster in the experiments than the simulations. Additionally, the observed decrease in the outer length after 1000 s was not predicted. The stress simulation curve is approximately parallel to the red LVDT curve after the onset of the solid state phase transformation (SSPT), i.e., the local minimum at 2500 s. However, because distortions were not generated after the SSPT commenced (this was demonstrated by the thermal strain simulations), these later times are not particularly interesting. Thus, the finite element stress simulation could not predict the outer length evolution for the time period during which distortions were observed.

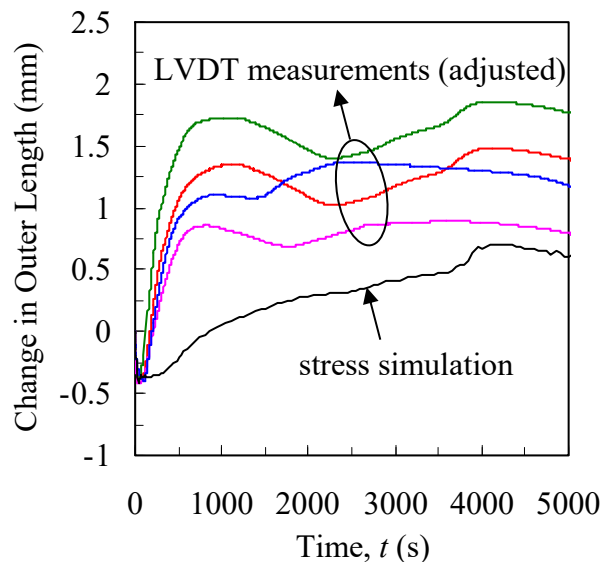
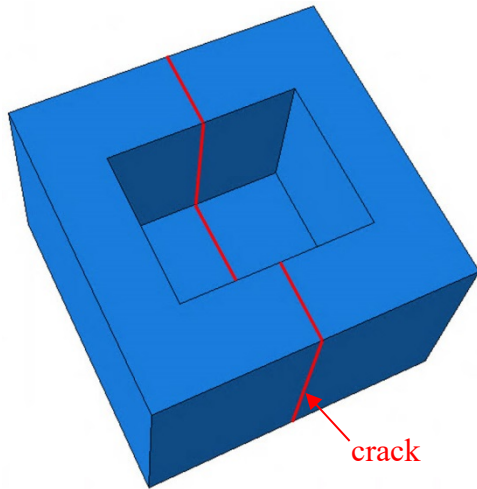
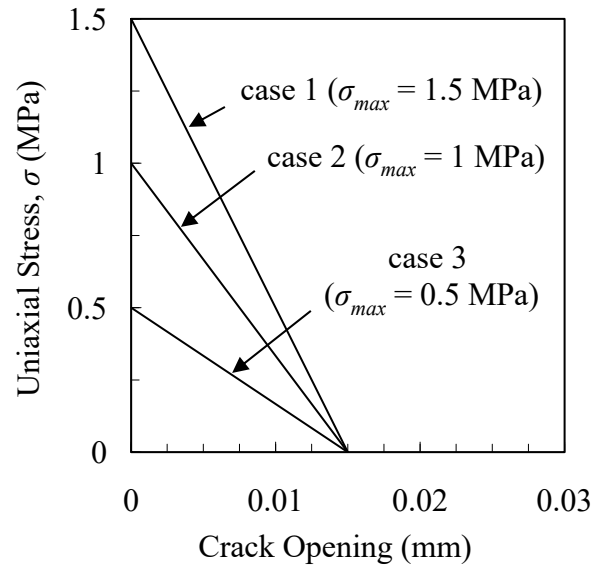


Figure 3.33 Comparison between the LVDT measurements and the predicted change in outer length using the bonded sand properties in Table 2.

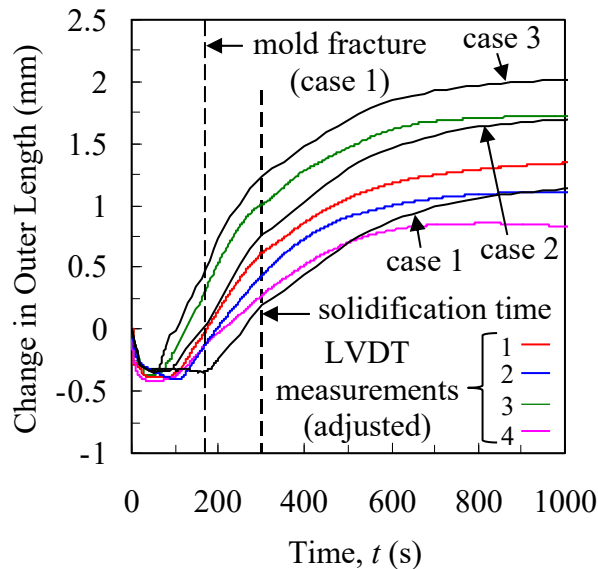
During the experiments, the drag fractured at the location shown in Figure 3.34(a), shortly after pouring. Until the time of fracture, the tensile strength of the outer mold provided restraint that prevented the bracket legs from being pushed outward. At the time of fracture, however, this strength rapidly deteriorated, which essentially eliminated any restraint. After this, the bracket legs could be easily pushed outward by the thermally expanding inner mold.



(a) Observed Crack Plane in Drag



(b) Stress-displacement Behavior after Onset of Crack



(c) Change in Outer Length

Figure 3.34 Mold fracture was observed at the location shown in (a). A parametric study demonstrated the effect of the post-cracking stress-strain behavior in (b) on the predicted change in outer length (c).

To simulate this behavior, a crack plane was defined in the model at the observed location of fracture using surface-based cohesive behavior in ABAQUS®/explicit. Once the tensile capacity in the cohesive bond is reached, the bond degrades as the surfaces are pulled apart. This degradation is governed by stress-displacement behavior such as that shown in Figure 3.34(b), in which the tensile strength of the bonded sand linearly decreases from a maximum tensile stress (σ_{max}) to zero at some finite crack opening (0.015 mm for this study). The three cases shown in Figure 3.34(b) contain different values for σ_{max} . Such variations are needed in order to predict mold fracture at different times (Figure 3.27(a) illustrates that the experiment 3 mold fractured earlier than those in the other experiments). The curves were based on a uniaxial tensile test performed on a sodium silicate bonded sand by Caylek and Mahnken^[16], who measured a maximum tensile stress of 1.3 MPa. A linear stress-displacement behavior was employed, which was based on finite element predictions that the cohesive bond failed in a matter of seconds (< 10), regardless of the type of relation (i.e., linear, exponential, power series). Using the curves in Figure 3.34(b), a parametric study investigated the sensitivity of the predicted outer length evolution to changes in σ_{max} . The tensile strengths in Figure 3.34(b) were linearly decreased from room temperature to a very small value at the pyrolysis temperature (180°C for this study), which was determined from the measured heating curves in the bonded sand. Pyrolysis of the binder is an endothermic reaction that reduces the local heating rate to nearly zero. Results of the parametric study are shown in Figure 3.34(c). Now it can be seen that the predicted outer lengths increase at rates similar to those observed in the experiments. These increases coincide with the predicted times of fracture and are henceforth referred to as the time of mold fracture. For example, the time of mold fracture for case 1 (175 s) is denoted by a vertical dashed line in Figure 3.34(c). As σ_{max} decreases, mold fracture is predicted earlier, which in turn leads to larger amounts of distortions. For example, case 3 ($\sigma_{max} = 0.5$ MPa) predicts mold fracture at approximately 80 s and a maximum change in outer length of 2 mm at 1000 s. In contrast, case 1 ($\sigma_{max} = 1.5$ MPa) predicts mold fracture at a much later time (175 s), resulting in a maximum change of only 1.1 mm at 1000 s. Interestingly, these simulations have shown that the outer mold restraint impeded the pushout of the bracket legs and actually prevented distortions. This counters the intuition that mold restraint always generates distortions.

The inclusion of a crack plane in the finite element model provides a mechanism for predicting the steep increase that was observed in the outer length, particularly between 100 s and 500 s (see Figure 3.27(c)). During the experiments, the maximum change in outer length (which occurred at approximately 1000 s) ranged from 0.75 mm (for experiment 4) to 1.75 mm (for experiment 3). By modifying the stress-strain curves in similar fashion to those in Figure 3.34(b), these observed variations can now be predicted. However, such modifications may also lead to considerable disagreement between the measurements and predictions at earlier times. This can be seen when comparing the “case 1” simulation to the experiment 2 LVDT measurement (blue curve) in Figure 3.34(b). Although both curves show the same change in outer length at 1000 s, the measured outer length begins to increase at 120 s, whereas the predicted outer length increases much later, at 175 s. It is clear that in order to predict the change in outer length for experiment 4 at 1000 s, σ_{max} would have to be further reduced, which would cause the predicted time of mold fracture to occur even later. Therefore, the outer length evolutions cannot be

predicted solely through modifications to the stress-strain curves (that govern the degradation of the cohesive bond). Another mechanism must be considered.

Recall that the molds for the bracket experiments were hand packed. Using this technique, some amount of variation in the initial bulk density (ρ_{b0}) between the experiments can be expected. The effect of the bulk density on the bonded sand strength is illustrated on the void ratio (e) vs. $\log p$ (where p is the pressure) plot shown in Figure 3.35(a). The nearly-horizontal curves are loading-reloading lines and were constructed through a procedure described by Galles and Beckermann^[19]. The intersection of the loading-reloading lines and the normal consolidation line (NCL) define the initial hydrostatic compressive strength (p_{b0}) of the bonded sand. From the figure, it can be seen that as the initial bulk density increases, p_{b0} also increases. Intuitively, this makes sense; a densely-packed sand has a higher compressive strength than a loosely-packed sand. Therefore, the effect of the initial hydrostatic yield stress was investigated through a parametric study, in which the change in outer length was predicted using the p_{b0} values shown in Figure 3.35(a) (i.e., 0.7 MPa, 1.35 MPa, and 2.5 MPa). To model the degradation of the cohesive bond, the “case 2” curve in Figure 3.34(b) was used. Results are shown in Figure 3.35(b). Clearly, different initial bulk densities have a large impact on the predictions, as the predicted change in outer length varies from 0.5 mm to 2 mm at 1000 s. The family of predicted curves in Figure 3.35(b) looks similar to the predictions in Figure 3.34(c) with one important exception; the magnitudes of the curves are now independent of the mold fracture time. This is in contrast to the previous parametric study, in which variations in σ_{max} affected both the magnitudes of the predicted curves and times of mold fracture. This notable difference provides the means needed to predict the observed outer length evolution.

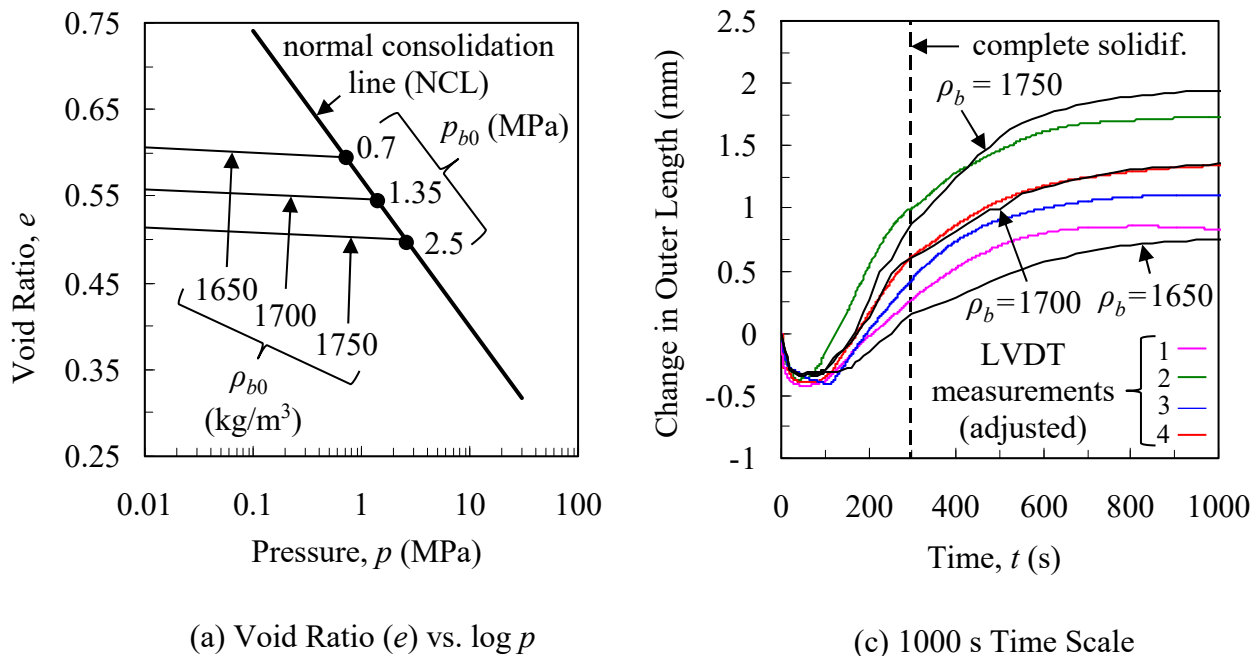
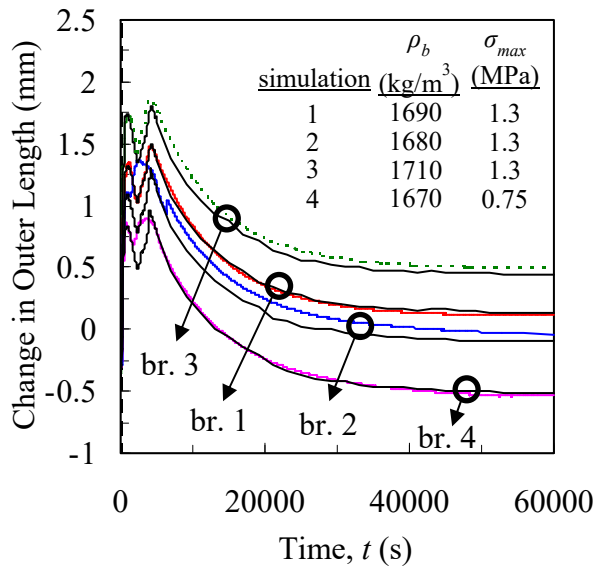


Figure 3.35 A parametric study demonstrated the effect of the bulk density of the bonded sand on the predicted change in outer length.

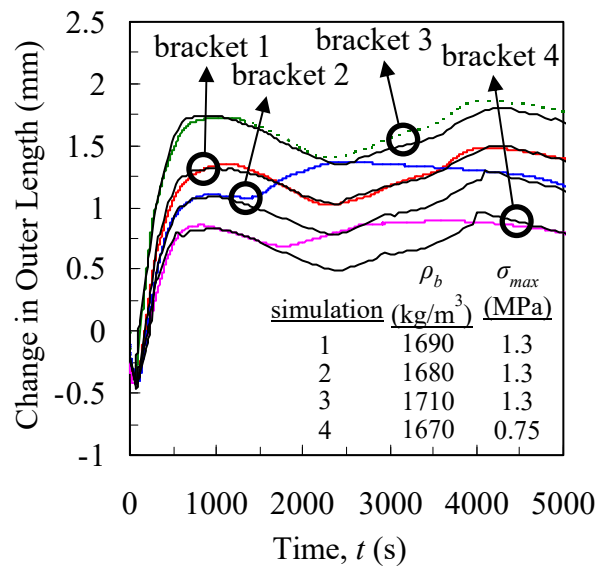
In order to match the measured and simulated changes in outer lengths, the maximum uniaxial stress was first adjusted so that the measured and simulated mold fracture times were matched. As in the parametric study, the tensile strength was linearly decreased from σ_{max} to zero at a crack opening of 0.015 mm. Then, the density was adjusted (which affected p_{b0}) so that the correct magnitude of pushout was predicted. The results are shown on complete (a), 5000 s (b), and 1000 s (c) time scales in Figure 3.36. The maximum tensile stress and bulk densities used for the simulations are listed for each experiment within the figures. Now, the measurements and simulations are in excellent agreement at all times, with the exception of experiments 2 (blue curve) and 4 (pink curve) between 1500 s and 4000 s. The disagreement at these times is likely due to differences in the casting chemistries (see Table 3.4) that caused variations in the time and duration of the solid state phase transformation (SSPT). During this time period, the measured and predicted curves first diverged but eventually converged again. By modifying the kink in Figure 3.31(c) for each individual experiment, the disagreements during the SSPT could have been eliminated. However, this added effort would not have affected the pattern allowance predictions, and therefore, was not performed.

Pattern allowance comparisons for experiment 1 are shown in Figure 3.37(a). In general, the predictions (solid diamond symbols) are in excellent agreement with the measurements (hollow circular symbols). In addition, the bias seen between the inner plane (blue) and outer plane (red) pattern allowances for the leg thicknesses (L) were predicted. In order to quantify the error for the predicted pattern allowances, the root mean square error (RMSE) was calculated for each experiment and is shown in Figure 3.37(b). PA_{RMSE} varied from 0.39% (experiment 1) to 0.52% (experiment 3). For comparison, using the patternmaker's shrink gives a root mean square error of greater than 2%.

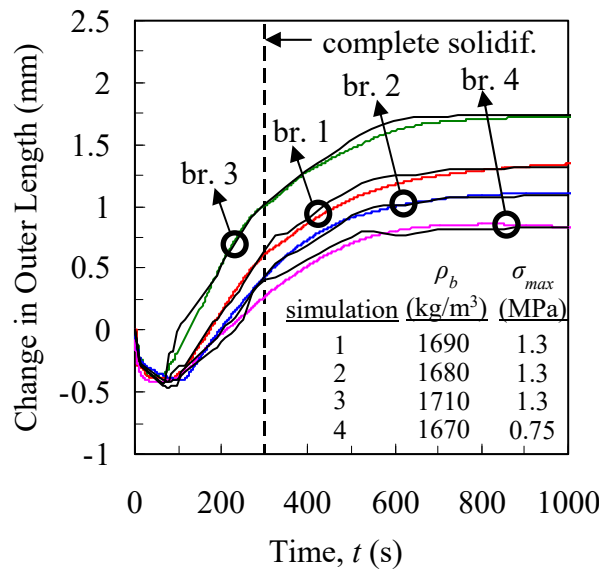
Predicted von Mises stresses and equivalent plastic strains in the casting and mold for experiment 1 are shown in Figure 3.38. Distortions are magnified by a factor of 5. At 200 s, mold fracture has already occurred, as a gap can be seen between the two drag halves. The bracket legs are clearly pushed outward at 1000 s. Note that different stress scales are used for each time in Figure 3.38(a). Figures 3.38(b) and (c) show the predicted equivalent plastic strains in the mold due to yielding on the shear failure and cap surfaces, respectively. Therefore, the contours in Figures 3.38(b) and (c) indicate sand dilation and sand compaction, respectively. For the inner mold region, shear stresses such as those in Figure 3.38(a) at 200 s were necessary to predict the large amounts of equivalent plastic strains associated with the shear failure surface (Figure 3.38(b)). The minimal amount of equivalent plastic strains predicted on the cap surface imply that very little compaction was predicted for the inner mold. However, this is not to say inner mold restraint was unimportant. Likely, the compressive strength of the inner mold was already sufficient to provide considerable restraint and generate distortions. The largest amounts of equivalent plastic strains in the bracket were predicted on the bottom surface of the top section, at the mid-plane (see Figure 3.38(d)). This coincides with the maximum stresses predicted in the bracket (see Figure 3.38(a) at 1000 s). The von Mises stresses in the bracket at 60,000 s represent the residual stresses, which average roughly 40 MPa throughout the bracket with some localized regions approaching 80 MPa.



(a) Complete Time Scale

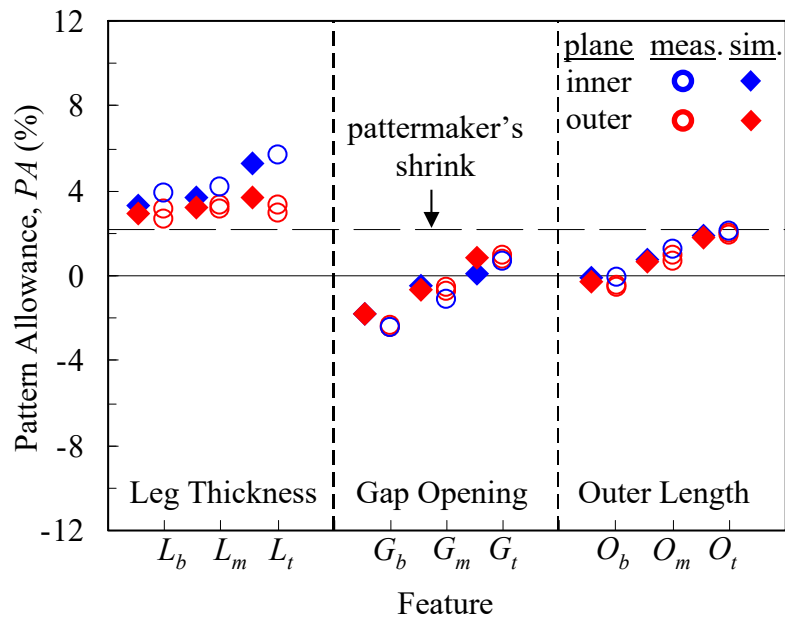


(c) 5000 s Time Scale

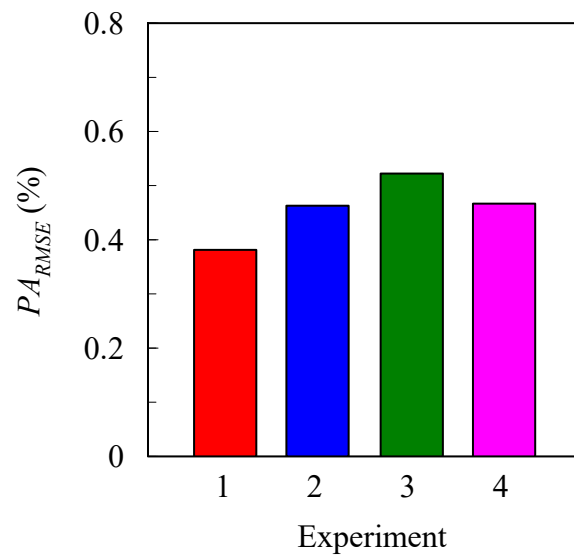


(c) 1000 s Time Scale

Figure 3.36 Comparison between the measured and predicted (black curves) changes in the outer length for the bracket experiments after adjusting the bulk density (ρ_b) and maximum tensile stress of the crack plane (σ_{max}) for each experiment.

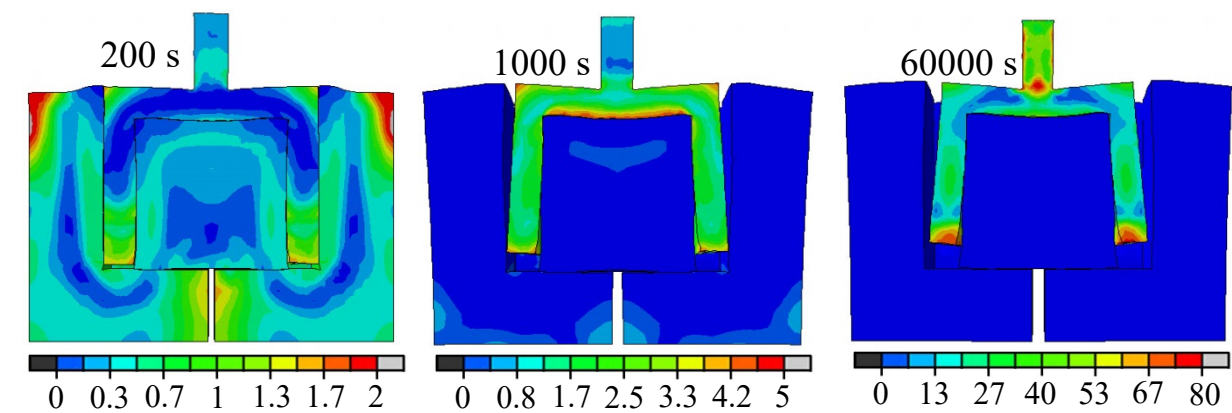


(a) Comparison between Measured and Predicted Pattern Allowances for Experiment 1

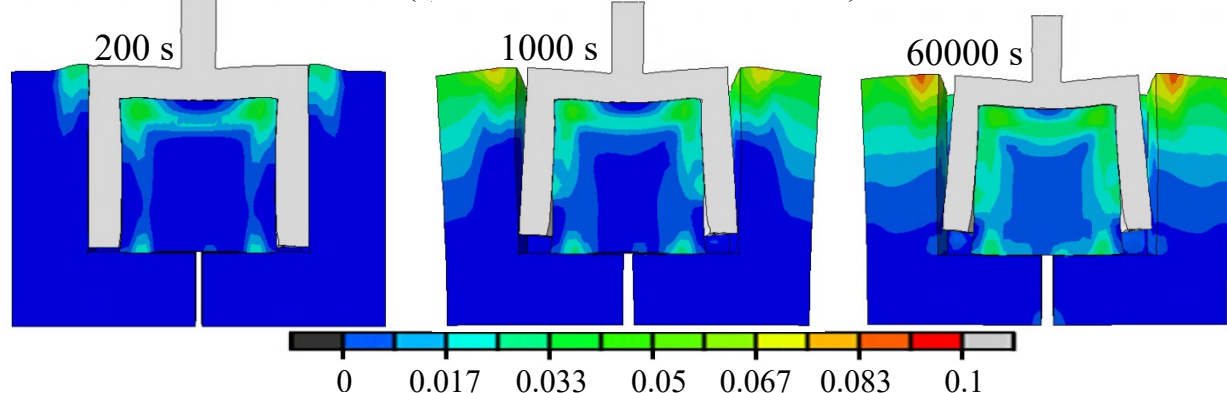


(b) Root Mean Square Error of Pattern Allowances for all Experiments

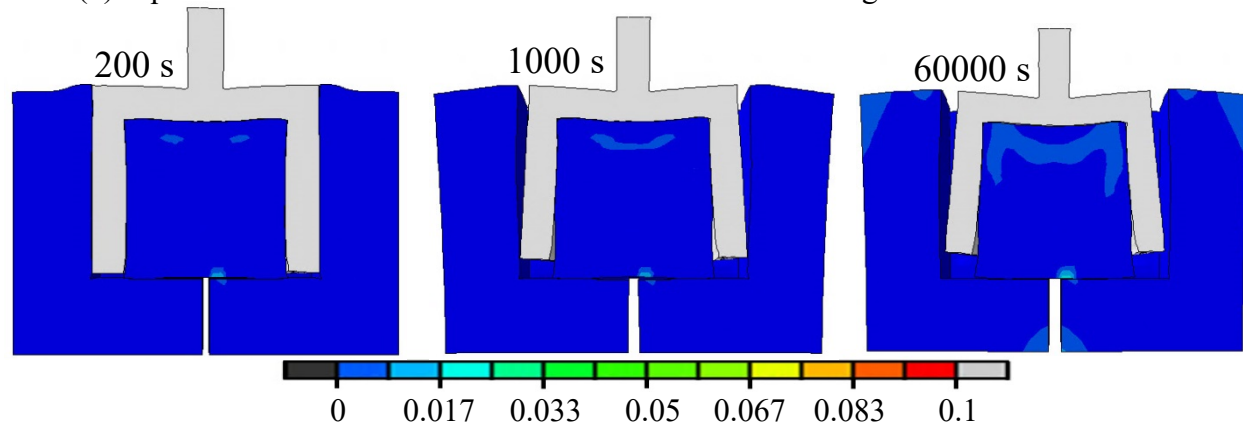
Figure 3.37 The predicted pattern allowances for bracket 1 are in good agreement with the measurements (a). The root mean square error ranges from 0.39% to 0.52% for all brackets (b).



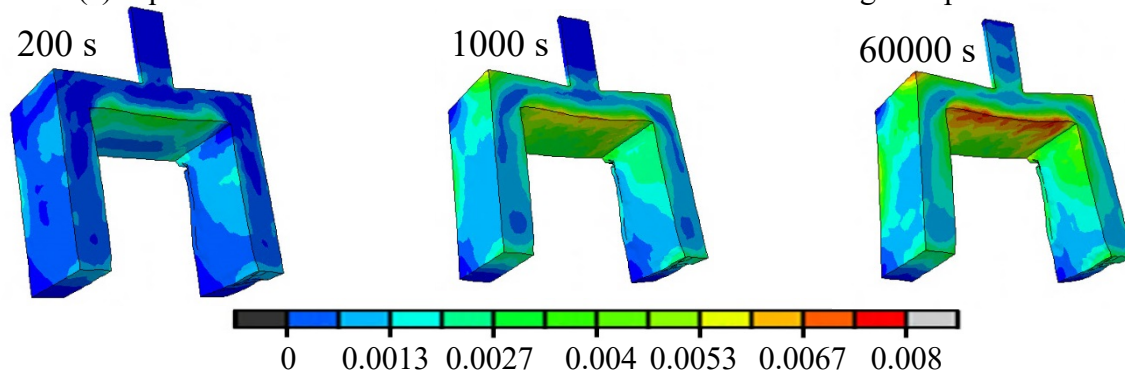
(a) von Mises Stress (units in MPa)



(b) Equivalent Plastic Strains in the Mold on the Drucker-Prager Shear Failure Surface



(c) Equivalent Plastic Strains in the Mold on the Drucker-Prager Cap Surface



(d) Equivalent Plastic Strains in the Bracket

Figure 3.38 Predicted von Mises stresses and equivalent plastic strains. Distortions are magnified by a factor of 5.

3.4 Predictions and Measurement Results for Case Study Casting

Predicted temperature contours from the thermal simulations are shown at 500 s and 5000 s in Figure 3.39. Large temperature gradients can be seen throughout the casting at both times. For example, the body of the casting (left side of Figure 3.39) cools much faster than the section near large hole on the right side. After 500 s, temperatures throughout the casting range from approximately 900°C to over 1400°C. Even after 5000 s (~1.5 hours), temperatures vary by over 400°C. As a result of these variations, distortions can be expected from this uneven cooling.

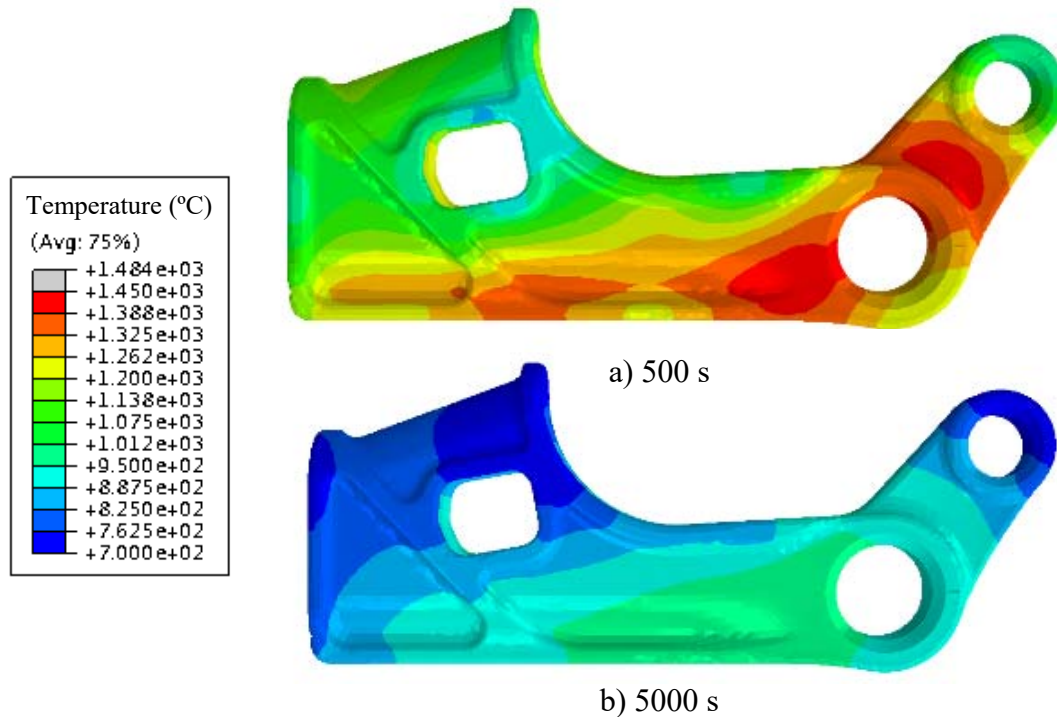


Figure 3.39 Predicted temperatures at 500 (a) and 5000 (b) s.

The deformed shape at room temperature predicted by the finite element stress simulation is shown in Figure 3.40. The deformations are magnified by a factor of 10. The distorted shape (green) is overlaid onto the undeformed shape to illustrate where distortions occur. For example, the arm on the right side is distorted outward. Most likely, the mold impedes the thermal contractions to generate this distortion. However, uneven cooling could also have an impact. The predicted pattern allowances (shown below) will give insight to which the responsible phenomenon. Also, the holes on the right side of the casting appear to be enlarged. This is expected, as mold expansion and core restraint both can be expected to contribute to distortions of these features.

The predicted temporal evolution of feature length 3 (location shown in Figure 2.11) is plotted on complete (400,000 s) and 5000 s time scales in Figure 3.41. The complete time scale represents the time needed to cool the casting to room temperature. For the

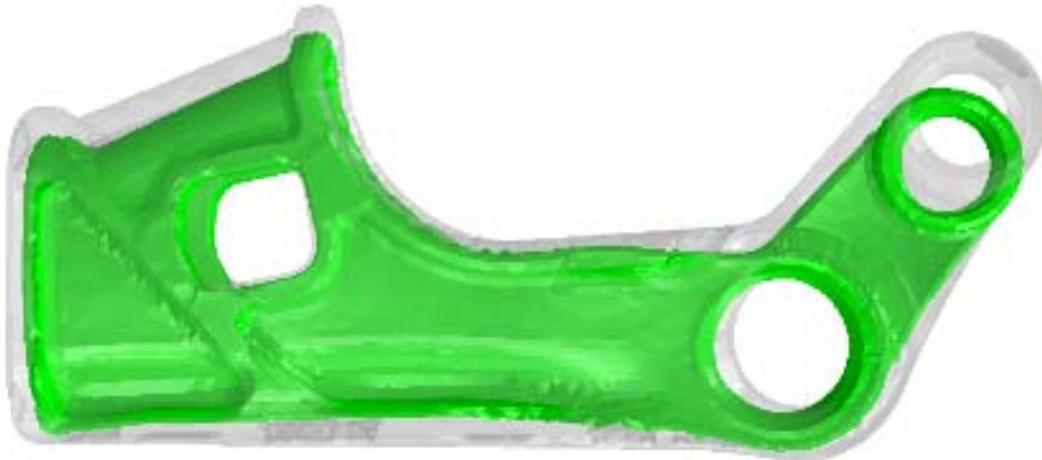
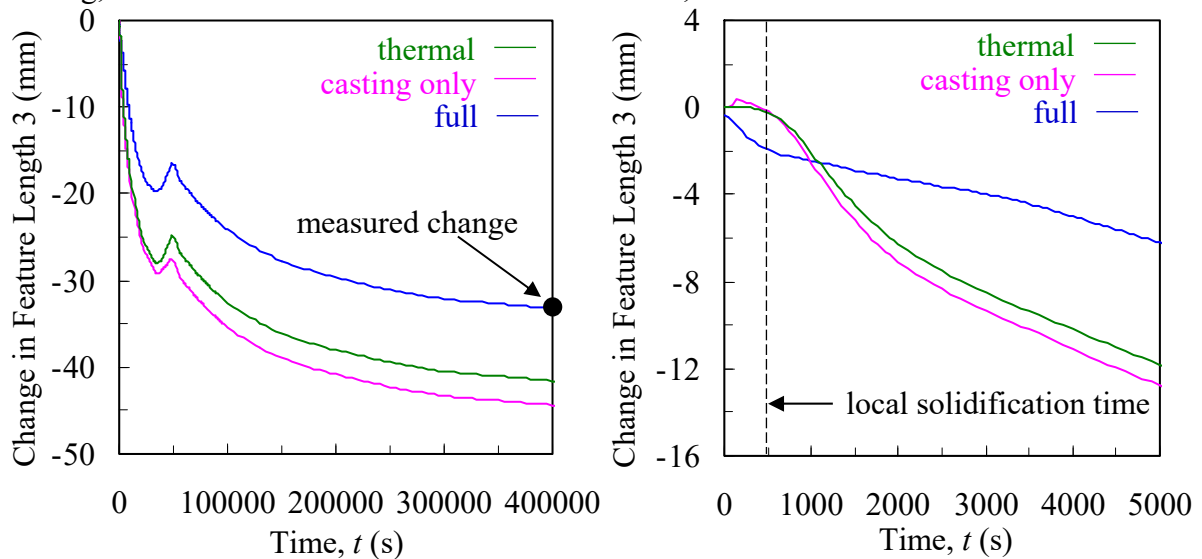


Figure 3.40 Deformed casting at room temperature.

thermal simulation (shown as the green curve), the feature length begins decreasing at approximately 500 s, which represents the approximate solidification time and is denoted by the vertical dashed line in Figure 3.41(b). Between 500 and 400,000 s, feature length 3 decreases approximately 41.5 mm, as seen on the complete time scale in Figure 3.41(a). This decrease occurs in the absence of distortions and represents the patternmaker's shrink. The increase in length change between 40,000 and 50,000 s is due to the solid state phase transformation from austenite to pearlite and ferrite. Differences between the casting only simulation (pink curve) and the thermal simulation can be seen beginning at 500 s. The curves gradually diverge until the end of the solid state phase transformation (at 50,000 s), after which the difference between the curves (approximately 4 mm) remains constant. Because the mold is not included in this simulation, this difference is due to uneven cooling, which distorts the arm inward. Therefore, the outward distortion observed in



a) Complete time scale

b) 5000 s time scale

Figure 3.41 The predicted length changes for feature length 3 shown on complete (a) and 5000 s (b) time scales. The complete time scale represents the time needed to cool the casting to room temperature.

Figure 3.40 must be caused by mold/core restraint. For the full simulation (blue curve), the length change during the initial 500 s (approximately -2 mm) is created by mold expansion. This expansion occurs during solidification. Once solidified, the casting has gained sufficient strength to resist any farther push-in from the mold. Beginning at 500 s, the full simulation feature length decreases at a slower rate than the thermal simulation feature length. This reduced contraction rate is due to core/mold restraint, which impedes thermal contractions and causes the feature to decrease at a slower rate than if it were unconstrained. As a result, the thermal and full simulation curves converge beginning at 500 s until they predict the same length change at 1000 s and then diverge until the beginning of the solid state transformation (~35,000 s). Throughout this time period, considerable distortions are generated by core/mold restraint. After the solid state transformation is complete (~50,000 s), the feature lengths in the full and thermal simulation contract at the same rate, signifying that no distortions are predicted after 50,000 s. When the casting has cooled to room temperature (after approximately 400,000 s), the full simulation has reduced in length by 34 mm (see Figure 3.41(a)). This value is very close to the measured reduction of feature length 3, which is denoted by the symbol in Figure 3.41(a) at 400,000 s.

Similar plots for feature 5 are shown in Figure 3.42. Very little difference can be seen between the thermal and casting only curves, which indicates that distortions created by uneven cooling are negligible for this feature. Also similar to feature 3, the solidification time occurs at approximately 500 s. Prior to 500 s, mold expansion increases feature length 5 by approximately 2.5 mm (see the full simulation curve in Figure 3.42(b)). This result is in contrast to mold expansion for feature 3, for which mold expansion causes a decrease in the length. Recall that this is because feature length 3 is measured on the outer casting surface, whereas feature length 5 is measured on an internal surface. After feature 3 expands to a maximum value at 2000 s, its length decreases at the same rate as the thermal simulations, indicating that no distortions are predicted after 2000 s.

Through the analysis performed on feature lengths 3 and 5, several conclusions can be drawn. First, mold expansion considerably impacts feature lengths at early times. The features may either increase or decrease in length depending where they are located on the casting surface. Core/mold restraint also has a significant impact on features and always leads to increased feature lengths (i.e., decrease in pattern allowances). Finally, no distortions were predicted after the solid state phase transformation. This is not unreasonable, as the solid state phase transformation is associated with a significant increase in the casting strength.

Comparisons between all predicted pattern allowances are compared to the measurements in Figure 3.43. In general, the pattern allowances were predicted with good accuracy. The free shrink line is denoted by a dashed horizontal line and represents the predicted pattern allowances using the patternmaker's shrink. All of the pattern allowances (measured and predicted) are different from the free shrink. In other words, every feature chosen for this study has some amount of distortion associated with it. These distortions increase the pattern allowances for some features and decrease them for others. Even for situations where the predicted pattern allowances don't agree with the measurements, they predict the correct trends.

The difference between the measured and predicted pattern allowances determines the accuracy of the model. Clearly, some features were predicted more accurately than

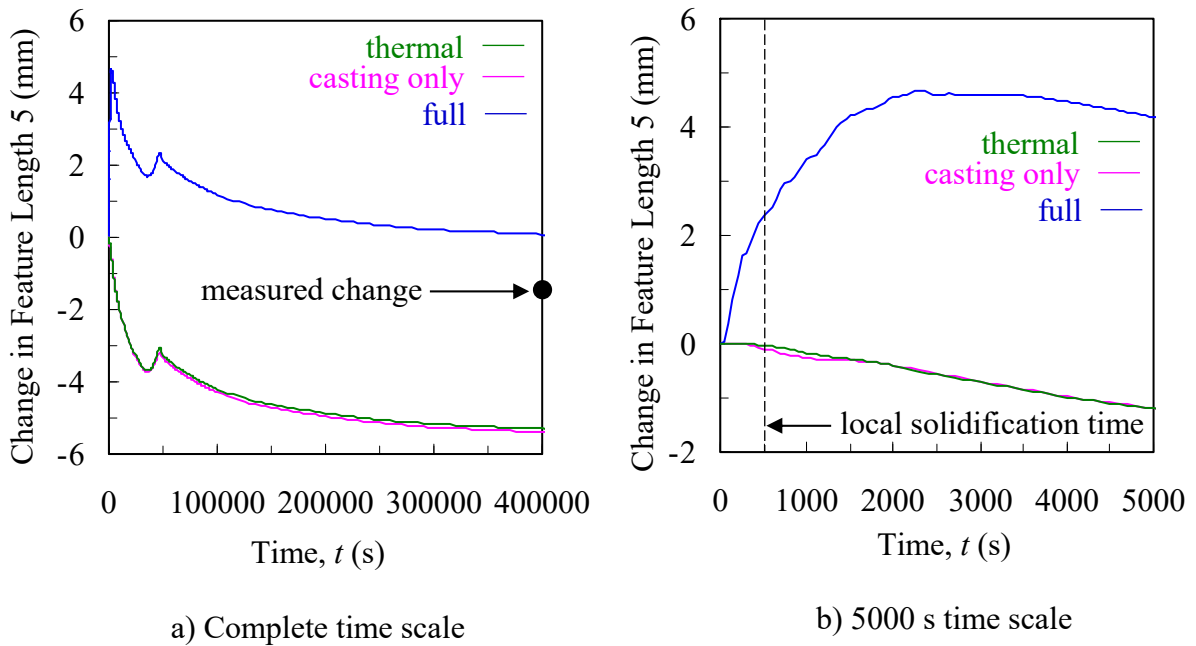


Figure 3.42 The predicted length changes for feature length 5 shown on complete (a) and 5000 s (b) time scales. The complete time scale represents the time needed to cool the others, which can make it difficult to evaluate the overall performance of the simulation. As a solution, a suitable figure of merit that combines the predicted pattern allowances of all features into a single value should be used. However, because pattern allowances can either be positive or negative, simply taking the average of all values is not appropriate. For such cases, the root mean square (RMS) can be used. The RMS is defined as

$$PA_{RMS} [\%] = \sqrt{\frac{1}{n} \sum_{i=1}^n (PA_{measured} - PA_{predicted})^2} \quad [3.1]$$

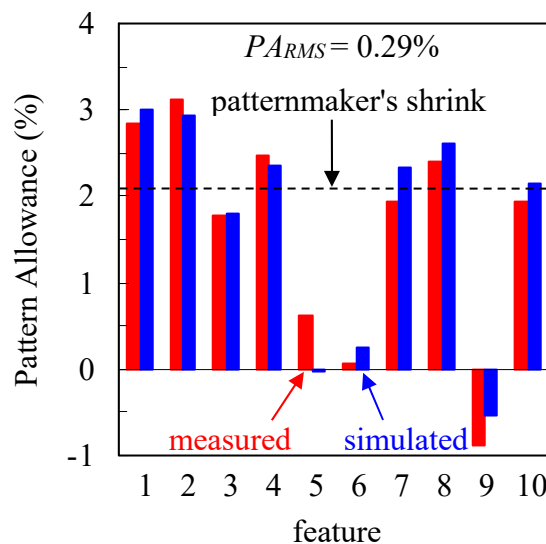


Figure 3.43 Comparison between measured and predicted pattern allowances. $PARMS$ is the root mean square of the difference between predicted and measured pattern allowances.

where n is the number of features, and $PA_{measured}$ and $PA_{predicted}$ are the measured and predicted pattern allowances, respectively. This number can be viewed as the average difference between measured and predicted pattern allowances. For the simulation, $PA_{RMS} = 0.29\%$. This small value demonstrates that the simulation predicts the pattern allowances with very good accuracy. Using the RMS value, the performance of different simulations can be compared.

Contours of equivalent plastic strain and von Mises residual stress (shown in MPa) are shown in Figure 3.44. Residual stresses are those that remain in the as cast part (i.e., before heat treatment) at room temperature. The largest residual von Mises stresses and strains occur in the body of the casting (on the left side in Figure 3.44). Considerable plastic strains are also predicted near the two holes in the casting arm (i.e., features 5 and 6). These areas of high residual von Mises stress and strain are near locations containing cores and thus, not unexpected.

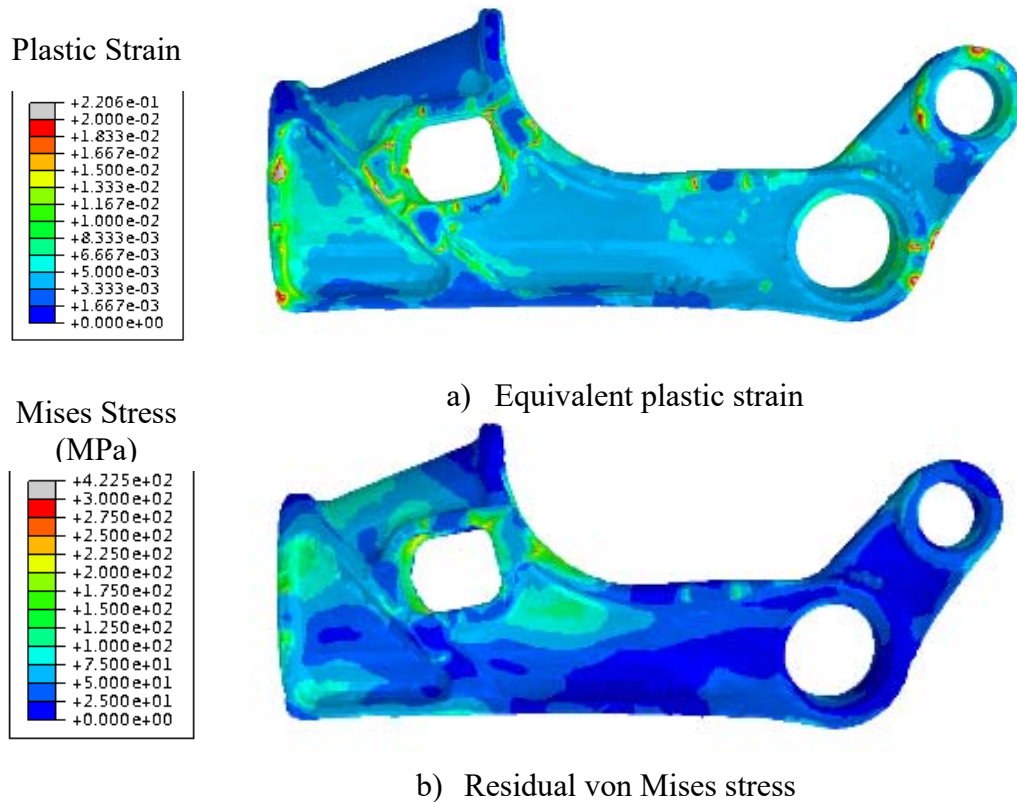


Figure 3.44 Predicted equivalent plastic strain and residual von Mises stress (units in MPa).

3.5 Implementation and Transitioning of the Research to Industry

In order for the investment in this research to make a positive and substantial impact to the steel foundry industry and manufacturing base of the United States it must be transitioned to industry. Throughout the project we have been partnering with MAGMA Foundry Technologies to facilitate one of our means to transition this research to industry. In this partnership we worked together to implement software modules and properties developed into *MAGMASOFT*® to advance our research efforts and to implement the

project developments into one of the most advanced software packages used throughout the foundry industry. Models and properties developed here for casting dimensional predictions have been implemented in *MAGMASoft* and *MAGMAstress* modules for cast steel. These modules include coupled stress-strain models developed during the course of this research for residual stresses, distortion and hot tearing prediction, among others illustrated in Figure 3.45. In addition, MAGMA has measured and shared high temperature mechanical properties of sand molds. They have been implementing the Drucker Prager constitutive material model as used in this project work in their software, as illustrated in Figure 3.45(b). MAGMA has supported the goals of this project, to provide casting designers and foundry engineers with engineering tools for predicting the final dimensions and service performance of steel castings. Developments arising from this project implemented through the MAGMA software will serve as a basis for collaboration between foundries and part designers to produce better castings for end users such as the

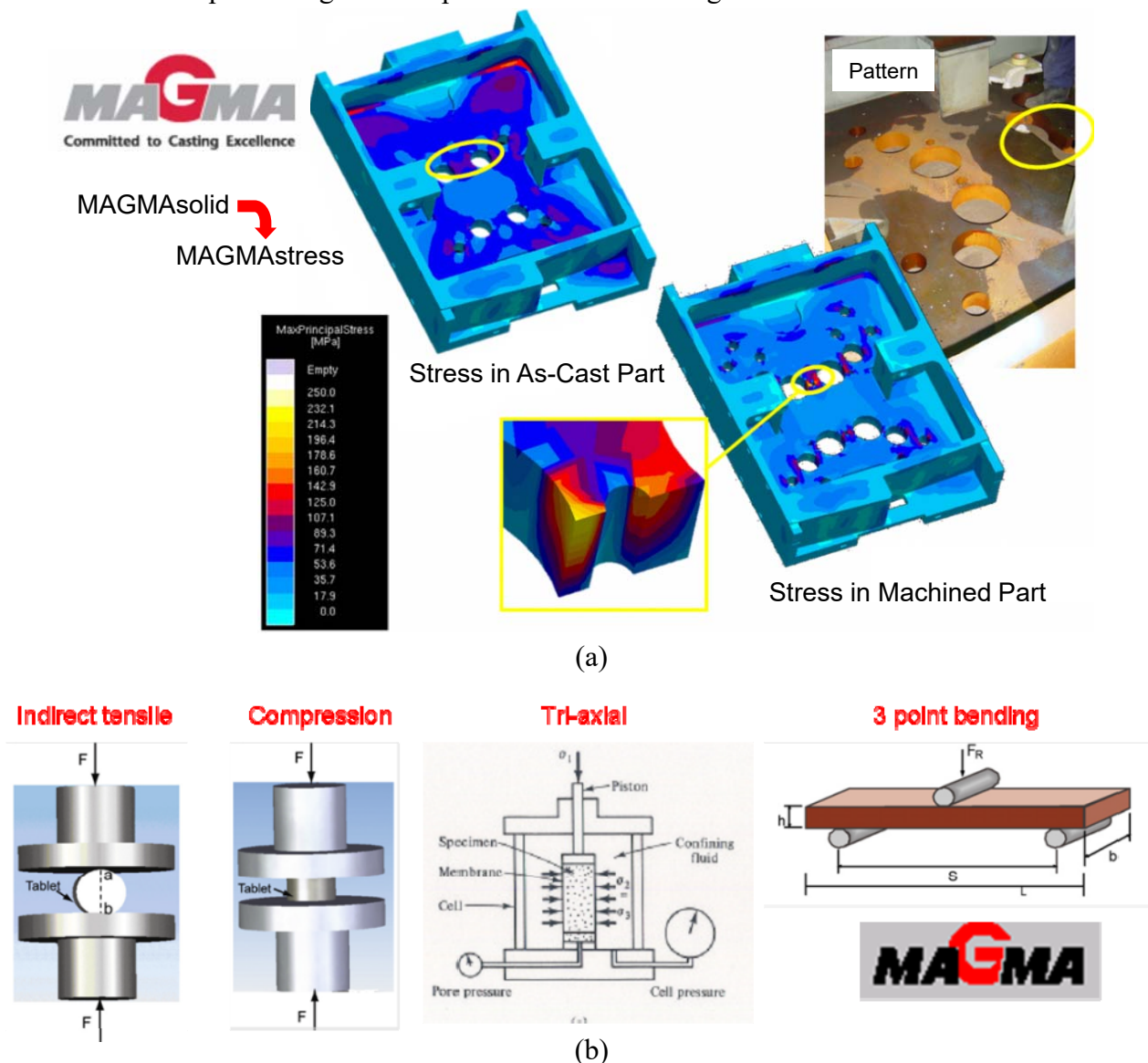


Figure 3.45 (a) Implementation of models developed into MAGMAstress for residual and resulting machined component stress predictions. (b) Bonded sand mechanical tests performed by MAGMA for use with Drucker-Prager material model within MAGMAstress.

Department of Defense.

Under the auspices of the Steel Founders' Society (SFSA) three case studies were completed and presented at SFSA research meetings and reviews: a lever arm casting produced at Sivyer Steel, a drag socket cast at Bradken-London (details in this report), and a trunnion link casting produced at Bradken-London, as shown in Figure 3.46. These case studies facilitate the transition of the technology developed during this project to industry by demonstrating its application with industry partners. These case studies have shown that the model gives accurate predictions of deformations due to mechanical interactions at mold-metal interface. They have demonstrated that the model shows areas of distortion and plastic strain causing quality variations or dimensional non-conformance. The case studies have shown that patterns designed with the model to address problem areas can be designed to get dimensions right for the initial pattern. In addition to the case studies, dozens of presentations were given throughout the duration of the project to the steel foundry industry through the SFSA to promote understanding of this research, which will lead to the foundry industry's use of the methodology described here and its advances in

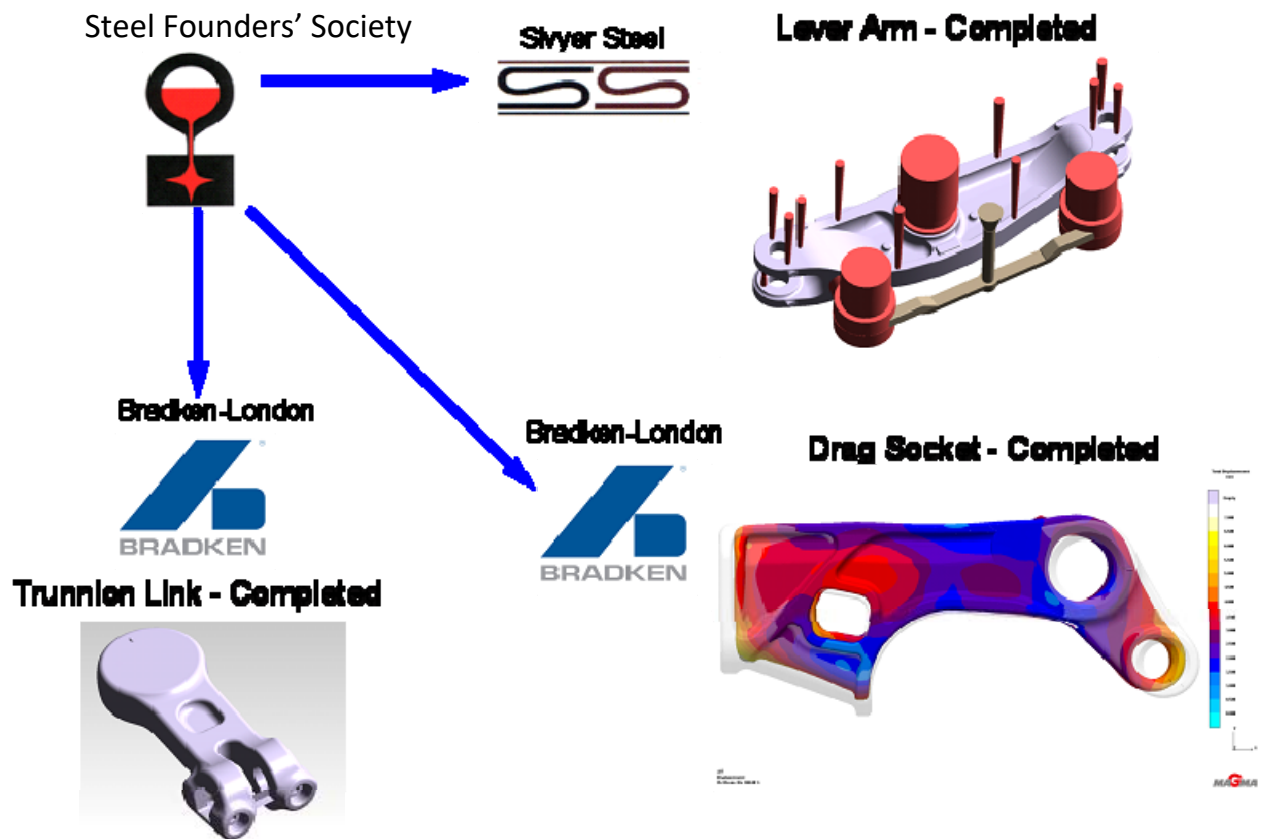


Figure 3.46 Under the auspices of the Steel Founders' Society (SFSA) three case studies were completed and presented at SFSA research meetings and reviews: a lever arm casting produced at Sivyer Steel, a drag socket cast at Bradken-London (details in this report), and a trunnion link casting produced at Bradken-London.

dimensional predictions in the years to come.

Another important means of implementing and transitioning this research to practical applications is by publishing it so it may be used and implemented through any casting simulation software, and many commercially available finite element stress analysis software packages. Though the stress model presented here uses ABAQUS or MAGMAstress, other stress analysis such as Ansys, LS-DYNA, Permas, Nastran, Adina and others can be used. The publications produced for this project under sponsorship of the Defense Logistics Agency are given in the References section of this report as references [19,22] and [41-50]. Also, the modeling approach presented here is not limited to steel sand castings, and in principle can be applied to non-ferrous alloys. However, the necessary measurements and property development work would be required.

Finally, this work has sparked ground breaking research using the inverse finite element method. The inverse finite element method can be used to determine an initial geometry based on a final geometry subject to plastic loads. This means that using the products of this research program pattern dimensions can be determined using the inverse finite element method based on desired final casting dimensions. This research continues through the use of its models, and leveraging this project's research results, in a forthcoming publication by Daniel Galles, Jia Lu, and Christoph Beckermann demonstrating the inverse analysis concept to determine pattern dimensions.

4. Summary of Work and Conclusions

4.1 Bar Casting Conclusions

Forces and displacements were measured in-situ during casting of a steel bar in a sand mold in this project task. The outcomes from this task fulfilled WBS task 2 "Development of computational algorithm and model to predict dimensional changes, distortions, residual stresses and cracks during casting of steel in a sand mold." Using embedded bolts at the two ends, the bar was strained during solidification and cooling to induce stresses and distortions. Multiple experiments with different straining periods were conducted. The experiments were simulated using a finite element stress analysis code employing an elasto-visco-plastic constitutive law that accounts for solidification. The thermal strain predictions were calibrated first using displacement measurements from the unrestrained bar experiments. The simulations for the strained bar experiments used the measured forces in the bolts as boundary conditions. It was shown that using constitutive model parameters determined from previous mechanical tests involving reheated steel specimens does not produce satisfactory agreement between the measured and predicted length changes for the strained bar experiments. This disagreement sheds considerable doubt on previous stress simulations of steel casting processes. Through a trial-and-error process involving repeated simulations of the experiments, the temperature dependence of the strain rate sensitivity exponent was adjusted until good agreement between the measured and predicted length changes was obtained. The adjustments were shown to be essentially the same for all experiments, even though the straining periods were different in each of the experiments. The significance of the adjustments in the viscoplastic parameter was demonstrated through a parametric study.

Validated mechanical property dataset for temperatures ranging from 1223 K (950 °C) to 1673 K (1400 °C) for the austenite phase of steel during casting were developed as part of completing this task. The data reveal a significantly different mechanical behavior

of steel during casting compared to what previous stress-strain data from reheated specimens show. This discrepancy may be attributed to differences in the microstructure. It is envisioned that the resulting products from this research will lead to more accurate stress simulations of steel casting processes. Additional work will be necessary to develop material datasets covering a wider range of steel compositions, other steel phases (e.g., ferrite), and temperatures below 1223 K (950 °C).

4.2 Cylinder Casting Conclusions

The effect of mold expansion on pattern allowances was investigated in this task. The outcomes from this task contribute to the completion of WBS tasks 1 “Experimental measurement of mechanical properties of bonded sand and steel at high temperatures” and WBS task 2 “Development of computational algorithm and model to predict dimensional changes, distortions, residual stresses and cracks during casting of steel in a sand mold”. In addition, the agreement between predictions and measurements completes WBS task 3 “Perform validation of the improved stress model from task 2”. Sand casting experiments were performed, in which the inner diameter of a hollow steel cylinder was distorted by core expansion. It was found from the finite element stress simulations that thermal expansion of the bonded sand only generated a small fraction of the observed inner diameter expansion. This demonstrated that sand dilation should be considered as the mechanism responsible for the remaining expansion. To predict dilative behavior, the bonded sand used to build the core and mold was modeled using the Drucker-Prager Cap constitutive law. Adjustments to model parameters were needed to predict the correct amount of dilation. By doing so, the barrel-shaped profile of the inner diameter was accurately predicted, as the simulated pattern allowances fell within the scatter of the measurements.

Parametric studies investigated uncertainties associated with the high temperature mechanical properties. The finite element predictions were found to be sensitive to changes in high temperature Young’s modulus ($E_{H.T.}$) values less than 60 MPa but relatively insensitive for $E_{H.T.}$ values > 100 MPa. Changes to the cap eccentricity and normal consolidation line also impacted the predictions significantly. A final parametric study demonstrated the importance of controlling the packing density when building the molds.

The research accomplished in this work provided invaluable insight to the physics associated with sand mold expansion during solidification. The findings have not only identified the importance of dilation but have also quantified it. By calibrating the Drucker-Prager Cap model parameters to account for dilation, this represents the first study geared towards predicting casting distortions that are created by sand dilation. Due to the apparent impact of sand dilation on pattern allowances, it is envisioned that the present stress model can have an immediate positive impact on process efficiency for the foundry industry. With the aid of simulation, it is anticipated that the high costs and long lead times associated with pattern design can be drastically reduced. Although the current results are highly encouraging, the parametric studies revealed that further work is needed to better characterize the high temperature properties and mitigate the uncertainties associated with them.

4.3 Bracket Casting Conclusions

Dimensional inaccuracies that arise from mechanical interactions during sand casting were studied in this task as part of the completion of WBS tasks 1 “Experimental measurement of mechanical properties of bonded sand and steel at high temperatures” and WBS task 2 “Development of computational algorithm and model to predict dimensional changes, distortions, residual stresses and cracks during casting of steel in a sand mold”. In addition, the agreement between predictions and measurements found in the final analysis of this work contributes to the completion of WBS task 3 “Perform validation of the improved stress model from task 2”. Casting experiments involving a U-shaped steel bracket were performed and then simulated in order to study the effect of such interactions on pattern allowances. The temporal evolution of the gap opening between the bracket legs was measured *in situ* and revealed that mold restraint generated considerable distortions after solidification. Distortions were also created by mold expansion during solidification. Mold fracture was observed during the experiments approximately 100 s after filling. It was later revealed during the stress simulations that unless this fracture behavior was considered, the tensile strength of the outer mold impeded the pushout of the bracket legs and distortions were under-predicted. To account for this effect, surface-based cohesive behavior was utilized to model mold fracture. Finally, it was found that the significant variations in the LVDT measurements could be predicted through modest changes to the packing density of the molds.

This work culminates and validates our technical advances in predicting pattern allowances for steel sand castings. It is envisioned that the current computational model will drastically reduce lead times as well as reduce dimensional variations in the as-cast part. Most importantly, because the simulations were performed using commercial software, the procedures outlined in this study can be easily duplicated and transferred to industry. This gives the foundry engineer the necessary tools to minimize distortions and predict pattern allowances efficiently and accurately.

4.4 Casting Case Study Conclusions

A finite element stress analysis was performed to predict distortions for a production steel casting using the accomplishments from this research project to complete WBS task “Demonstration of new simulation technology through a case study involving a steel casting produced in a foundry.” As reported here, significant variations from the patternmaker’s shrink (2.1%) were revealed in the measured pattern allowances, which ranged from -0.89% to 3.11%. The casting, mold, gating and risers were included in the finite element simulations and contact was used to model interactions between the mold and casting. Elasto-visco-plastic and Drucker Prager Cap constitutive laws developed during this project were employed for the steel and bonded sand, respectively, and model parameters were calibrated in previous experimental studies. The computational model featured the ability to predict distortions caused by mold expansion (due to both thermal expansion and dilation), mold restraint, and uneven cooling. The simulations predicted the measured pattern allowances with good accuracy, as the root mean square (RMS) value between measured and predicted pattern allowances was calculated as 0.29%. While pattern allowances based on current production practices, the pattern maker’s shrink rule, had a much larger RMS error of 1.31%.

In addition to the distortions, significant residual stresses were also predicted in the highly distorted regions of the casting. By accounting for the relevant physical phenomena that lead to distortions, the present simulations have demonstrated the ability to predict pattern allowances for a production casting. It is envisioned that such predictive capability will lead to efficient pattern design requiring fewer iterations and also minimize dimensional inaccuracies.

Additional case studies have been performed as part of this project, and these have been presented to the SFSA at various meetings and research reviews. At the time of writing this report, the project team is continuing to work on case studies to be presented to the SFSA at a later date. In addition, a military casting, muzzle brake component, has been analyzed using the technology resulting from this research project in production and best practices development work with the SFSA and the Rock Island Arsenal.

4.5 Concluding Remarks on Project Metrics

During the course of the project, three key metrics were determined to reflect project goals as given in Table 4.1. These metrics could be readily evaluated to demonstrate progress during the course of the project. The progress and status of these metrics were reported on at yearly AMC Technical Reviews. Baseline or starting points for the metrics and final states of the metrics are given in the table, along with the methods of measurement and demonstration. Additional research and development milestones reported at the yearly review meetings were: development of mechanical properties of bonded sand and steel as a function of temperature, development of model to predict dimensional

Table 4.1 Three metrics addressed and successfully demonstrated during the project

Project Metric Addressed	Baseline of Metric at Start of Project	Metric at End of Project	How Measured	How Demonstrated
Mechanical Property Data for Steel and Sand	Mechanical properties are independent of temperature or inaccurate	100% of steel and mold mechanical properties are temperature dependent	In-situ and laboratory measurement at controlled temperatures & strain rates	Excellent agreement for bar castings unrestrained and restrained, and for brackets and cylinders
Pattern Allowances	56% of features conform to shrink rule of $2.1\% \pm 1\%$ [1], in drag socket case study use of pattern maker's shrink rule has RMS error of 1.31%.	90% within $\pm 1\%$ of desired dimension, from drag socket case study RMS error is 0.3% using technology developed here	From pattern allowances of castings with core & mold interaction, measurements from foundry	Results for bar pattern allowance accuracy, bracket and cylinder geometries and drag socket case study
Stress Simulation for Volumetric Deformation and Distortion Prediction	Dimensional accuracy is $\pm 6.2\%$ (2σ) of feature length [1]	Simulation results validated to within $\pm 1\%$ of feature length, from drag socket case study RMS error is 0.3%	Validate stress simulation of steel casting with core, comparison of measured and predicted distortions	Dimensional accuracy for model with bar castings, and cylinders and brackets with sand cores, drag socket case study demonstrates this

changes, distortions, stresses and cracks, and validation of improved stress model through controlled testing.

Key benefits arising from the project are:

- reduced costs and lead times resulting from first pour parts produced correctly
- higher quality parts from reduced variability
- lighter weight parts from thinner-walled castings
- improved service reliability

Prior to this work, even by following the most cost-effective approaches to metal casting processes and their design, “the unpredictable nature of patternmaker’s contraction [made] tooling adjustments inevitable.”[51] Following this work, using the technology developed through this project, accurate prediction of final as-cast dimensions will reduce scrap rates, will reduce and guide use of appropriate machining, shrinkage and distortion allowances, and will substantially decrease lead times required to deliver acceptable first article castings. According to a study by Creese et al. [52] the average lead time for a “new order” steel sand casting is 9 weeks with a standard deviation of 5 weeks, and a maximum lead time of 21 weeks. Considering that 60% of this time is “consumed by dimensional issues” [53], applying the technology developed during this project will directly and substantially reduce lead times by getting dimensions right on the first pattern, or if needed at all, first iteration on pattern making trial-and-error development. In particular, for the 2000 pound drag socket casting case study presented here, dimensions of features such as feature IDs 5, 6 and 9 shown in Figure 2.11 require numerous iterations to get right and meet specifications. Yet the modeling developed here does an excellent job of predicting them correctly (see Figure 3.43) and no iteration is required. Therefore, 60% of the lead time and the associated costs and scrapped castings could be virtually eliminated. By eliminating scrapped castings, either in the pattern development stage, or in the production stage by predicting and controlling process variability, casting yield will be greatly improved and costs decreased. A previous study found that 7% of the reduction in casting yield is due to scrapped castings [54]. Furthermore, when dimensional issues arise, foundries have been addressing them by increasing machining allowances and increase padding of the casting geometry which both decreases casting yield and increases machining cost.

Considering the above discussion, it is anticipated that the impact on the steel foundry industry from this project will be a 2% reduction in costs and 2% improvement in yield to meet the key metrics given in our statement of work. These appear to be conservative estimates comparing them to similar metrics from a previous study in prediction of dimensions in investment castings [55]. In that report, Cannell and Sabau wrote that improving dimensional predictions would increase casting yield from 55% to 65% and reduce scrap from 4% to 3%.

Acknowledgements

This research is sponsored by the Defense Logistics Agency (DLA) – Troop Support, Philadelphia, PA and the Defense Logistics Agency Logistics Operations, J335, Research & Development, Ft. Belvoir, VA, under subcontract number 2012-525 from the Advanced Technology Institute, Summerville, South Carolina. This work was conducted under the auspices of the Steel Founders' Society of America (SFSA) through substantial in-kind support and guidance from SFSA member foundries. In particular, the authors gratefully appreciate the participation of Sivyer Steel Casting, Bradken-Atlas and Bradken-London in case studies and providing CAD models and measurements data for the case studies. Last not least, substantial in-kind support was provided by our project partners at MAGMA Gießereitechnologie GmbH and MAGMA Foundry Technologies Inc. whose software we relied upon for casting simulation results, and additional support in stress analysis modeling and properties.

References (publications in blue were produced under sponsorship of this program)

1. R. Voigt, Pennsylvania State University, personal communication, 2012.
2. P. Feltham, The plastic flow of irons and plain steel above the a-3 point, *Physical Society – Proceedings*, vol. 66, no. 406B, pp 865-83, 1953.
3. P.J. Wray and M.F. Holmes, Plastic deformation of austenitic iron at intermediate strain rates, *Metallurgical Transactions A*, vol. 6A, no. 6, pp 1189-96, 1975.
4. P.J. Wray, Effect of carbon content on the plastic flow of plain carbon steels at elevated temperatures, *Metallurgical Transactions A*, vol. 13A, no. 1, pp 125-34, 1982.
5. T. Suzuki, K.H. Tacke, K. Wunnenberg, and K. Schwerdtfeger, Creep properties of steel at continuous casting temperatures, *Ironmaking and Steelmaking*, vol. 15, no. 2, pp 90-100, 1988.
6. C. Zhang, M. Bellet, M. Bobadilla, H. Shen, and B. Liu, Inverse finite element modelling and identification of constitutive parameters of uhs steel based on gleeble tensile tests at high temperature, *Inverse Problems in Science and Engineering*, vol. 19, no. 4, pp 485-508, 2011.
7. R.N. Parkins and A. Cowan, Effects of mould resistance on internal stresses in sand castings, *Proceedings of the Institute of British Foundation*, paper no. 1062, pp A101-9, 1953.
8. C.S.E. Mkumbo, B.B. Nyichomba, J. Campbell, and M. Tiryakioglu, Linear contraction of grey iron sand castings, *International Journal of Cast Metals Research*, vol. 14, no. 4, pp 225-34, 2002.
9. B.B. Nyichomba and J. Campbell, J., M., Linear contraction and residual stresses of aluminum alloy sand castings, *International Journal of Cast Metals Research*, vol. 11, pp 163-7, 1998.

10. B.B. Nyichomba, I.M. Cheya, and J. Campbell, Linear contraction of ductile iron castings, *International Journal of Cast Metals Research*, vol. 11, pp 179-86, 1998.
11. C. Monroe, and C. Beckermann: *61st Steel Founders Society of America Technical and Operating Conference*, paper no. 5.7, Steel Founders' Society of America, Chicago, IL, 2006.
12. C. Monroe, and C. Beckermann, Deformation during casting of steel: mold and material properties, *Proceedings of the 61st SFSA Technical and Operating Conference*, paper no. 5.6, Steel Founders' Society of America, Chicago, IL, 2007.
13. Y. Inoue, Y. Motoyama, H. Takahashi, K. Shinji, and M. Yoshida: *J. Materials Processing Technology*, 2013, vol. 213, pp. 1157-65.
14. F. Peters, R. Voight, S.Z. Ou, and C. Beckermann: *Int. J. Cast Metals Res.*, 2007, vol. 20, no. 5, pp. 275-87.
15. O. Yamamoto, H. Yamada, and M. Saito: *Japanese Foundry*, 1978, vol. 50, pp. 14-18.
16. I. Caylek and R. Mahnken: *Int. J. Cast Metals Res.*, 2010, vol. 23, no. 3, pp. 176-84.
17. J. Thole and C. Beckermann: *Int. J. Metalcasting*, 2010, vol. 4, no. 4, pp. 7-18.
18. R. Ami Saada, G. Bonnet, and D. Bouvard: *Int. J. Plasticity*, 1996, vol. 12, no. 3, pp. 273-94.
19. Galles, D., and Beckermann, C., "In-Situ Measurement and Prediction of Stresses and Strains during Casting of Steel," *Metall. Mater. Trans. A*, Vol. 47A, 2016, pp. 811-829.
20. MAGMASOFT® v4.6, Magma GmbH, Aachen, Germany.
21. J. Miettinen: *Metall. Mater. Trans. B*, 1997, vol. 28, no. 2, pp. 281-97.
22. Galles, D., and Beckermann, C., "Measurement and Simulation of Distortion of a Steel Bracket Casting," in *Proceedings of the 66th SFSA Technical and Operating Conference*, Paper No. 5.2, Steel Founders' Society of America, Chicago, IL, 2012.
23. K.D. Carlson and C. Beckermann: *Int. J. Cast Metals Res.*, vol. 25, 2012, pp. 75-92.
24. C.A. Monroe, C. Beckermann, J. Klinkhammer: *Modelling of Casting, Welding, and Advanced Solidification Processes – XII*, S.L. Cockcroft and D.M. Maijer, Warrendale, PA, 2009, pp. 643-49.
25. C. Monroe: Ph.D. Thesis, University of Iowa, Iowa City, Iowa, 2009.
26. M. Pokorny, C. Monroe, and C. Beckermann: *Int. J. Metalcast.*, 2008, vol. 2, no. 4, pp. 41-53.
27. J. Bluhm and R. DeBoer: *ZAMM – J. Appl. Math. Mech.*, 1997, vol. 77, no. 8, pp. 563-77.
28. A.P. Roberts and E.J. Garboczi: *J. American Ceramic Soc.*, vol. 83, no. 12, 2000, pp. 3041-48.

29. R.A. Hardin and C. Beckermann: *Metall. Mater. Trans. A*, 2007, vol. 38A, pp. 2992-3006.
30. ABAQUS[®], Abaqus, Inc., Providence, RI.
31. J.C. Simo and T.J.R. Hughes: *Computational Inelasticity*, Springer-Verlag New York Inc., New York, NY, 1998.
32. C. Martin, M. Braccini, and M. Suery: *Int. J. Plast.*, 2002, vol. 15, pp. 981-1008.
33. A.C.F. Cocks: *J. Mech. Phys. Solids*, 1989, vol. 37, no. 6, pp. 693-715.
34. V. Tvergaard and A. Needleman: *Acta Metall.*, 1984, vol. 23, no. 1, pp. 157-69.
35. E.B. Marin and D.L. McDowell: *Comput. Struct.*, 1997, vol. 63, no. 3, pp. 579-600.
36. S. Koric and B.G. Thomas: *Int. J. Num. Met. Eng.*, 2006, vol. 66, pp. 1955-89.
37. B.G. Thomas: *ISIJ Int.*, 1995, vol. 35, no. 6, pp. 737-743.
38. P.F. Kozlowski, B.G. Thomas, J.A. Azzi, and H. Wang: *Metall. Mater. Trans. A*, 1992, vol. 23A, pp. 903-18.
39. S. K. Saxena, R. K. Reddy and A. Sengupta: *Proceedings of the International Workshop on Constitutive Equations for Granular Non-Cohesive Soils*, pp. 629-45, 1989.
40. A. Hettler and I. Vardoulakis: *Geotechnique*, 1984, vol. 2, pp. 183-98.
41. Galles, D. and Beckermann, C., "Effect of Sand Dilation on Distortions and Pattern Allowances during Steel Sand Casting", *Int. J. Cast Metals Research*, published online February 2017, Crossref DOI link: <https://doi.org/10.1080/13640461.2017.1290909>.
42. Galles, D., Monroe, C., and Beckermann, C., "Measurement and Prediction of Stresses during Casting of a Steel Bar," in Proceedings of the 65th SFSA Technical and Operating Conference, Paper No. 5.5, Steel Founders' Society of America, Chicago, IL, 2011.
43. Galles, D., Monroe, C.A., and Beckermann, C., "Measurement and Simulation of Deformation and Stresses in Steel Casting," IOP Conf. Series: *Materials Science and Engineering*, Vol. 33, 2012, 012049 (8 pages).
44. Galles, D., and Beckermann, C., "Distortion of a Steel Cylinder Casting with a Core," in Proceedings of the 67th SFSA Technical and Operating Conference, Paper No. 5.8, Steel Founders' Society of America, Chicago, IL, 2013.
45. Galles, D., "Measurement and Prediction of Distortions During Casting of a Steel Bar," Master of Science Thesis, The University of Iowa, December, 2013.
46. Galles, D., and Beckermann, C., "Effect of Sand Dilation on Core Expansion during Steel Casting," IOP Conf. Series: *Materials Science and Engineering*, Vol. 84, 2015, 012022 (8 pages).

47. Galles, D., and Beckermann, C., "Simulation of Distortions and Pattern Allowances for a Production Steel Casting," in Proceedings of the 69th SFSA Technical and Operating Conference, Paper No. 3.7, Steel Founders' Society of America, Chicago, IL, 2015.
48. Galles, D., and Beckermann, C., "Modeling of Distortion of a Steel Bracket Sand Casting," in *Shape Casting: 6th International Symposium*, eds. M. Tiryakioglu, M. Jolly, and G. Byczynski, TMS, John Wiley & Sons Inc., Hoboken, NJ, 2016, pp. 35-42.
49. Galles, D., "Prediction of Distortions and Pattern Allowances in Steel Sand Castings," Doctor of Philosophy Thesis, The University of Iowa, August, 2016.
50. Galles, D., and Beckermann, C., "Prediction of Distortions and Pattern Allowances during Sand Casting of a Steel Bracket," *Int. J. Cast Metals Research*, Vol. 30, 2017, pp. 133-147.
51. Creese, R.C., Atluri R. and Rammohan N., "Sandcasting Lead-Time Prediction Model," AACE International Transactions, Morgantown, 1997, pp. 1-6.
52. Karve, A., Chandra, M.J. and Voigt, R.C., "Determining Dimensional Capabilities from Short Run Sample Casting Inspection," AFS Transactions, Vol. 106, pp. 699-703, 1998.
53. Gwyn, M.A., "Cost-Effective Casting Design," *Modern Casting*, Vol.88, No.5, 1998, pp.32-36.
54. Hardin, R.A., and Beckermann, C., "Current State of Casting Yield: Results of 1997 SFSA Survey," AFS Transactions, Vol. 106, 1998, pp. 633-642.
55. Cannel, N. and Sabau, A., "Predicting Pattern Tooling and Casting Dimensions for Investment Casting, Phase II," Final Technical Report for the U.S. Department of Energy, Energy Efficiency and Renewable Energy, Industrial Technologies Program, 2005.

Appendix A: Student Involvement in Research and Modeling Development

A large and important part of the research investment made in this project has gone towards the support of a graduate research assistant, who worked throughout most of duration of the project. This student was Dr. Daniel J. Galles. Supported by the project, he was able to complete his academic and professional training with a high level of success evidenced by the publications he and Professor Beckermann produced over the course of this project (see references 19, 22, and 41 through 50). He completed his Master of Science degree in December 2013 with the thesis titled "Measurement and Prediction of Distortions During Casting of a Steel Bar", and his Doctor of Philosophy degree in August 2016 with the thesis titled "Prediction of Distortions and Pattern Allowances in Steel Sand Castings." He is currently a postdoctoral researcher in the Materials Manufacturing Technology Branch for the United States Army Research Laboratory.